LBL-26805

Center for Advanced Materials

CAM

Surface Structural Analysis of Small Molecules on Transition Metal Single Crystal Surfaces with Low Energy Electron Diffraction

G.S. Blackman
(Ph.D. Thesis)

Received by OSTI

September 1988

MAY 01 1989

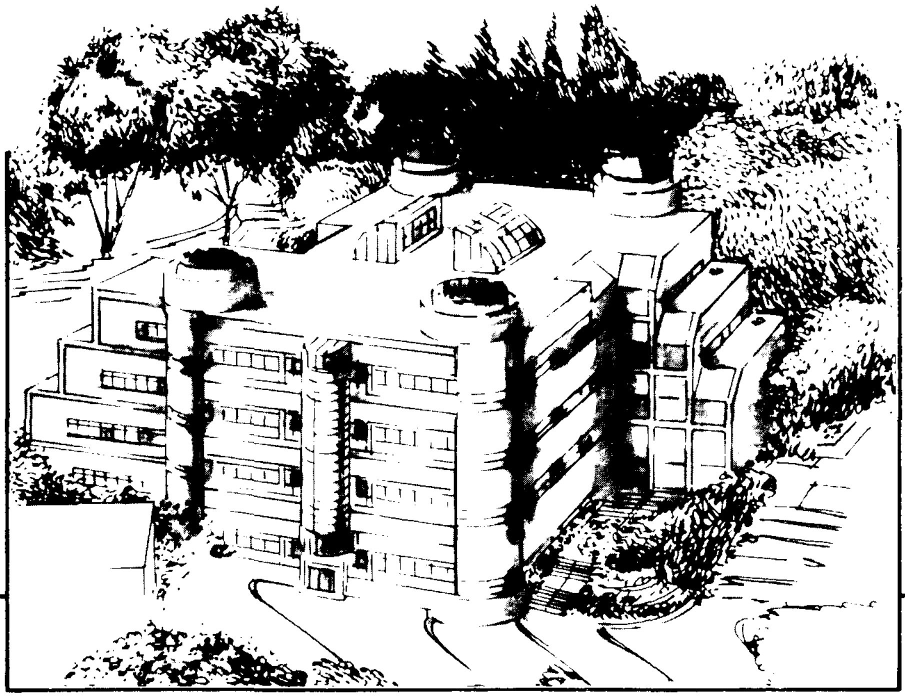

Materials and Chemical Sciences Division

MASTER

Lawrence Berkeley Laboratory • University of California
ONE CYCLOTRON ROAD, BERKELEY, CA 94720 • (415) 486-4755

Prepared for the U.S. Department of Energy under Contract DE-AC03-76SF00098

DISTRIBUTION OF THIS DOCUMENT IS UNLIMITED

LBL--26805

DE89 010681

SURFACE STRUCTURAL ANALYSIS OF SMALL MOLECULES ON TRANSITION METAL SINGLE CRYSTAL SURFACES WITH LOW ENERGY ELECTRON DIFFRACTION

Gregory Scott Blackman
Ph.D. Thesis

Department of Chemistry
University of California at Berkeley
and
Center for Advanced Materials
Materials and Chemical Sciences Division
Lawrence Berkeley Laboratory
1 Cyclotron Road
Berkeley, California 94720

September 1988

This work was supported by the Director, Office of Energy Research, Office of Basic Energy Sciences, Chemical Sciences Division, of the U.S. Department of Energy under Contract No. DE-AC03-76SF00098.

ps

Surface Structural Analysis of Small Molecules on Transition Metal Single Crystal Surfaces with Low Energy Electron Diffraction

Gregory Scott Blackman
Materials and Chemical Sciences Division
Lawrence Berkeley Labs
and Department of Chemistry
University of California
Berkeley CA 94720

Abstract

An attempt was made to go beyond the normal restrictions of surface crystallography. Low–temperature adsorption and coadsorbate induced ordering can be used to stabilize high coverage structures which would otherwise not form. Conventional LEED requires long–range order, digital LEED is sensitive enough to detect weak scattering from disordered adsorbates with no long–range order. Complete surface structures are presented for the first surface structure of NO, CO + benzene, NO + ethylidyne, and CO + ethylidyne all on the Rh(111) surface, and the first disordered molecular adsorbate: CO on Pt(111).

At low temperatures or higher applied pressures high coverage structures can be stabilized and unique bonding geometries occur. In UHV at room temperature both NO and CO occupy single adsorption sites, bridge- and top–sites, respectively. When NO is adsorbed at 40K or CO is adsorbed in an ambient pressure of 1x10^{-5} torr the structures change. Top and bridge sites are both occupied.

Coadsorbate–induced ordering occurs when two adsorbates form a different ordered structure than either would form by itself. The lateral interactions between adsorbates force the molecules to populate new sites. Pure CO or NO overlayers have only top and bridge sites occupied, but if either molecule is paired with a

coadsorbate (*e.g.* CO/benzene, CO/ethylidyne, or NO/ethylidyne) they move to hollow sites.

Until recently only ordered surface structures could be analyzed by LEED. Recent theoretical developments by Pendry *et al.* and new experimental techniques (digital LEED, this work) have made it possible to study disordered overlayers. The new digital LEED apparatus is sensitive enough to measure the weak diffuse scattering from disordered CO on Pt(111) to determine its structure. The first surface structure of a disordered molecular adsorbate is presented in this work.

Dedication:

To my parents, for teaching me that a Blackman never gives up, and to Leslie for being there when I needed her.

Acknowledgments

No PhD. thesis exists in a vacuum, not even one in surface science. It is the culmination of one person's work, but that person was guided, protected, and supported throughout the project. The most prominent figure in a thesis project is the advisor. It has been a great pleasure for me to have Professor Gabor Somorjai as my thesis advisor. Gabor takes an almost childish delight in all of science and in surface science in particular. His enthusiasm is infectious, and I always went away from a meeting with him ready to conquer all. One should always be prepared for the torrent of ideas from Gabor. If each idea were pursued to its conclusion there would be enough for several more PhD. theses. He is always effective at providing motivation, but he also knows when to sit back and let nature take its course.

Surface structural analysis is a unique blend of theory and experiment. None of the surface structures presented in this thesis could have been done without the active collaboration of our resident theoretician Michel Van Hove. His quiet competence and deep understanding of LEED has made it possible for our group to stay at the forefront of surface crystallography. Many thanks also to Mu–Liang Xu for his theoretical work on the diffuse LEED studies.

A surface science lab can be intimidating to the first–year graduate student, with its shiny steel vacuum chamber, multiple pumps, and seemingly endless array of complex electronics. There have been many people who guided my steps through

the maze. My first teacher, Rong–Fu Lin, introduced me to the wonders of surface science. Mathew Mate and Brian Bent were patient tutors who always had time for one more question. Frank Ogletree was an incredible source of knowledge and expertise in all the lore of LEED. He taught me the video LEED technique and suffered through most of the initial digital LEED problems.

One of the most important contributions to our scientific efforts comes from the support staff at LBL. Mechanical support from Dan Coulomb and electronics support from Joe Katz and Jim Severns are often all that stands in the way of our chambers reverting back to their original state: scrap metal and bits of wire. Brigid Tung and Ann Kahn had to deal with the day–to–day bureaucracy as well as the constant pressure from Gabor and the ever–changing stream of graduate students, post–docs, and visitors. Sandy Stewart in whose hands the knots of the money matters on The Hill magically untangle. And to all the others who make it possible for the scientist to concentrate on science.

There is life outside of the lab and there are people who make it worthwhile: Brian Naasz for his *pahwrful* thirst and love of good Cajun cooking; Mike Hilton and the other Horsemen for those many pleasant Sundays at the Pelican Inn; Andy Ninham who proved that not all Englishmen are bad cooks; Ken Lewis who shared the trials and tribulations of graduate life; and Karen Krushwitz who taught me that being a good chemist and being a good scholar are not mutually exclusive.

Finally I'd like to acknowledge The Group. past, present, and future. No other group does things quite the way we do, but you can't argue with success. The flavor of the group changes from year–to–year as people come and go, but it has always been a supportive, nurturing environment from which we can push off and excel in the world.

This work was supported by the Director, Office of Energy Research, Office of Basic Energy Sciences, Materials Science Division, of the US Department of Energy under Contract No. DE-AC03-76SF00098.

Contents

1 **Introduction** 1

2 **Experimental** 4
- 2.1 Introduction 4
- 2.2 Ultra-High Vacuum (UHV) 4
  - 2.2.1 Pumps 6
  - 2.2.2 Bakeout 11
- 2.3 Cleaning procedures 12
- 2.4 Electron Guns 16
- 2.5 Techniques 20
  - 2.5.1 Auger Electron Spectroscopy (AES) 20
  - 2.5.2 Low-Energy Electron Diffraction (LEED) 27
- 2.6 Digital LEED 36

3 **Low Temperature LEED: NO on Rh(111)** 46
- 3.1 Introduction 46
- 3.2 Background 47
- 3.3 Experimental 52
- 3.4 HREELS 53
- 3.5 Structural Search 58
- 3.6 Discussion 65
- 3.7 Conclusions 67

4 **Coadsorbate Induced Ordering** 70
- 4.1 Introduction 70
- 4.2 Background 73
- 4.3 LEED theory 77
- 4.4 Carbon Monoxide plus Benzene on Rh(111) 78
  - 4.4.1 LEED patterns 78
  - 4.4.2 HREELS of CO plus Benzene on Rh(111) 82

4.4.3 Structural Search and Results for the Rh(111) + (3 × 3) 2CO + Benzene Structure 85
4.4.4 Discussion of the Benzene Coadsorption Structures 88
4.5 Nitric Oxide and Carbon Monoxide plus Ethylidyne 91
4.5.1 LEED Patterns 91
4.5.2 HREEL Spectra of NO and CO plus Ethylidyne 92
4.5.3 Structural Search and Results for NO and CO plus Ethylidyne 97
4.5.4 Discussion of the Ethylidyne Coadsorption Structures . . . 103
4.6 Conclusions 105

5 Diffuse LEED **108**
5.1 Introduction 108
5.2 Experimental 113
5.3 Pt(111) + Disordered CO 117
5.4 Theory 119
5.5 Structure Determination 121
5.6 Discussion 122
5.7 Conclusion 125

List of Figures

2.1 Schematic diagram of the video LEED chamber. 7
2.2 Photograph of digital LEED chamber. 8
2.3 Typical residual gas mass spectrum. 13
2.4 Universal curve of electron escape depths in metals. 17
2.5 Schematic of a typical electron gun. 19
2.6 Typical Auger spectra for Pt(111). 22
2.7 Schematic of retarding field analyzer. 24
2.8 Current *vs* voltage for a Varian LEED gun. 30
2.9 Typical video and digital LEED images. 33
2.10 Peak intensity *vs* count rate for DLEED detector. 38
2.11 Block diagram of digital LEED apparatus. 40
2.12 Position sensitive anode. 42
2.13 DLEED I–V curves for clean Pt(111). 45

3.1 I–V analysis flowchart. 55
3.2 Summary of NO stretching frequencies. 56
3.3 HREELS for NO on Rh(111). 57
3.4 Trial structures for the structural search of NO on Rh(111). 60
3.5 I–V curve comparison for NO and CO. 62
3.6 Final structure for Rh(111) + (2 × 2) 3CO. 63
3.7 Final structure for Rh(111) + (2 × 2) 3NO. 64
3.8 Surface structure for the (2 × 2) patterns drawn with van der Waals radii. 68

4.1 Surface structures of CO, NO, and ethylidyne on the Rh(111) surface. 75
4.2 Schematic diagram of CO plus benzene LEED patterns. 80
4.3 Approximate surface structures for CO plus benzene on Rh(111). . 81
4.4 HREELS of CO plus benzene on Rh(111). 84
4.5 Final structure for Rh(111) + (3 × 3) 2CO + benzene. 87
4.6 Schematic of pathways to *c*(4 × 2) 93
4.7 HREEL spectra of CO plus ethylidyne. 94

4.8 Summary of HREELS for ethylidyne coadsorption system. 95
4.9 Final structure of Rh(111) + $c(4 \times 2)$ CO + C_2H_3. 99
4.10 Final structure of NO + ethylidyne. 102

5.1 Digital LEED schematic. 114
5.2 Final DLEED data. 118
5.3 R–factor contour plot. 123
5.4 R–factor variation with site occupancy. 124
5.5 Thermal diffuse intensities from clean Pt(111). 126

List of Tables

2.1 Time for the adsorption of one monolayer(ML) of gas calculated from the kinetic theory of gases at different stages of vacuum. . . . 5
2.2 Video LEED Spot Failure Modes. 35
2.3 Comparison of Video and Digital LEED. 36

3.1 Summary of HREELS of NO. 49
3.2 Summary of structure search. 59
3.3 Final structural parameters. 59

4.1 Summary of the surface structures of CO and NO on the Rh(111) surface. 74
4.2 Summary of CO plus benzene sturctures. 89
4.3 Vibrational frequencies for NO, CO, and ethylidyne on Rh(111). . 96
4.4 Summary of the structures tested for the ethylidyne coadsorption systems. 100
4.5 Summary of final structural parameters. 101
4.6 R–factor summary. 103

Chapter 1

Introduction

What is a surface? Why would anyone want to study the structure of a surface? Throughout the world of science, there are many fields where the surface structure, directly or indirectly, influences the behavior of the system. Catalysis, diffusion through cell membranes, electrochemistry, and corrosion are all phenomena which involve reactions at or near the surface of a material. In semiconductor technology, and crystal or thin film growth, the structure and properties of the interface determine the characteristics of the device or system. Friction, lubrication, and wear are all governed by the interactions between *two* surfaces. It is the structure and properties of the surface chemical bonds which influence, or in some cases, completely determine the form and function in each of the above systems.

Surface science, the study of interfaces, can provide information on the structure, chemical identity, and bond strengths in the top few atomic layers of a material.

At its most fundamental level, heterogenous catalysis is the making and breaking of chemical bonds at a surface. Certain catalytic reactions are so intimately dependent on surface structure that simply changing from one crystal face of a metal to another reduces the reaction rates by many orders of magnitude (e.g.

ammonia synthesis over iron single crystals). Electrochemistry is the study of the reactions which occur at an electrode as the potential is varied. Since we can fix the external voltage of an electrochemical cell, we have the unique ability to stop the reaction before it is complete. Surface science has allowed the study of species at the electrode surfaces at various points during the reaction. Corrosion is yet another phenomena where surface science has made its mark by identifying chemical species and oxidation states in the initial stages of oxidation of metals like iron and aluminum.

Another interesting class of surface related phenomena is the unique electrical properties of semiconductor interfaces. As electronic devices become smaller and smaller the structure and properties of the junctions between different types of semiconductors and between metals and semiconductors become increasingly important. From the structure of the various reconstructed faces of silicon to the identification of trace impurities down to parts per trillion levels, surface science contributes to the understanding of this unique class of materials.

A third class of surface phenomena which surface scientists have just begun to examine, involves mass transport across interfaces. Surface science has already been used to study structure and adhesion of thin films by providing elemental composition at the interface, and it may yet be possible to study the nucleation and growth of crystals and thin films. Active transport and diffusion across cell membranes may even be amenable to study using new developments in surface science.

A final range of phenomena which depend on the chemical bonds formed when two surfaces are brought together is friction, wear and lubrication. A mechanical analogue of catalysis, friction is the resistance to motion caused by the breaking of chemical bonds between two surfaces in contact. New developments in surface science make it possible to measure the atomic forces between molecules even in the presence of a lubricating layer.

Despite the diversity of the many phenomena discussed in the preceeding paragraphs all of them have one central theme. The structure or the reactivity or the "chemistry" of the interface is an important part of the phenomena and surface science has, is, or will contribute to the understanding of them.

Surface science is the study of interfaces, the study of the making and breaking of surface chemical bonds. The topics discussed in this thesis lie mostly in the realm of catalysis, although the instrumental developments discussed in the final chapter will have ramifications in other fields. Low energy electron diffraction (LEED) has been used to determine the surface structure of various small molecules on the Rh(111) and Pt(111) surfaces. In one instance low temperature adsorption (40K) was used to stabilize unique bonding configurations, mimicking the higher applied pressures used in catalytic reactions. The structure of various ordered pairs of adsorbates was used to probe the structural effects one adsorbate can have on another. Finally new developments in theory and experiment were used to go beyond the requirement of long–range order in normal LEED to study the structure of disordered molecular adsorbates.

Chapter 2

Experimental

2.1 Introduction

The assortment of ultra–high vacuum and surface science paraphernalia is overwhelming. Its scope is only limited by the skills and imagination of the technical staff designing it. Even choosing the "best" surface analytical tool for a given problem from amongst the ever growing lists of acronyms can be difficult. In this chapter no attempt will be made to cover the large number of possible surface science techniques. Instead, the emphasis will be on a few general concepts about obtaining Ultra High Vacuum(UHV), some of the common surface analysis tools and the hardware necessary to implement them (*e.g.* Auger Electron Spectroscopy(AES)). A detailed discussion of Low Energy Electron Diffraction(LEED) will also be included as well as a number of very useful "tricks of the trade" to help those graduate students who will follow.

2.2 Ultra–High Vacuum (UHV)

Ultra–High Vacuum (UHV) is characterized by pressures below about 1x10^{-8} torr.

Method	Degree of Vacuum	Pressure	Time for 1 ML
Lungs	Atmospheric	760torr	1.3×10^{-9}sec
	Low	1.0	1.0×10^{-6}
Mech. Pump	Medium	1.0×10^{-3}	1.0×10^{-3}
Sorption Pump	High	1.0×10^{-5}	0.1
Ion Pump(no bake)	Very High	1.0×10^{-7}	10.0
Ion Pump(after bake)	Ultra High	1.0×10^{-10}	1×10^{4}

Table 2.1: Time for the adsorption of one monolayer(ML) of gas calculated from the kinetic theory of gases at different stages of vacuum.

There are two reasons why the production and maintenance of UHV is necessary for studies of surfaces. First, many of the surface analysis techniques use low energy electrons as probes; and the second, more important requirement, is impurity adsorption from the background gases.

Low energy electrons are ideal because their strong interaction with matter limits the mean free path. Since the electron penetration depth is limited to tens of Angstroms or less, the surface analysis techniques are sensitive to only the top few layers. Unfortunately ambient pressures of gases around the sample would make the production and subsequent detection of the electrons impossible. Pressures must be below $\sim 10^{-3}$ torr in order for the electrons to travel unimpeded from their source to the sample and ultimately to the detector.

Impurity adsorption must be minimized long enough to perform an experiment. At atmospheric pressure reactive surfaces are covered by adsorbed gases. In table 2.1 is collected the time for adsorption of a monolayer of gas at various pumping stages calculated using the kinetic theory of gases.(cf[1]) At 760 torr it takes about one nanosecond for a typical metal single crystal to be covered with a monolayer of adsorbed gas; however, if the pressure is at 1×10^{-10} torr there are about 10^4 seconds before a complete monolayer can adsorb to the surface. The second restriction on pressure is the practical reason for UHV.

2.2.1 Pumps

There are a variety of ways of attaining and maintaining UHV.(Refer to J.F. O'Hanlon, "A User's Guide to UHV."[2]) A brief description of the pumping units used in the video and digital LEED chambers follows.

The two chambers used in this work have three stages of pumping: (1) two sorption pumps, (2) an ion pump and (3) a titanium sublimation pump. A schematic diagram showing the stages of pumping in the video LEED chamber is shown in figure 2.1. Figure 2.2 is a photograph of the digital LEED chamber. Starting with the chamber at ambient pressures each stage of pumping is used to progressively bring the chamber to UHV. The various pumping stages and their vacuum ranges are shown in table 2.1. Stage 1, sorption pumps, can start at ambient pressures, but can only pump down to the 10^{-3}–10^{-4} torr range. Ion and titanium sublimation pumps, stages 2 and 3, are damaged if started at ambient pressures. Both pumps will readily start pumping at the lower limit of the sorption pumps and will reach about $5\text{x}10^{-7}$ torr within a few hours of switching them on. The lowest pressures, in the 10^{-10}–10^{-11} torr range, can only be obtained after the chamber and pumps have been baked.(see section 2.2.2)

A sorption pump is a high surface area cryopump. It consists of an aluminum cylinder loosely packed with Linde 5A molecular sieves or equivalent microporous material. The entire pump is immersed in liquid nitrogen and any gases in the chamber, with boiling point greater than 77K will condense out on the surfaces of the cold molecular sieve. For faster cooling, the pumps often have tubes running through them with copper vanes extending out in close proximity to the molecular sieves for better thermal conduction. Linde 5A is a typical choice because the

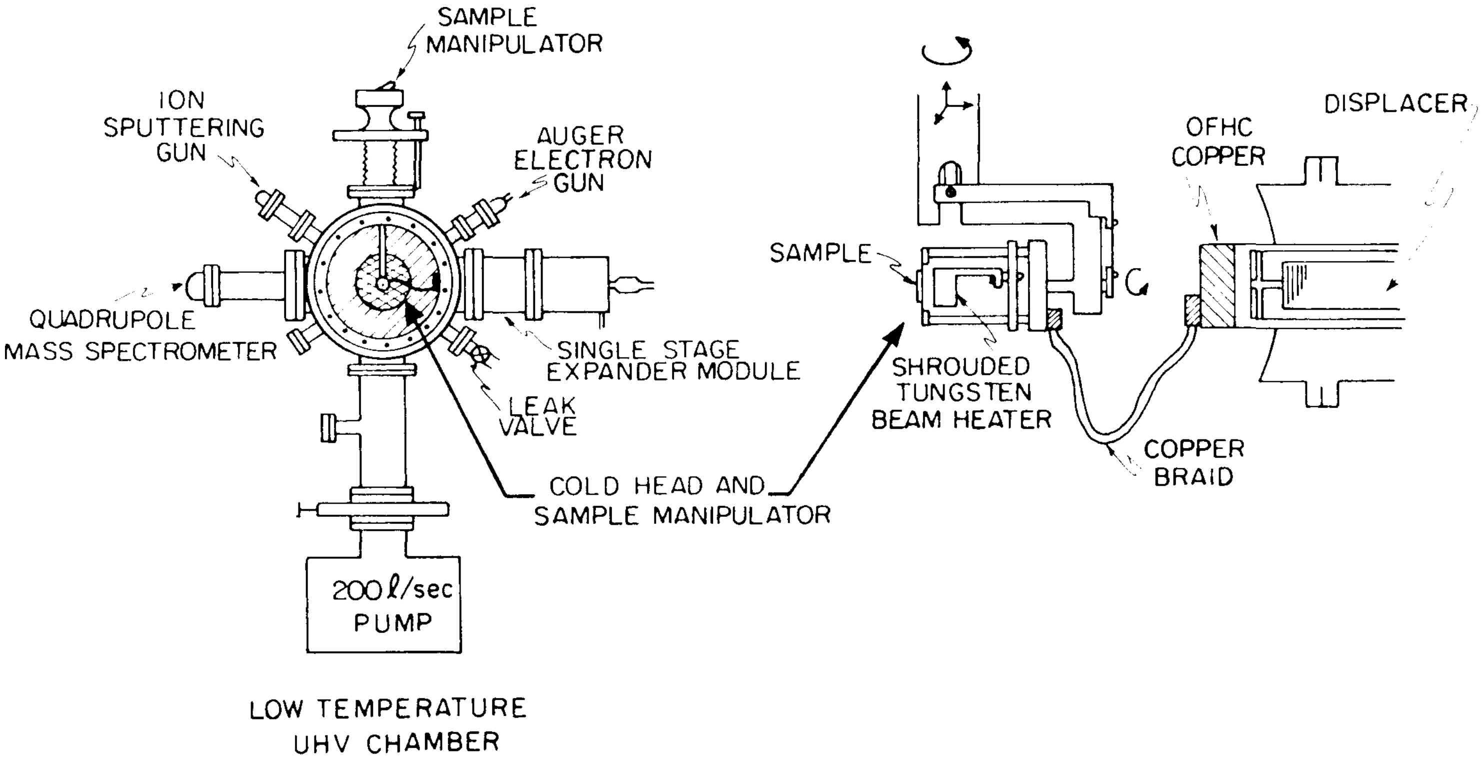

XBL 842-6607

Figure 2.1: Schematic diagram of the video LEED chamber with low temperature apparatus

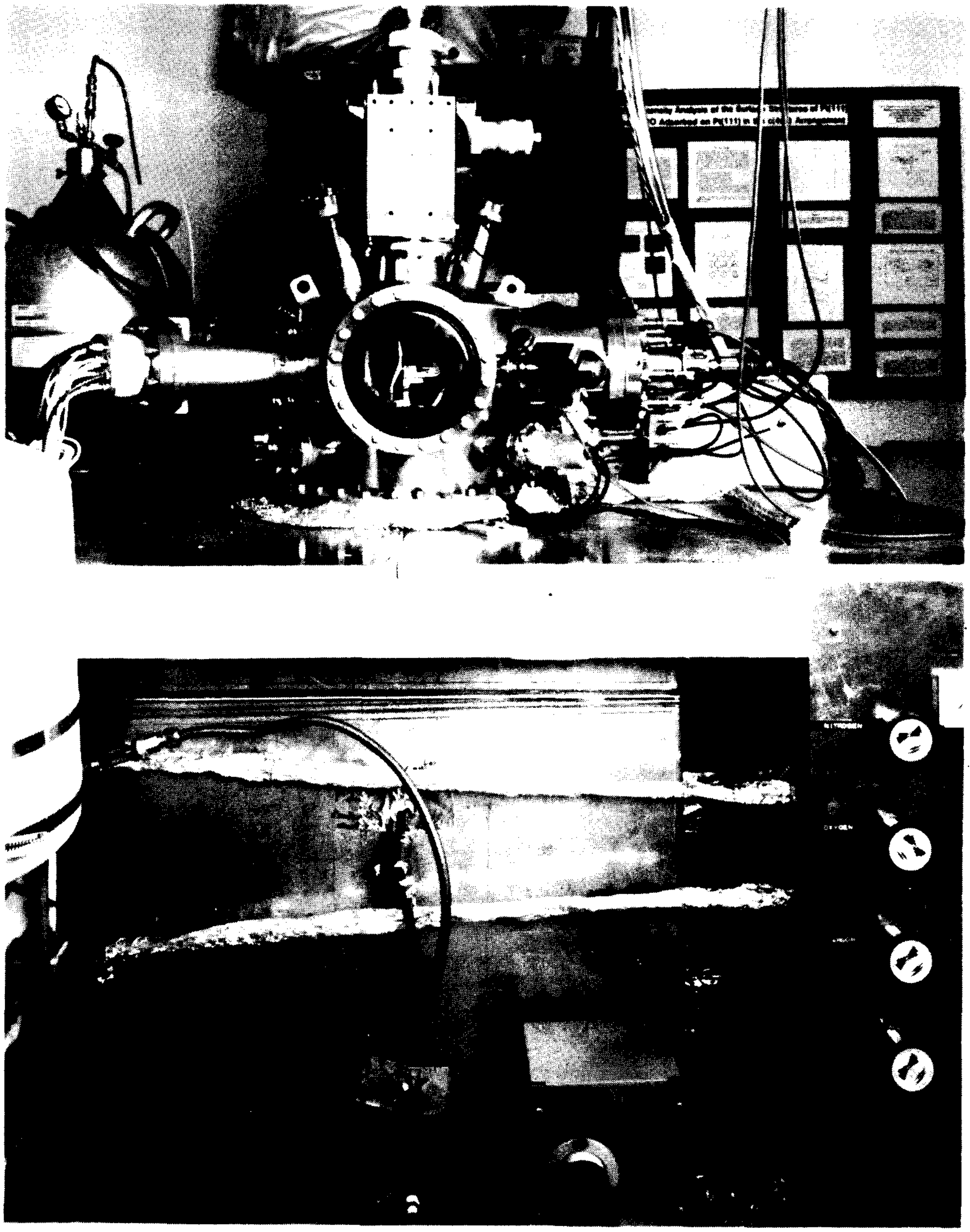

Figure 2.2: Photograph of the digital LEED chamber. The pumping units are concealed inside the stainless steel bakeout ovens at the bottom of the figure.

average pore size is about 5Å, a perfect size for trapping water. The pumping speed depends on the boiling point of the gas to be pumped. Water boils at 373K and pumps very well, whereas gases such as neon and helium (boiling points 27K and 4K, respectively) will not pump at all.

One method for removing some of the low boiling gases involves using two stages of sorption pumps.[2] The first pump is used until the pressure in the chamber reaches about ten torr at which point it is quickly valved off. Initially the velocity of the pumped gases is relatively high, and the low boiling gases are swept into the pump and trapped there when the valve is closed. The second pump will then attain a lower ultimate pressure in less time. Sorption pumps can be reconditioned by heating them to a temperature of 300°C for 4–5 hours. The high temperatures will desorb most of the pumped gases; and, unless there is hydrocarbon cracking within the sieves, they will be almost as good as new. In the event of coking, the dirty molecular sieves can be poured out and replaced by new ones. The lowest pressure that can be reached by sorption pumps is about 10^{-3}–10^{-4} torr and can only be reached after they have been well baked.

Just as the sorption pumps reach their limit, the ion pump can be started. A configuration known as a triode pump is a common and efficient all purpose ion pump. It consists of one anode sandwiched between two cathodes all placed between the poles of a permanent magnet (1000 gauss). Electrons are accelerated from the cathode to the anode by a potential of 5–6keV, but they follow spiral paths due to the presence of the strong magnetic field. The increase in path length of the electrons increases the probability of collision and ionization of a residual gas molecules. The ions in turn are accelerated in spiral paths and ultimately collide with other gas molecules or the electrode surfaces. If the energy of the ion is high enough it will crash into the surface of the electrode and react with the fresh titanium thus exposed or bury itself. Gases such as oxygen, carbon oxides and nitrogen are pumped by reaction with titanium. Noble gases such as argon and neon are pumped by burial. Reaction with titanium is a fast and relatively permanent means for removing residual gases. The burial mechanism is less efficient and less permanent which accounts for the low pumping speed of the noble gases.

Hydrogen is a difficult gas to pump, because it is small and light. Hydrogen does not have sufficient mass to pump well by burial and even though it does react with titanium to form a stable hydride it is constantly being replenished by diffusion through the chamber walls. As an ion pump ages the electrodes become saturated with hydrogen and trying to pump any other gas releases more hydrogen into the chamber. The problem is exacerbated by attempting to do argon sputtering with an ion pumped system.

The electrodes eventually become saturated with hydrogen so that when any other ion hits the walls hydrogen is liberated. The hydrogen background can become orders of magnitude higher than any other gas. Measures must be taken to remove the excess hydrogen. One method to rejuvenate an ion pump is to use an auxiliary pump (a diffusion or a turbo pump) to pump away hydrogen while sputtering the walls of the ion pump with argon. With the ion pump on and the auxiliary pump valved off the chamber pressure is increased slowly to 10^{-6} torr in argon. As the pressure is increased the high voltage in the pump will ionize the argon and the resulting ions crash into the electrode surfaces and liberate H_2. The hydrogen background will immediately start to rise and the electrodes will start to heat up. As the pressure rises the valve to the auxiliary pump should be opened and the argon flow reduced to keep the pressure stable. As the sputtering continues, hydrogen will be given off and eventually the argon can be shut off entirely and the hydrogen pressure will remain high. By cycling the system up and down in pressure a few times and pumping away the resultant gases with another pump the ion pump can be regenerated and the hydrogen background reduced considerably. In addition the sputtering of the electrode surfaces will remove other scale and impurities allowing lower ultimate pressures.

An ion pump can not last forever. There is only a finite supply of titanium on the electrode surfaces which eventually wears out. When this occurs the base pressure will stay high even after a bake out and it will be necessary to disassemble the pump and clean and re–coat the electrodes. Ion pumps can last many years if treated carefully.

The final stage of pumping is the titanium sublimation pump (TSP). This pump is usually used to remove reactive gases liberated while cleaning the crystal, or to obtain the last order of magnitude in pressure. It does just what the name implies; a filament made from a Ti/Mo alloy is heated until the Ti sublimes. Such pumps usually have a water or liquid nitrogen cooled jacket to condense the titanium vapor and to assist in pumping. The only mechanism for removing gases for a TSP is by reaction with titanium, therefore only reactive gases such as O_2, H_2O, and CO are pumped well. Inert gases like Ar and He are not pumped at all. Hydrogen can be a problem for a TSP, because it becomes saturated just like an ion pump. If a TSP has been exposed to air, it should be briefly flashed during the initial stages of pumping down to eliminate some of the water and hydrogen adsorbed to the filaments.

2.2.2 Bakeout

After the initial pump down, assuming the chamber does not have any leaks, the ultimate pressure is limited by the rate of desorption from the walls of the chamber. For most systems the largest peak in the residual gas spectra is water and the pressure is seldom better than 5×10^{-7} torr. While all of the chemisorbed species on the walls would eventually pump away, it would take a prohibitively long time. Since desorption can be thermally activated the best way to speed up the process is to increase the temperature of the walls of the chamber. Chambers are typically baked to 150–250°C for 12–48 hours. When complete, the chamber pressure will drop to around 1×10^{-10} torr. A residual gas spectrum for a well–baked, ion pumped system is shown in figure 2.3. The large hydrogen peak is common for stainless steel UHV chambers and is due to H_2 permeation through the metal walls.

2.3 Cleaning procedures

Even after bakeout the crystal surface can be covered with impurities. Each type of single crystal presents slightly different impurities and thus slightly different cleaning procedures.(See reference [3] for a review of cleaning procedures for over 70 different materials.) The identity and quantity of the impurities depends on how the sample was prepared, and how carefully it was handled prior to its introduction to UHV. For example, the sudden appearance of calcium after mounting a crystal can be the result of the use of rubber gloves with talcum powder on them. Likewise, chlorine is a major constituent of fingerprints so touching a sample with bare hands can result in chlorine contamination. The most common method for checking surface cleanliness is Auger Electron Spectroscopy (AES). It is most convenient if Auger can be done at the same time as the cleaning cycle to assess the efficacy of the method.

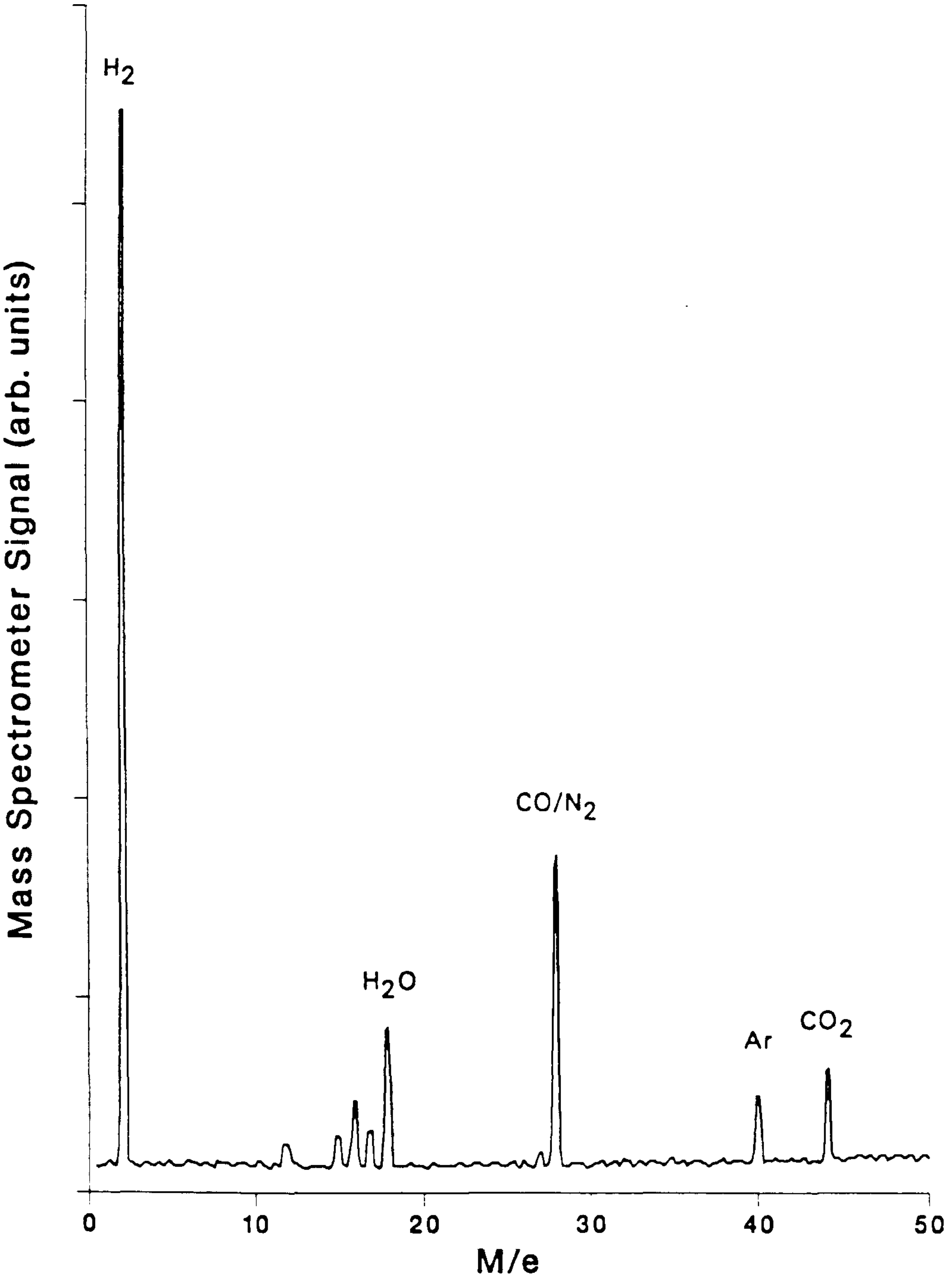

Figure 2.3: Typical quadrupole mass spectrum of an ion pumped UHV chamber after bakeout. The predominant gases are H_2, CO or N_2, and H_2O.

Common impurities for the rhodium and platinum crystals used in these studies (carbon, sulfur, boron, silicon, calcium) could be removed using cycles of heating in oxygen, argon sputtering and annealing. The oxygen treatment is usually performed by bringing the chamber up to $1\text{x}10^{-7}$ torr and then heating the crystal to 650–750°C . This treatment can remove most of the carbon residue, because the carbon reacts with the gaseous oxygen to yield carbon monoxide. The process can be monitored with a mass spectrometer (the CO peak at mass 28 will decrease as the carbon residue is depleted) or directly by AES (see section 2.5.1). For rhodium the temperature of oxygen treatment is important, because carbon can diffuse into or out of the bulk.

Argon sputtering is the atomic analogue of sandblasting. The chamber is backfilled with argon gas which is ionized by a hot filament then accelerated to crash into the sample. It is a destructive cleaning technique especially if the ion current or the voltage is large. Typical parameters are: an argon pressure of $1.0\text{x}10^{-5}$ torr, beam voltage of 3keV, 25 milliamps emission current, and roughly 10microamps of beam current. Under optimum conditions sputter rates of a thousand Angstroms per minute can be achieved with a normal Varian sputter gun; however, if the beam is rastered or defocused much lower rates can be obtained. Even using a gentle, low voltage beam causes some damage to the surface. The amount of damage can be assessed by noting the width of the electron diffraction spots. The width of the spots is related to the amount of disorder on the surface and they become fuzzy and diffuse after sputtering. Sputtering removes more difficult impurities like Ca and Si.

One of the more insidious problems with sputtering is, "How do you know when you are hitting the crystal with the beam?" The easiest way is to monitor the crystal current and maximize it during sputtering. However, a current measurement is impossible or meaningless when the crystal is permanently grounded or not isolated from the rest of the manipulator. In that case the most certain way to align the sputter gun is to watch one of the impurity signals with AES while adjusting the gun electronics and sample position. Under optimal conditions monolayers of impurities can be removed in seconds. If the chamber design does not permit simultaneous sputtering and AES, there is still another option. With the voltage as high as possible on the sputter gun, and the pumps valved off, bring the argon pressure in the chamber up into the $5\text{x}10^{-5}$ torr range. With all the lights in the room off and dark adapted eyes it is quite easy to see the characteristic blue emission from the excited argon ions at 488nm. The last option is harder on the chamber, but it only needs to be done once to optimize the sputter gun settings and crystal position.

After sputtering the crystal, it is necessary to anneal to high temperatures. The objective of annealing is to provide enough thermal energy to the surface atoms for them to diffuse to more favourable sites, thus flattening the surface, and repairing the damage caused by sputtering. Temperatures in the range of 80% of the melting temperature are typical. Difficulties may arise when heating to this temperature, because diffusion from the bulk can replenish the impurities that were just removed. Many cleaning cycles may be necessary to deplete the near surface region of its seemingly inexhaustible supply of impurities.

One method for depleting the near surface region of stubborn impurities is to heat the crystal to a point where the diffusion of bulk impurities to the surface is at a maximum and maintain this temperature while sputtering them away. If all else fails the crystal may have to be removed from UHV and etched in a suitable acid, or heated in a furnace (vacuum, hydrogen or air depending on the impurity). For example silicon etches away well in solutions of hydroflouric acid, and boron can be removed by heating in hydrogen.

One particularly effective cleaning procedure for Pt(111) consists of elements of all three of the above techniques. Ion pumped systems do not pump argon very well. If they are operated during argon sputtering large amounts of other impurity gases can be liberated which can decompose on the crystal and make it dirtier than it was before cleaning. Oxygen on the other hand is pumped very well by ion pumps. Oxygen ions are very reactive and they can be produced using a normal sputter gun. An appreciable flux of oxygen ions is generated by bringing the chamber up to $1\mathrm{x}10^{-6}$ torr in oxygen with the sputter gun on. Even the most stubborn carbon impurities instantly melt away when hit by oxygen ions. Afterwards the ion pump removes every trace of the oxygen from the chamber in a very short time leaving a clean surface with a low background pressure.

2.4 Electron Guns

The strong interaction between low energy electrons and matter makes them extremely surface sensitive; therefore, many of the techniques for surface analysis use electron beams as a probe. Figure 2.4 shows the so called universal curve or mean free path for electrons *vs* energy. Note that at 50eV, the minimum of the curve, the escape depth for electrons incident on a surface is only 5Å or just over one atomic layer. High resolution electron energy loss spectroscopy, AES, and LEED depend on the production of a well focused beam of electrons with energies between 0 and 5keV. In this section a few of the methods for producing such a beam will be discussed.

The generation of an electron beam requires a source of electrons, and lenses for focusing and collimating the beam. In some cases deflector plates for aiming

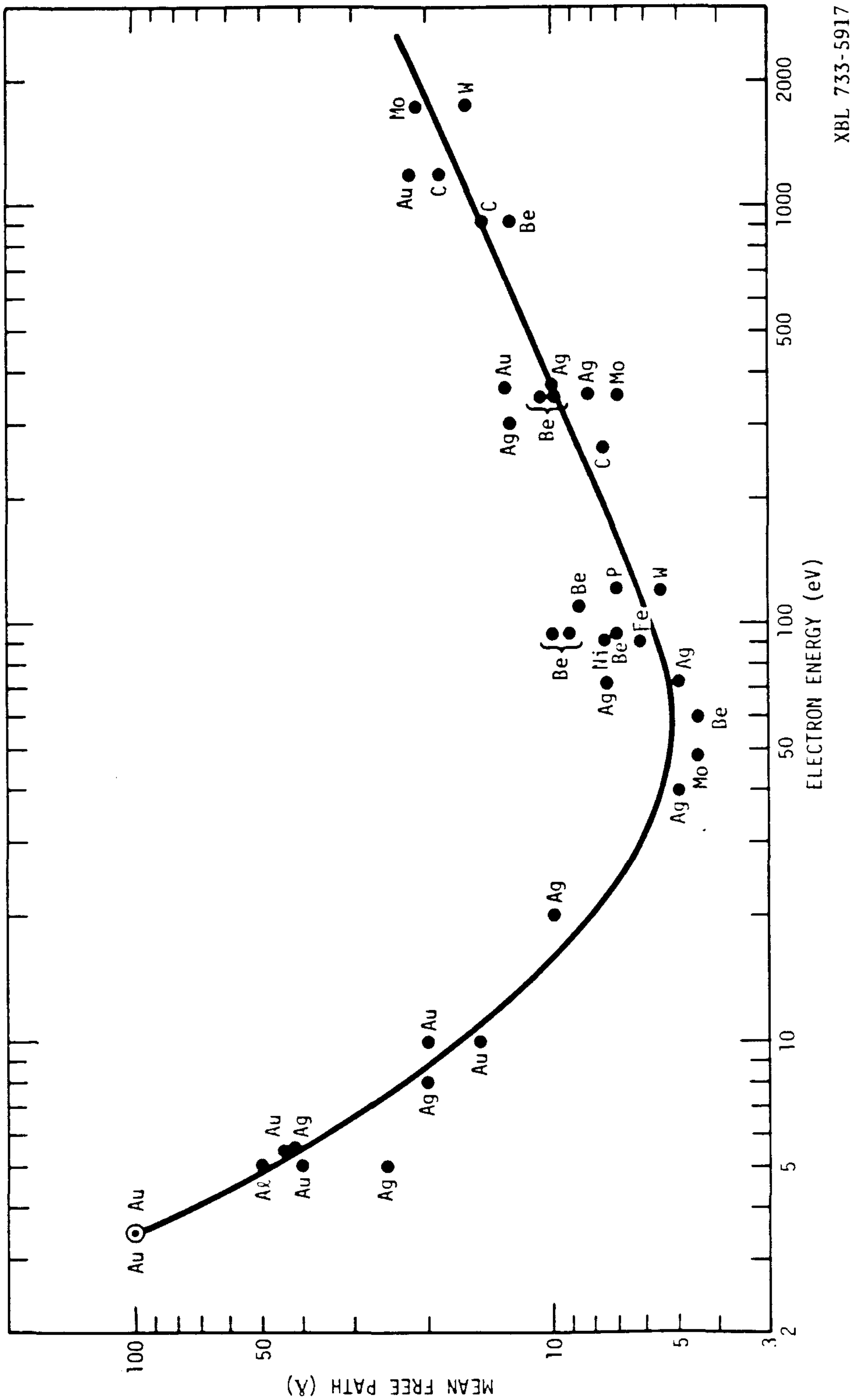

Figure 2.4: Escape depths *vs* energy for electrons in metals.[4]

the beam are also included. Figure 2.5 shows a schematic diagram of a typical LEED electron gun and a plot of the potentials at various points throughout the gun. The source of electrons is commonly an indirectly heated tungsten/barium aluminate "matrix" cathode, but directly heated thoriated iridium or tungsten hairpin filaments are also common. The cathode is heated to a temperature high enough for appreciable thermionic emission (1500K for matrix, 1800K for thoriated iridium, and 2000K for tungsten) by passage of a current of several amps through the filament. The cathode will generally be at the same potential as the beam voltage.

A hot filament emits electrons in all directions, so the first lens element must gather the electrons into a thin beam. The first lens element is called a "Wehnalt" or repellor and it completely surrounds the filament with a 1–2mm diameter hole for the electrons to escape. The next three elements are collectively called an Einzel lens and consist of either stacked concentric tubes as shown in figure 2.5 or as three separate coaxial cylinders.

The potentials applied to the different lenses serve to extract and focus the electron beam. The repellor lens is usually biased negative with respect to the filament(V_B). The first element of the Einzel lens is at ground. The electric field between the two extracts the electrons from the filament. Since the electrons near the filament have low kinetic energy, they follow the field lines and are focused and collimated as they escape from the aperature of the Wehnalt. As the electrons move towards the Einzel lens they accelerate to the beam voltage and most of them pass through. The next element is the focus lens and it is usually biased to about 70% of the beam voltage and rides upon it. The third member of the Einzel lens is also at ground (0.0 volts). In addition some guns have two mutually perpendicular deflector plates along the central axis for aiming and moving the electron beam.

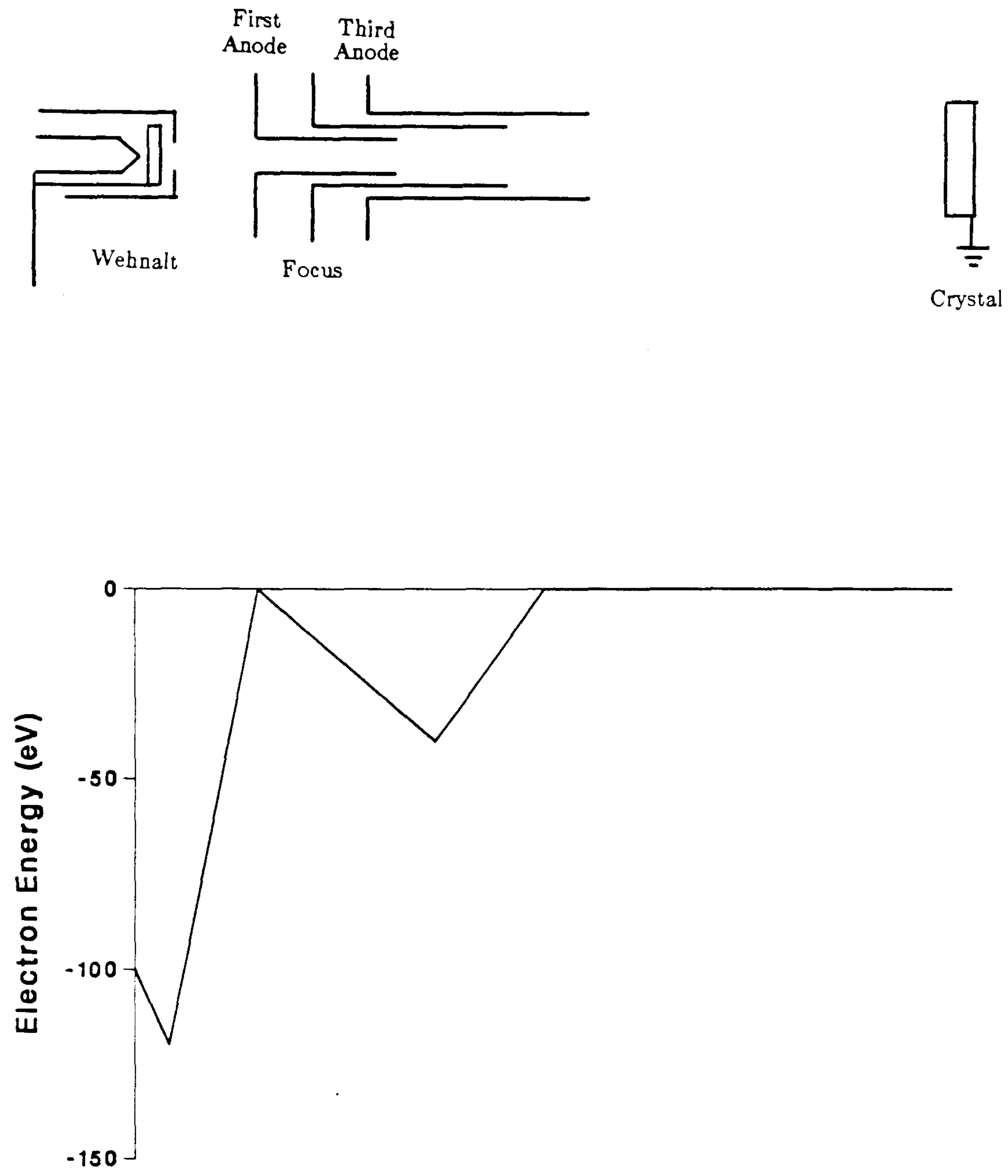

Figure 2.5: Schematic diagram of an on–axis LEED electron gun with an emitter cathode source.

The first and third anodes are both hooked to a plate with spring clips on it that makes contact with the gun shield, to provide a connection to ground. The digital LEED gun is different in that it has a total of five lens elements.[5] In between the repellor and the Einzel lens is a small (30 micron) beam limiting aperature which is located precisely at the first cross over point of the electrons. The various potentials for the operation of the digital LEED gun will be discussed in section 2.6.

Another common source of electrons for LEED is called an off–axis electron gun. This gun has the filament assembly displaced from the central axis and a deflector to bring the electrons back to the center.[6] The off–axis configuration removes the hot filament from line of sight to the crystal eliminating the twin problems of high light levels inside the chamber and desorption of impurities from the hot filament onto the sample. A well adjusted off–axis gun can provide microamps of current down to 10eV and as high as several kilovolts with little change in focus of the beam.

2.5 Techniques

2.5.1 Auger Electron Spectroscopy (AES)

Auger Electron Spectroscopy is used to determine the elemental composition of the near surface region of the crystal. It is difficult, but not impossible, to make the technique quantitative. Absolute concentrations down to 1% of a monolayer can be measured reliably if some standard is used to calibrate the Auger peak ratios (For example a known LEED structure at a certain coverage). Two particularly good references for the technique are Briggs and Seah[7] and Ertl and Küpper[8].

The Auger process is a two electron process which results in the emission of an electron with energy that is characteristic of the atom from which it came. (See figure 2.6 for a typical spectra.) The most common form of AES uses an electron gun (usually the type with coaxial cylinders) to begin the process; although photons and even high energy ions can be used.[9] The incident electrons have energies between 500 and 5000eV (the rule of thumb is to use an energy three times that of the highest energy Auger transition in the spectra.) Inner shell electrons in the atoms at the surface are kicked out, creating a hole that is subsequently filled by an electron from a higher level. The energy released by the collapse of the outer electron to fill the hole can be released as a photon (x–ray fluorescence) or by the emission of a second electron (the Auger process). The energy of the Auger electron depends only on the relative energy levels of the atom from which it came, and can be used as a fingerprint for that elemental species (figure 2.6). Each peak in an Auger spectra corresponds to a single transition and is labeled by the three levels taking part in the process. For example, the peak at 272eV in the top spectrum of figure 2.6 is from the carbon KLL transition; that is, the original hole was in the K–shell and both the electron that dropped down to fill the hole and the ejected Auger electron are from the L–shell. The energy of the transition is therefore approximately:

$$E(KLL) = \mathcal{E}_{\mathcal{K}} - \mathcal{E}_{\mathcal{L}} - \mathcal{E}^{*}_{\mathcal{L}}$$

The first two terms, $\mathcal{E}_{\mathcal{K}}$ and $\mathcal{E}_{\mathcal{L}}$, are the energies of the K and L shells for carbon, respectively. The last term, $\mathcal{E}^{*}_{\mathcal{L}}$ is the energy of the L shell perturbed by the presence of a hole in that orbital.[8]

When the kilo–electron volt incident beam hits the surface elastically scattered electrons, secondaries, and inelastically scattered electrons are emitted in all direc-

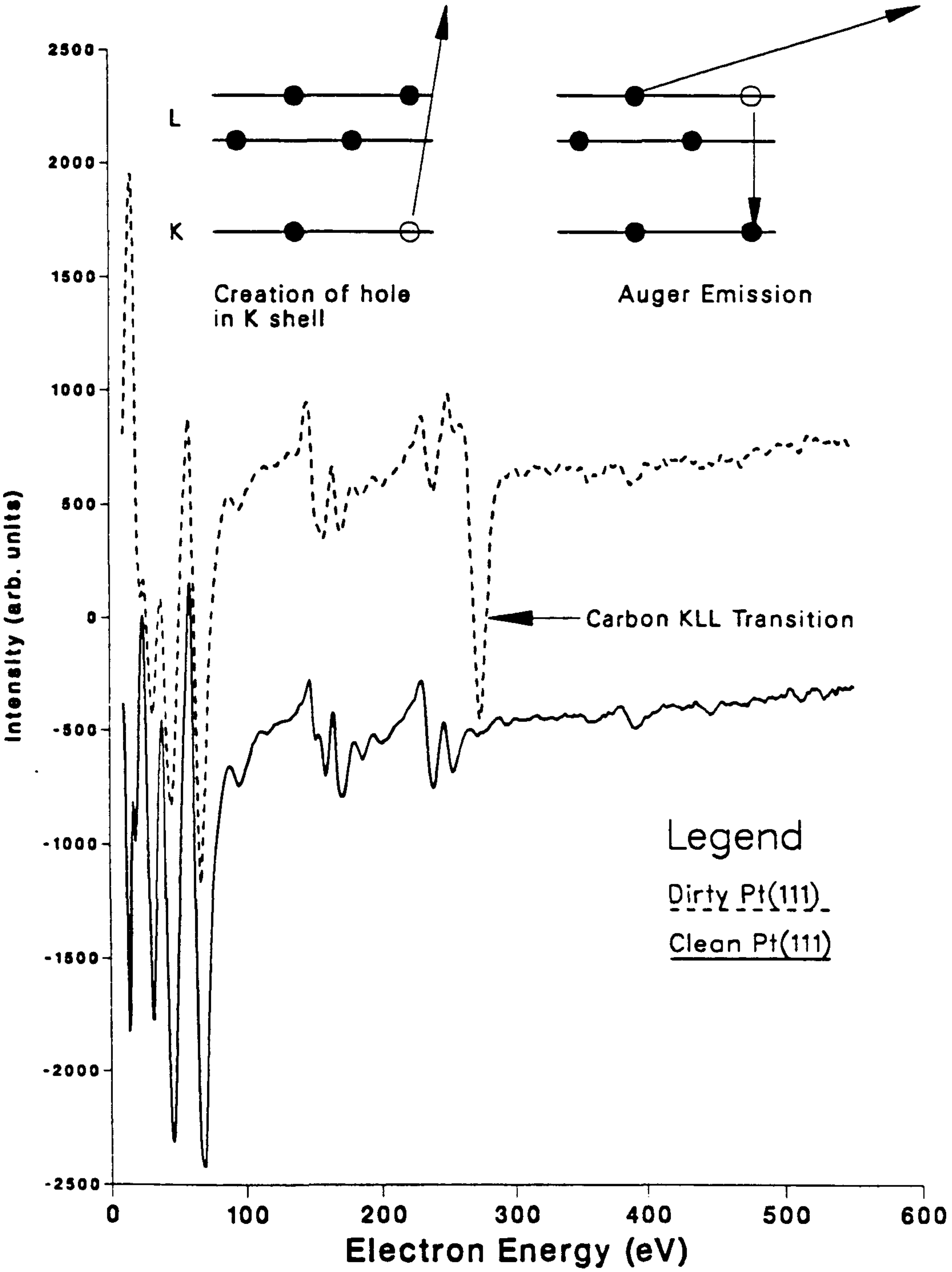

Figure 2.6: Auger spectra for clean Pt(111) and Pt(111) plus carbon impurity, collected with a single pass CMA.

tions. The electrons are collected and energy analyzed by one of two basic means: a Retarding Field Analyzer(RFA), or a Cylindrical Mirror Analyzer(CMA).

The RFA uses four concentric hemispherical grids for energy selection and a phosphor covered metal screen to collect the electrons. Figure 2.7 is a schematic diagram of a typical RFA configuration for doing Auger. The phosphor covering is not necessary for AES but is used for LEED (described in the next section). The RFA collects the electrons from a 45–60° solid angle. The first grid (the one closest to the sample in figure 2.7) is at ground to provide for a field free region near the crystal. The next two grids are internally connected and are collectively called the suppressor. The suppressor grids are where the energy selection process occurs. They act as a high pass filter, in that they will allow all electrons of higher energy to pass on to the collector and repell any electrons below the potential applied to them. The potential on these grids is typically ramped from 20–2000eV. The fourth grid is grounded. This is necessary in Auger to remove capacitive coupling between the metal collector and the suppressor grids. The metal collector is usually biased with +300V to more efficiently collect the electrons.

The Auger electrons are difficult to distinguish because they are superimposed on a slowly varying background of inelastically scattered primary electrons and other secondaries. Lock–in detection can be used to improve the signal to noise and to electronically provide the derivative signal thereby making the Auger peaks easier to measure. To make use of lock–in detection a small AC signal (2–10V_{p-p}) is applied to the suppressor grids. The frequency is around 3kHz and is chosen simply to minimize noise from external sources. The signal from the collector, which is now modulated, is passed through a capacitor which blocks the DC and passes the AC component. The AC signal is fed into a lock–in amplifier which selects only the component of the input signal which has twice the frequency of

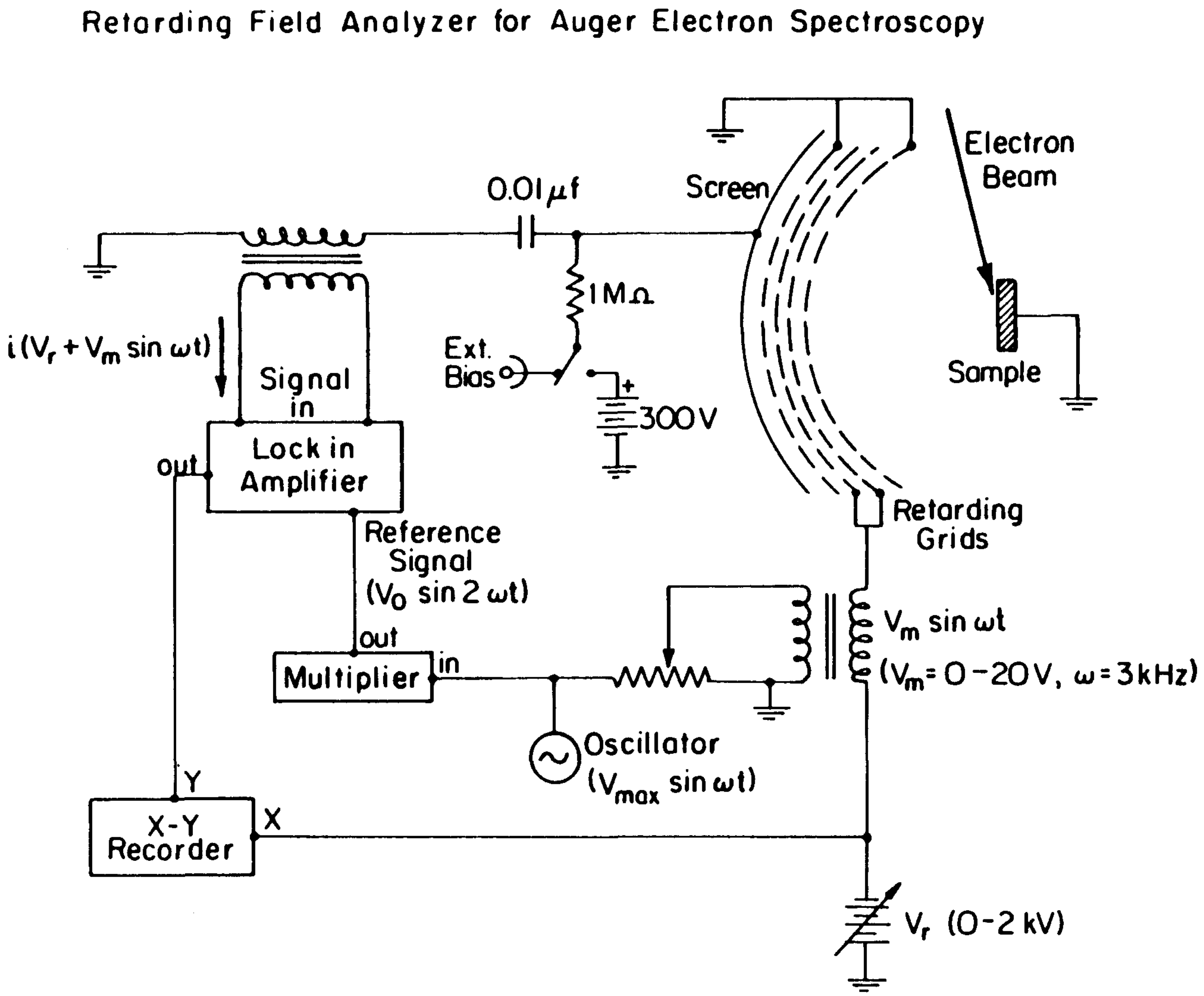

XBL 842-6631

Figure 2.7: Retarding field analyzer in Auger mode.

the reference signal thus producing the derivative $\frac{dN(E)}{dE}$.

The reason that $\frac{dN(E)}{dE}$ is proportional to the signal component with twice the frequency is shown below. The collector current at a given energy is the sum of all of the electrons above the suppressor voltage at that energy:

$$i(U_s) \propto \int_{E=eU_s}^{\infty} N(E)dE$$

therefore

$$\frac{di(U_s)}{dU_s} \propto N(E)$$

The collector current is modulated because of the modulation applied to the suppressor grids. Expanding the current in a Taylor series gives:

$$\begin{aligned} i(U_s + U_m \sin\omega t) &= i(U_s) + i'(U_s) \cdot U_m \sin\omega t + \frac{i''(U_s)}{2} \cdot U_m^2 \sin^2\omega t + \ldots \qquad (2.1) \\ &= i(U_s) + i'(U_s) \cdot U_m \sin\omega t + \frac{i''(U_s)}{2} \cdot U_m^2 \left(\frac{1-\cos 2\omega t}{2}\right) + \ldots \\ &= i(U_s) + \frac{i''(U_s) \cdot U_m^2}{4} + i'(U_s) \cdot U_m \sin\omega t - \frac{i''(U_s) \cdot U_m^2(\cos 2\omega t)}{4} \\ &\quad + \ldots \qquad (2.2) \end{aligned}$$

The first two terms are constant DC currents and will be blocked by the capacitor. The component with frequency ω is proportional to the first derivative of the current and therefore proportional to N(E). The component with frequency 2ω is proportional to the second derivative of the current and therefore proportional to $\frac{dN(E)}{dE}$. A lock-in amplifier can be used to select the component of the current at ω or 2ω to give either N(E) or the more familar $\frac{dN(E)}{dE}$. Use of the lock-in to give the derivative signal has the advantage of a high degree of noise rejection and improved sensitivity for the small Auger peaks on the high secondary electron background.

Another means for energy analysis of the secondary electrons is a Cylindrical Mirror Analyzer(CMA). A CMA consists of two concentric cylinders with a small electron gun on the central axis of the cylinders. The biggest advantage of a CMA over a RFA is that a CMA is a dispersive energy analyzer, that is it lets only a small energy range ΔE around E through at any given energy. Allowing only a small band width through to the detector reduces the noise considerably. The inner cylinder is at ground and the outer cylinder is ramped through the voltage range such that the narrow band pass of energies scans the desired energy range. The electrons which make it through are collected by a channeltron or by an electron multiplier at the exit side of the CMA. The resolution of the CMA depends on the size of the exit annulus.

The current from the channeltron is modulated by an AC voltage applied to the outer cylinder, just as with the RFA. However, because the CMA is a dispersive energy analyzer the signal component with the same frequency as the modulation is proportional to the $\frac{dN(E)}{dE}$.

$$i(U_s + U_m \sin \omega t) \approx i(U_s) + i'(U_s) \cdot U_m \sin \omega t \propto \frac{dN(E)}{dE}$$

Both methods of electron detection, RFA and CMA suffer from some of the same problems. The measured signal level depends on the incident current and the magnitude of the modulation voltage. Increasing the modulation voltage will increase the signal at the expense of the resolution. The scan speed will also affect the resolution. For maximum resolution the modulation voltage should be low and the scan speed slow.[10] The biggest advantage of a CMA over a RFA is that the CMA is a band pass filter and lets only a small number of electrons through with energies ΔE around E so the noise is considerably reduced. The result is that the typical signal to noise ratio for a CMA is 100 times better than for a RFA which means, faster scan rates or lower incident beam currents can be used. [8]

2.5.2 Low–Energy Electron Diffraction (LEED)

The majority of surface scientists use LEED as a simple tool for checking the cleanliness, order, and symmetry of the surface. It works very well for this purpose, and conditions can be far from optimum (unknown angles of incidence, unknown electric and magnetic fields, unknown currents) and still provide the required information. However, the complete surface structure can only be determined by an analysis of the LEED intensities and comparison to theory.

Collecting reliable intensity *vs* voltage or I–V curves requires a careful and meticulous experimentalist. In this section methods for optimizing the experimental apparatus for surface structure studies will be discussed. A brief introduction to the video technology and software used to reduce the raw data to final form will also be presented.

In the earliest days of LEED, in the 1930's, the only way to obtain diffracted beam intensities was to use a faraday cup to collect the electrons. A Faraday cup is a grounded canister with a small aperature for the electrons to enter and a positive collector inside. Linear motion feedthroughs were used to adjust the position at each energy to find the diffracted beam. At the time even attaining UHV was a difficult process and very few people entered the field.

Two major developments, one in experiment and one in theory, were to usher in a renaissance for LEED. A major theoretical problem for LEED was that it did not follow normal (x–ray) diffraction rules. In the case of x–rays, all features of the diffraction process with angle or energy could be explained using a single scattering or kinematic theory. The I–V curves collected for electrons had peaks shifted from their kinematically predicted positions and even new peaks growing in that could not be explained at all with a single scattering formalism. Something else was needed.

The something else was provided by Ean McRae who first put together a dynamical or multiple scattering theory for LEED in 1956.[11,12] McRae's model for calculating the electron diffraction amplitude from a crystal consisted of the following. The incident wave was treated as a plane wave of known wave vector. An electron absorption or damping term was included to model all of the inelastic processes (*e.g.* phonon and plasmon excitations). He broke the crystal into two parts, the topmost part consisted of every layer which was different from the bulk. The rest of the crystal was the "substrate" which had complete bulk periodicity. The diffraction amplitudes for each layer were calculated in turn. The incident wave field on underlying layers consisted of the sum of the transmitted incident plane wave and any scattering which occurred in previous layers. The total diffracted wave field was the sum of the diffraction amplitudes from all of the layers. McRae's dynamical LEED theory is the basis for all of the current theories for low–energy electron diffraction.

The major development in the experiment that brought LEED within the reach of every surface scientist was the post acceleration LEED which was invented by Ehrenberg in 1934[13], but not developed to its present form until the early 1960's by Scheibner *et al.* [14] and Lander *et al.* [15] In its simplest form it consists of two concentric hemispherical grids with the crystal located at the precise center. The first grid is at the same potential as the crystal (usually ground) to insure a field free region near the sample. The next grid is the suppressor grid and floats a few volts below the incident beam voltage to repel any electrons that have lost energy when they interacted with the surface of the sample. Behind the second grid and concentric with it is a metal screen coated with P–11 or P–22 phosphor.

The screen is biased to 3–5keV and the electrons accelerate so that when they strike the screen they excite the phosphor to give a bright spot. The light emitted from the phosphor is peaked in the blue at a wavelength of 460nm for P–11 or in the green at 525nm for P–22 phosphor.

Most LEED apparatus' are equipped with a total of four grids so that the same set–up can be used for Auger and LEED (although two grids can be used for both.[16]) The first grid is at ground, grids two and three are internally connected and act as the suppressor and grid four is either grounded or externally tied to the suppressor grids. (In Leed it makes little difference whether the fourth grid is at ground or at the suppressor voltage because the next potential the electrons experience is the screen voltage at 5keV.)

The production of reliable I–V curves for structural determination requires that the power supply settings be optimized. There are several important steps in the process that are described below. The steps are qualitatively similar to those used for digital LEED.

The video LEED gun is an off–axis type with a tungsten hair pin filament, and the potentials of the various elements must be adjusted carefully to produce bright sharp spots over the entire energy range of the experiment (20–300eV). First the incident current should be linear with beam voltage (later in the data analysis this known calibration will be used to normalize the I–V curves). The deflector bias, filament current and extractor voltage all affect the beam current. If the deflector bias and extractor voltage are adjusted to give a maximum current at the high end of the desired energy range the beam current will be close to linear. Typical currents are in the range of 1–5μA.(see figure 2.8)

The next step is to adjust the focusing elements, the suppressor voltage and the screen potential. With a stable well-ordered LEED pattern (the clean surface

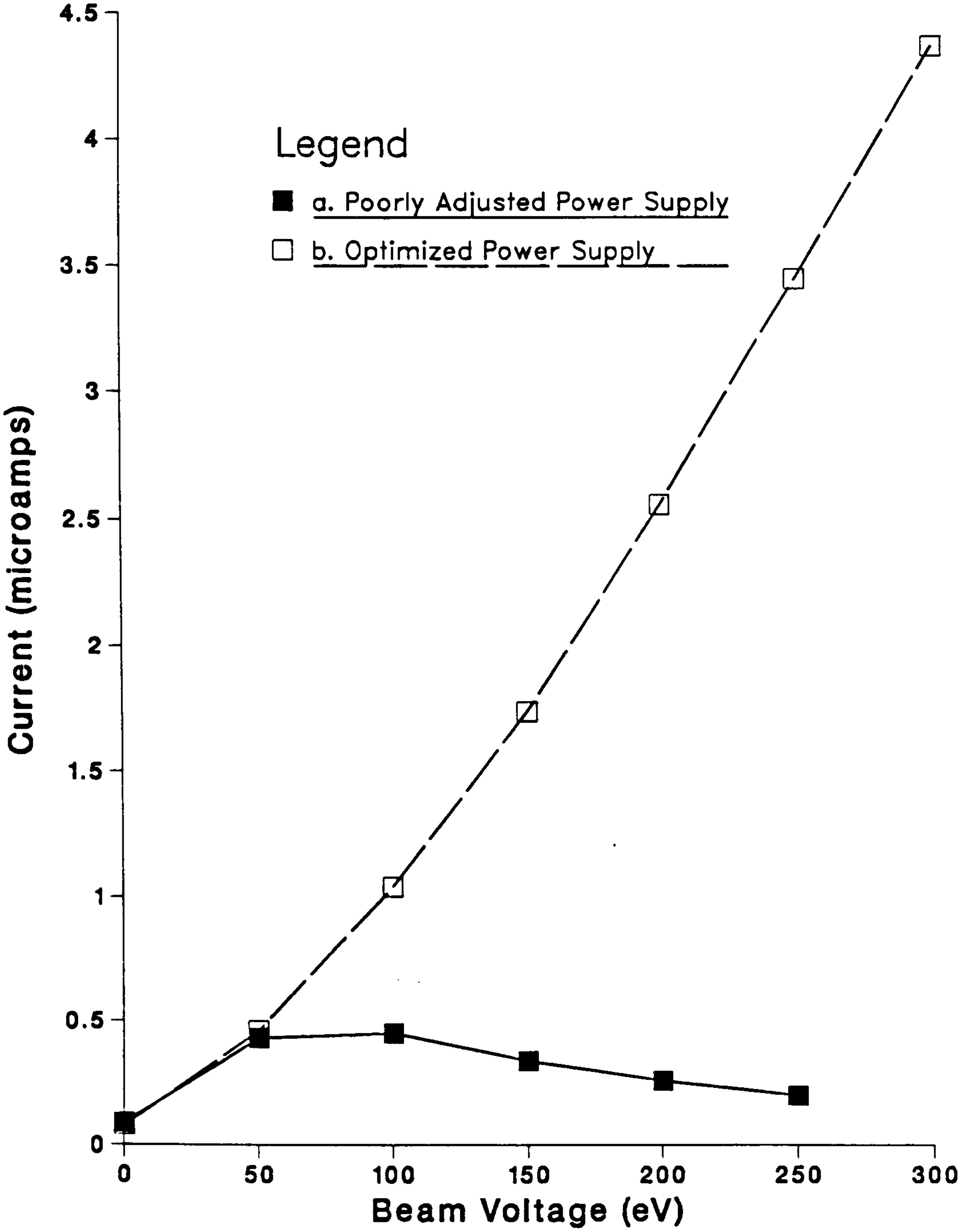

Figure 2.8: Current *vs* voltage characteristics for a Varian LEED power supply. Curve *a* shows a poorly adjusted supply and curve *b* shows one with optimum settings.

works quite well) visible on the screen adjust the focusing and the extractor voltage to obtain the sharpest brightest spots. Now adjust the voltage to get a large number of spots on the screen. Slowly increase the suppressor voltage until all of the spots vanish. If the crystal is not at the center of the grids the spots will not vanish all at once, instead they will vanish either from the outside in, or from the inside out. Once the crystal is in the correct position relative to the grids, decrease the suppressor voltage until the spots are the sharpest and the background is the darkest. Finally increase the screen voltage as high as possible without getting arcing. The larger the screen voltage the brighter the spots will be for a given beam current.

The LEED power supply on the video LEED chamber has been modified to allow computer control of the beam voltage. The computer also controls the video camera to synchronize the data collection. For all of the video work presented in this thesis a standard panasonic vidicon camera with a cadmium zinc telluride target was used to store an image of the phosphor screen on a video tape recorder for later analysis. The entire data collection takes only three minutes for roughly 100 energies. The computer generates labels and timing signals at the start of each energy so that the video processing hardware can synchronize the grabbing and digitizing of the images. Much of the development of the video LEED technique was done by Ogletree *et al.* [17,18]

Our video processing hardware was obtained from Imaging Technologies[19] and is controlled and operated by a LSI 11/23 computer on a Q–bus. The system consists of five boards: one analog processor (AP-512), one arithmetic logic unit (ALU-512), and three frame buffer boards (FB-512). The AP reads the data stream from the video source at video rates of 10MHz and converts it to digital form for storage in the frame buffers. Each image consists of 480 horizontal lines with 512 vertical pixels along each horizontal line. The origin is set at the upper left corner following video conventions. Each FB board has a 512x480 pixel memory with an 8 bit intensity for each pixel. Two are hooked together for a total of 16 bits to store the working image at a given beam voltage. The third board contains a background image consisting mainly of camera dark current for background subtraction. The ALU board is responsible for simple mathematical operations such as subtraction, addition and multiplication at video speeds.

The sequence of events for grabbing and analyzing an image is as follows. Sixteen frames are usually averaged together to improve the signal to noise ratio. The operator indicates which frames to grab by pressing the return key just prior to the flag for the desired energy. The ALU board takes care of the averaging operation by simply summing the frames one after another as they come in then rolling them back four bits (in essence dividing by 16). The working image is stored in the first set of FB boards and camera background or dark current is stored in the other FB. The background subtraction is done with a MACRO routine though it should be possible to speed it up by performing the subtraction with the ALU, but that option has not been implemented yet. The images can be artificially enhanced for ease in picking out weak beams. The whole video processor package is controlled by a set of MACRO subroutines called by the main program. A typical video image before background subtraction is shown in the bottom panel of figure 2.9. The large background is due to the camera dark current.

The main program is in FORTRAN–77 and has been set up for the production of I–V curves from the raw video images with very little user intervention. The user inputs a set of criterion such as minimum and maximum allowable spot widths, minimum signal/noise ratio etc. which the computer can use to judge whether a spot is to be considered "good" or not. The user also inputs the initial spot

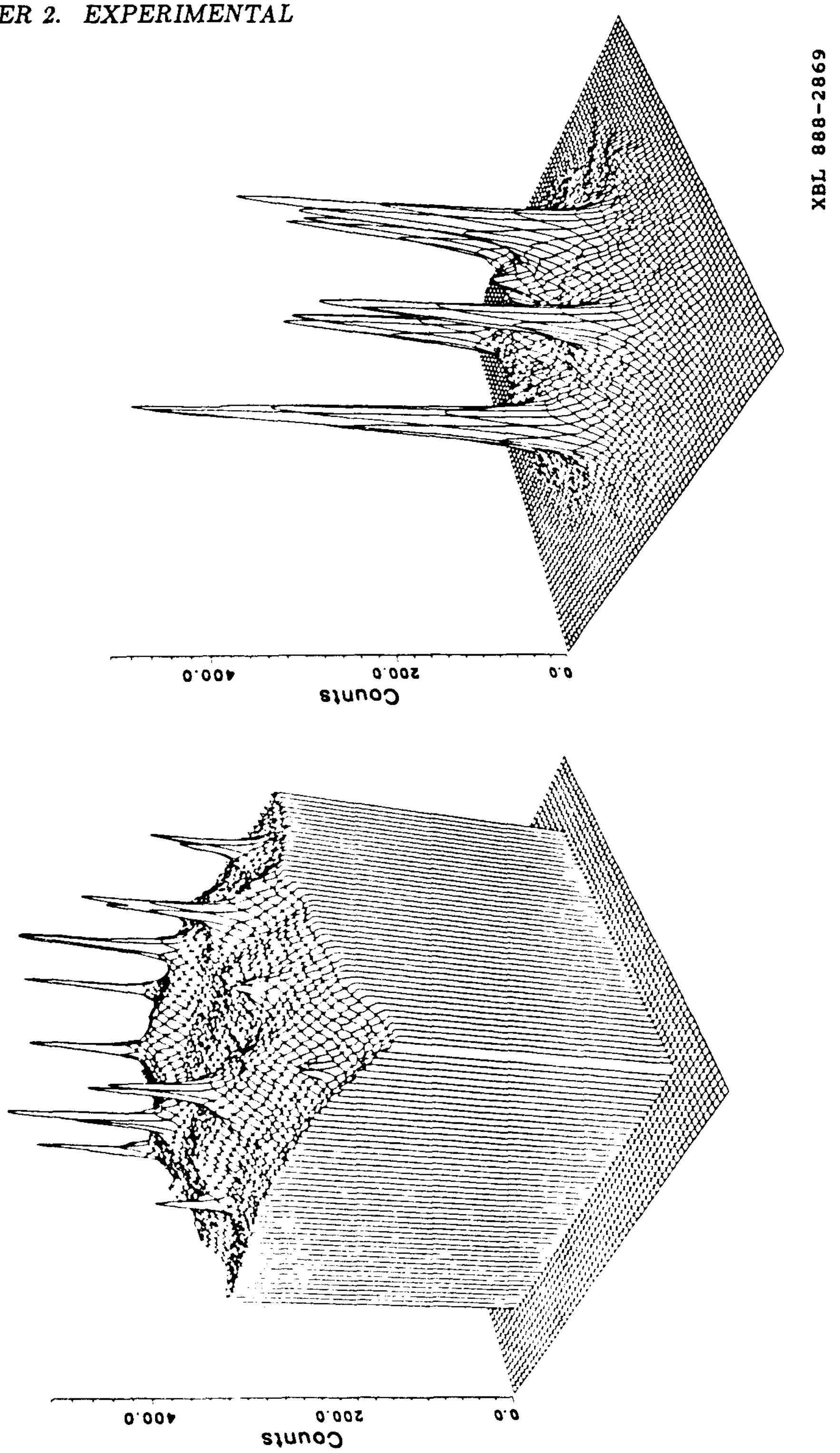

Figure 2.9: Quasi 3-dimensional plots of typical video (bottom) and digital (top) LEED patterns. The video LEED image is of clean Rh(111) at 30K. The image has been scaled such that the video and digital LEED saturation levels are equal. The digital LEED image is of clean Pt(111) at 160K. Compare the large dark current from the video camera with the negligible level for the digital detector.

positions at the starting energy. The computer calculates the unit cell parameters at this energy and uses them to determine spot positions at the next energy. By updating the unit cell parameters at each energy the computer can reliably track the spots as they move across the screen.

The spot analysis is accomplished by reading in a small region (25x25 pixels) centered on the predicted spot position, then searching the region for a local maximum in intensity. If a local maximum is found then the region is recentered about this spot. If not then the region is not moved and this spot fails. A summary of all the failure modes is in table 2.2. Once a spot has been located a local nine–point smoothing routine is carried out, followed by a calculation of the local background. The spot intensity is determined by adding up any intensity, greater than background, for each pixel within the elliptical integration area. Based on a set of user supplied criterion a decision is made about whether to include this spot intensity in the data set. If the intensity is strong enough the spot position will be used in a regression analysis to update the unit cell parameters for calculation of new spot positions at the next energy.

The user can exert many levels of control over the process. Manual mode requires the user to drive a cursor to a region near the spot each time and then after the computer displays the intensity in this region the user can decide whether the spot is a good one or not. Complete auto mode only requires the user to provide the working image and the background and everything else is performed automatically. The latter mode is used most and is reliable and fast. A flowchart of the software package is included in the appendix.

In a typical experiment the LEED power supply should first be adjusted as discussed earlier in this section. In addition the angles of incidence must be known to within ±0.2° . The easiest way to do this is by adjusting the angles to ob-

IFAIL	Reason for Failure
-120	Spot has drifted too far beyond calculated spot position in Y direction.
-110	Spot has drifted too far beyond calculated spot position in X direction.
-100	Calculated spot position is outside detector.
-90	User decision to reject spot.
-80	Sum of all pixels > (NOISE + BACKGROUND) is less than or equal to 0.0.
-70	User decision to use default spot position.
-60	Spot width is less than minimum (IWX0) in Y direction.
-50	Spot width is less than minimum (IWY0) in X direction.
-30	The intensity of the spot is less than a near–by pixel.
-20	The highest intensity pixel in the region around the calculated spot position is less than NOISE.
-10	All pixels in the search area have zero intensity.
0	Spot is intense, use for data and for unit cell calculation.
100	User decision to use for data, but not for unit cell calculation.
200	Spot is weak if integrated intensity is < SNLIM, use for data, but not for unit cell calculation.

Table 2.2: Flags for spot failure modes in the video LEED analysis routines.

	Video LEED	Digital LEED	Consequences
Incident Current Exposure	$\sim 1\mu$A 130 e^-/unit cell	$\sim$ 1pA 2.5×10^{-3} e^-/unit cell	Surface structural analysis of insulating surfaces and beam sensitive overlayers.
Maximum s/n for a typical LEED spot	75	66 for 1 sec 207 for 10 sec ...	Adjustable signal to noise ratio, extreme sensitivity, → Diffuse LEED

Table 2.3: Comparison for video and digital LEED for a typical experiment.

tain equivalent intensities in symmetry equivalent spots at normal incidence. One procedure is to increase the energy to a point in the I–V curves where one set of symmetry equivalent spots is at an intensity minimum. If the angles are off then the spots will go through this minimum at different energies so by carefully adjusting the angles while cycling through the intensity minimum, normal incidence can be quickly determined.

2.6 Digital LEED

The Digital Low–Energy Electron Diffraction (DLEED) apparatus was originally developed to study beam sensitive overlayers on metal surfaces. Many of the interesting ordered structures are damaged by the large incident beam currents ($\sim$1-5μA) used in the conventional post acceleration LEED. The DLEED apparatus uses incident beam currents of $\sim$1pA which eliminates any possibility of beam stimulated problems. In table 2.3 is a point by point comparison for video and digital LEED.

Digital LEED has other advantages over video LEED. In video LEED the camera itself has a significant dark current. Even without any light incident on the silicon target the signal is as much as 8.0mV. Since the maximum signal level is only about 0.75V the maximum signal to noise ratio is only ~80–100. Even in a single I–V curve the intensity can saturate near the maximums and it can drop into the noise at low intensities. The difference in s/n ratio is shown pictorially in figure 2.9. This figure has video and digital LEED images side by side. The video image has been scaled so that the saturation levels are equal for the two methods. The video LEED data is superimposed on the considerable camera dark current.

The digital LEED detector has almost negligible dark current. With no electrons incident on the crystal the total count rate is less than 100cps over the whole detector. In the region of a typical spot, say a 2x2mm square, there will be less than 0.1cps dark current. The peak intensity for a single pixel *vs.* total count rate for the digital LEED detector is shown in fig 2.10. The output from the detector is linear up to a total count rate of about 22kHz. In the local region around a typical spot the maximum count rate is about 4.3kHz. The signal to noise ratio for pulse counting depends only on $\sqrt{N}$, where N is the total number of counts in the image. At the maximum count rate the S/N ratio is 66 for 1 second, 207 for 10 seconds etc. DLEED can easily "see" features in the background intensities or weak features in I–V curves which would be completely undetectable by conventional LEED. This is the single most important aspect of the new digital LEED and is what enables the study of disorder and of insulating surfaces.

The electron gun power supply and digitizing electronics were all built at Lawrence Berkeley Labs.[20] Figure 2.11 is a block diagram of the DLEED detector and electronics. The electron gun (commercially available from Clifftronics[5]) uses a thoriated iridium filament directly heated by a DC current of 3–4Amps

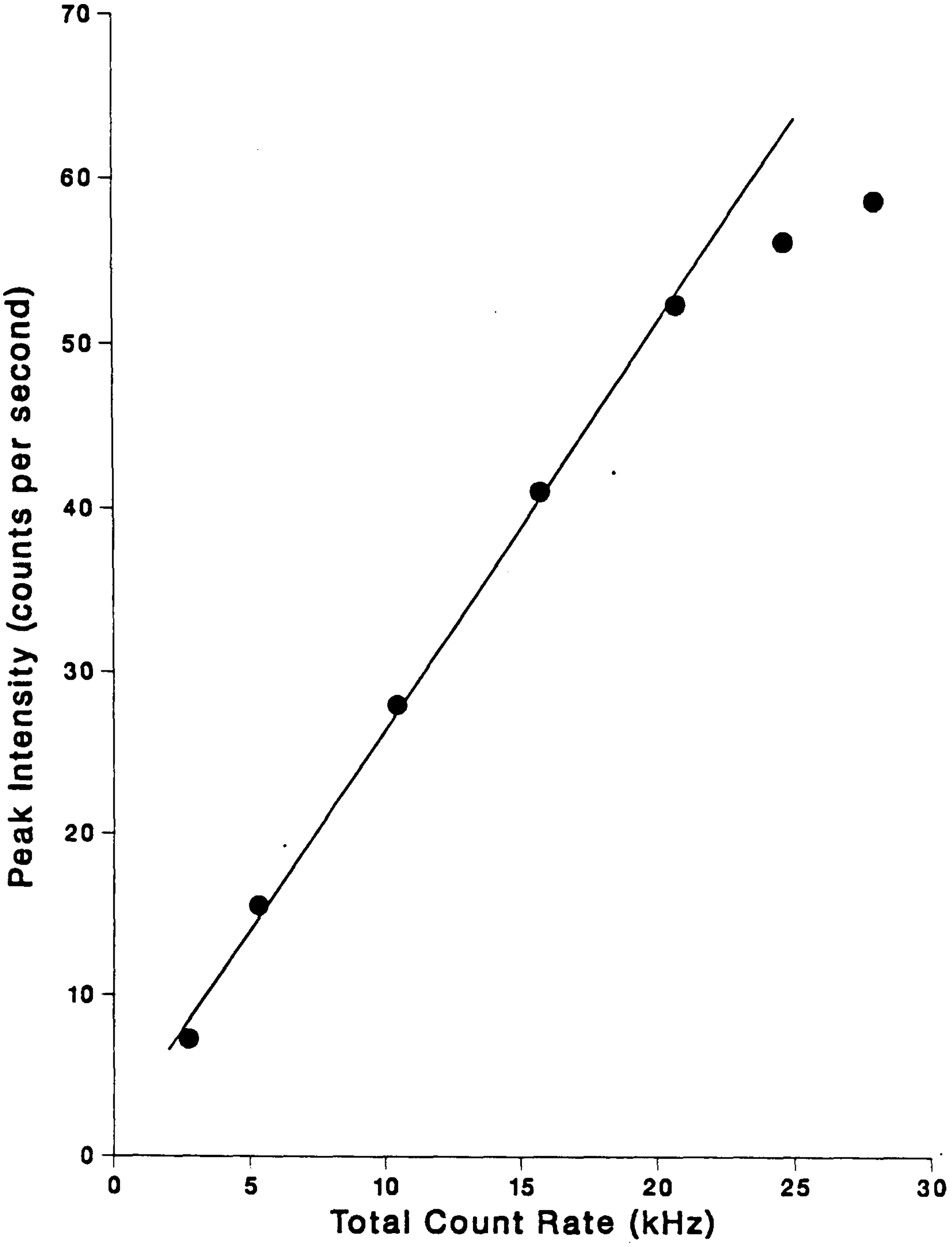

Figure 2.10: Peak intensity in a single pixel *vs* total count rate for the specular beam. The output is linear up to a total count rate of about 22kHz. Data is collected well below this value.

as a source of electrons. The repellor voltage on the "Wehnalt" can range from 0 to negative 100V with respect to the filament. A typical value for generating picoamps of incident beam current is negative 12–18volts. The first anode is precisely located at the cross over point of the beam and has a 37 micron beam limiting aperature. The potential on the first anode is the extraction voltage for the electron beam and can be adjusted in the range of positive 300–400eV. This voltage is kept constant during an experiment to keep the beam current constant. The next three lenses are in the Einzel configuration described previously and accelerate or decelerate the beam to give the correct beam voltage. The condenser lens and acceleration voltages can be computer controlled.

The electron gun supply also controls the biasing voltages for the energy selection grids, the microchannel plates, and the wedge and strip detector described below. Energy selection is done using three grids from a small PHI LEED optics. The first grid is grounded , the second has the suppressor voltage applied to it:

$$V_s = \alpha V_{beam} - \delta V$$

where α ranges from 0.8 to 1.0 and δV ranges from -10 to +10 volts. Both α and δ can be adjusted by turning a potentiometer on the front of the power supply. The last grid is held at the potential of the front surface of the first channel plate so that all electrons hit the channels with the same kinetic energy eliminating the problem caused by the variation of quantum efficiency with energy. Unfortunately this configuration causes the images to be radially distorted as well as introducing a problematical variation in angle of incidence for the electrons. Both of these problems can be eliminated by redesigning the detector to change the potential on the front of the channel plates.

Each microchannel plate[21] consists of a 7.4 cm diameter glass plate about

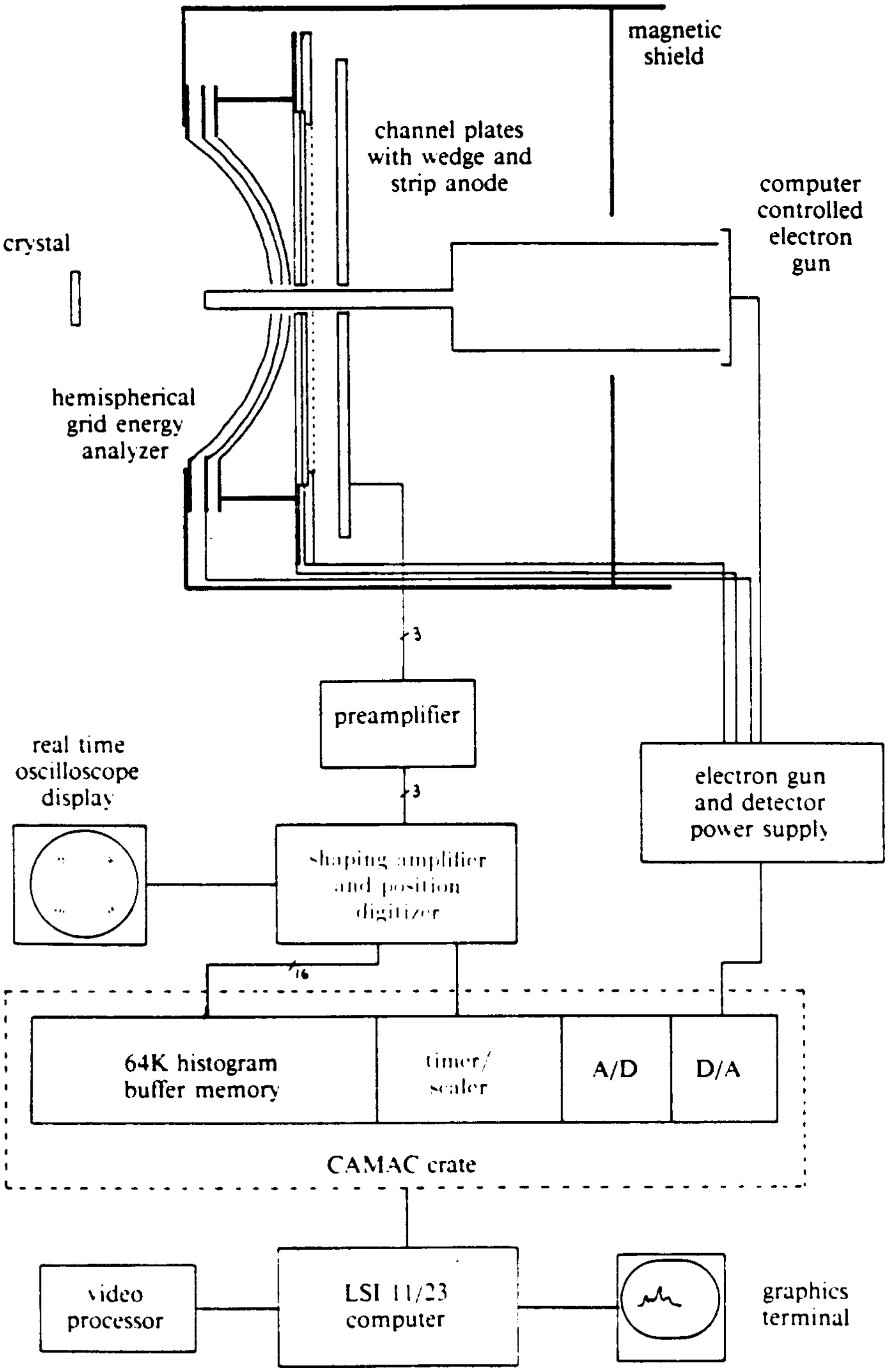

XBL 8512-5024

Figure 2.11: Block diagram of digital LEED apparatus.

3mm thick with channels 25 microns in diameter arranged in a hexagonal array 32 microns apart all across the surface. Each channel is inclined at an angle of 8° with respect to the surface normal. Two microchannel plates are used in a chevron array (opposing bias angles, see figure 2.11). The configuration reduces ion feedback at higher pressures because the electrons can easily follow the field lines while the more massive ions cannot.

Both channel plates are biased at ~1000eV per plate and are capable of amplifications as high as 10^8. The newest microchannel plates which are currently in the detector are the fastest ones that were available at the time. The speed is limited by how fast the channels can recharge after firing a pulse and this is limited by what is known as the strip current. The strip current is the current drawn from the power supply used to bias the channel plates and can be as high as 280 microamps.

One diffracted electron incident on the front of the first channel plate gives a pulse containing hundreds of millions out the back. About 6mm behind the microchannel plates is the position sensitive detector. We use a wedge and strip anode made by a photo–lithographic technique out of pure copper on a quartz flat substrate. On the left side of figure 2.12 is a schematic diagram of the interleaving wedges and strips. The wedges (electrode A) are wide at the top and get narrower towards the bottom. The strips (electrode B) are thicker on the left and get progressively thinner towards the right. Electrode C wends its way through between the other two electrodes and collects most of the remaining incident electrons. There is a five micron gap of quartz between each electrode. The period for the wedge and strip pattern is 1.5mm so the copper covers about 88% of the total surface area.

The eight bit x and y coordinates of the centroid of the charge pulse are calcu-

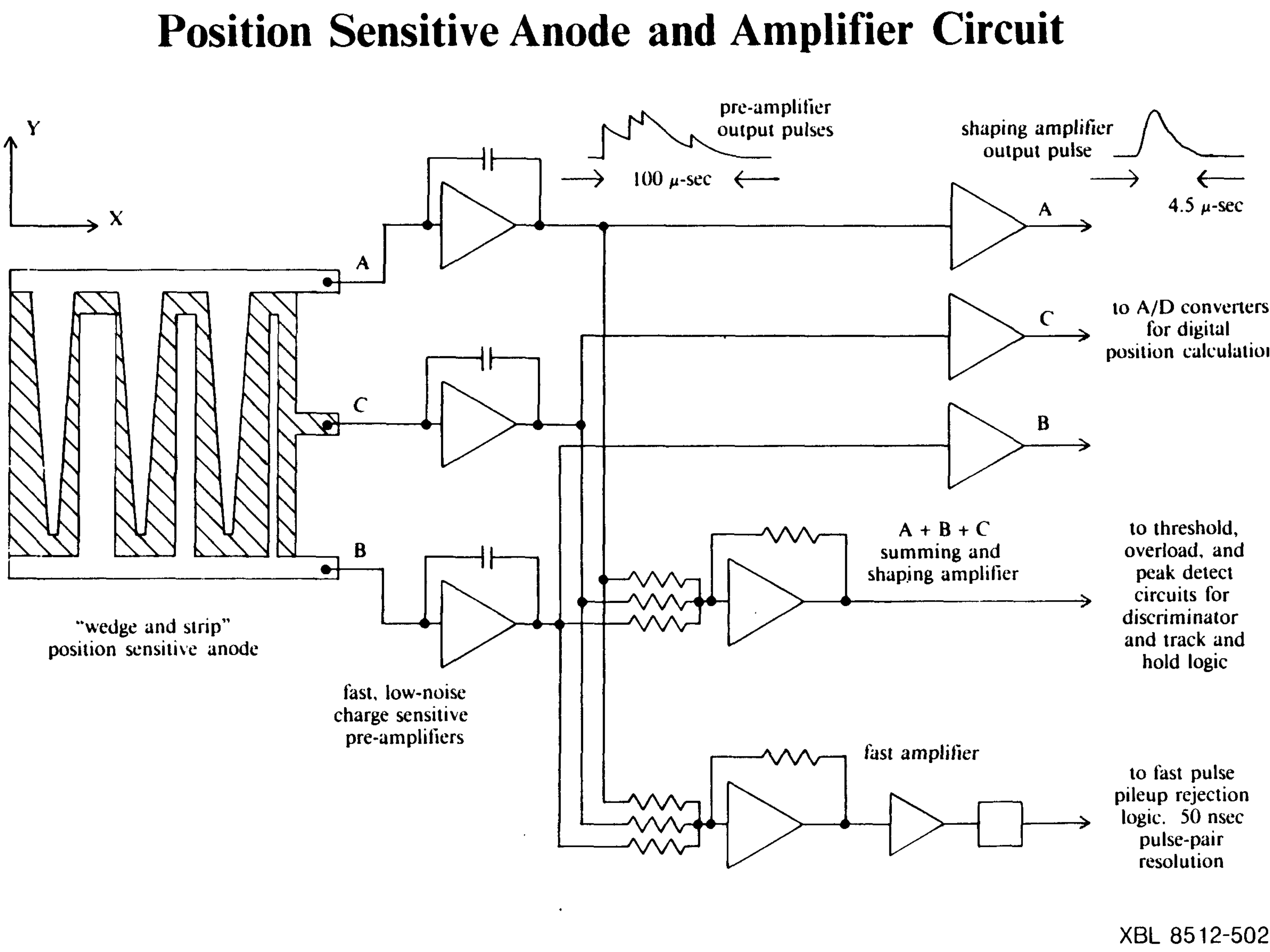

Figure 2.12: Schematic of the wedge and strip position sensitive detector and amplifier.

lated by taking ratios of the outputs of each of the three electrodes. For example as the charge pulse moves from left to right across the anode a lesser and lesser percentage of the total charge comes out on electrode B(strips), so by taking the ratio of the B output to the total (A+B+C) the x-coordinate of the pulse can be calculated. Similarly as the pulse moves from top to bottom less and less of the charge exits on electrode A (wedges). A ratio of output A to the total gives the Y component of the pulse. The rise time for these pulses is only 50ns because of the low resistance of the all-metal electrodes.

A pre-amplifier is located as close as possible to the chamber to reduce the amount of noise picked up by the leads. The front end of the pre-amp floats at about +2600V and the pulses are passed across a blocking capacitor and then amplified. The size of pulse from each electrode can be adjusted so that they are equivalent for an equal sized test pulse fed into the front of the preamplifier. The pre-amp output consists of a series of jagged pulses which travel to the digitizer where they are shaped and digitized and the position of the pulse is calculated digitally (see figure 2.12). The digitizing electronics can operate at speeds as high as 1Mhz for an 8 or 10 bit, x or y coordinate (256 or 1024 pixels). An analog signal is split off and sent to an x-y oscilloscope to show a real time image of the spatial distribution of pulses. The digital coordinates are sent to a histogramming memory where they toggle a switch at the appropriate memory location.

The histogramming memory is controlled by a scaler-timer and can count for a specific time or for a total number of counts. Upon completion of the image, it is downloaded to an LSI-11/23 computer for analysis while the next image is being collected. The software allows image enhancement and massage using the same video processor boards as the video LEED. The I-V collection software is similar to the video LEED software described earlier, but it is set so that the entire process can be fully automated. The first set of I–V curves taken with the DLEED apparatus are shown in figure 2.13. The data set took about 15 minutes to collect at 15 seconds per voltage.

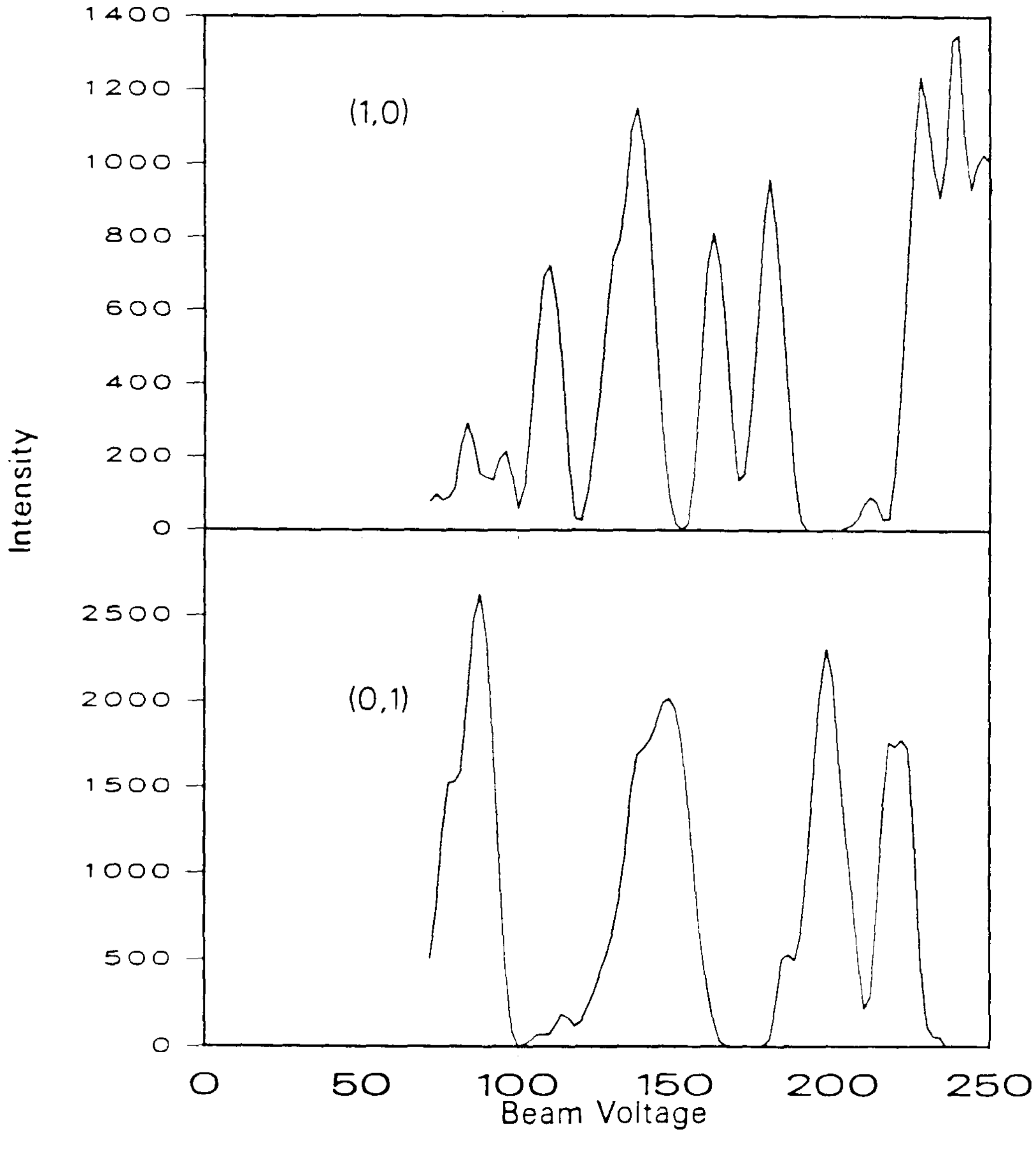

Figure 2.13: First set of I-V curves using the digital LEED system. They are similar to those obtained by Ogletree *et al.* [22] with video LEED.

Chapter 3

Low Temperature LEED: NO on Rh(111)

3.1 Introduction

Many of the efforts in surface science are directed towards an understanding of catalytic behavior at surfaces. The adspecies of interest under real catalytic conditions (atmospheric pressure or higher) are very difficult to form in UHV. For many years investigators have tried to use UHV surface science to understand real catalysis, with limited success. Intermediates in catalytic reactions can be weakly adsorbed, and the surface coverage can be quite high which makes the lateral interactions between adsorbates very important. One way to stabilize either the high coverage structures or the weakly adsorbed molecules is to reduce the temperature of the substrate, thereby, "trapping" the adsorbates on the surface. In this study a closed cycle helium refrigerator was used to cool the sample down to ~40K for adsorption. The low temperature LEED apparatus was used to perform the first surface structural analysis of NO on a metal single crystal surface.

At 40K it was possible to stabilize a high coverage of NO on the surface with only a small exposure. At 250K a dose of 75L was necessary to reach sufficiently high coverage for the (2 × 2) structure to form, but at 40K, the same coverage could be easily obtained after only 2.2L dose (1 Langmuir = 1x10^{-6} torr-seconds). The adsorbate mobility is very low at 40K, so the overlayer had to be annealed to 220K to allow the ordered structure to form. In addition two sites are populated. In this high coverage structure there are three NO molecules per unit cell, one of which is located on a bridge site while the other two are in near top sites. The lateral interactions are strong enough so that the NO molecules are pushed slightly off the pure top site.

In this chapter the structural search for the Rh(111) + (2 × 2) 3NO will be discussed. Section 3.2 contains a survey of the literature for the adsorption of NO on various metal surfaces. The experimental section follows with a brief description of the low temperature LEED apparatus. In section 3.4, the use of High Resolution Electron Energy Loss Spectroscopy (HREELS) as a powerful auxiliary technique will be illustrated as well as the use of cluster compound analogues to assign HREEL spectra. A discussion of the structural analysis by dynamical LEED calculations is included in section 3.5. A discussion of the important aspects of the structure including a comparison to the similar structure Rh(111) + (2 × 2) 3CO obtained by Van Hove *et al.* [23], is presented in section 3.6.

3.2 Background

Nitric oxide adsorption on transition metal surfaces has been extensively studied. Nitric oxide is an appealing candidate for study because it is structurally similar to carbon monoxide, a molecule which has received a great deal of attention and whose adsorption behavior is fairly well known. The molecular orbitals for NO are the same as CO, with only slight changes in the energy levels. Since NO has one extra electron it has some intriguing chemical and physical differences as well. The extra electron goes into a π^* antibonding orbital, thereby reducing the NO bond order to 2.5 (the CO bond order is 3). From analogy to inorganic chemistry we might expect this extra antibonding electron to make the N–O bond easier to break, to make the NO slightly more reactive, and to promote the formation of a bent M–NO bond of sp^2 character.[24]

The reduction of NO to N_2 by a trimetallic catalyst (catalytic converter), in an automobile exhaust system is a poorly understood reaction of great importance.[25] Catalytic converters are composed of a mixture of Pt, Rh, and Pd. The primary role of Rh in a catalytic converter is to catalyze the reduction of NO. Rh is one of the only metals that can do so in the constantly changing environment of an automotive exhaust system.[26] The study of nitric oxide adsorption on metal surfaces is important because of its catalytic behavior and because of its similarity to CO.

A survey of the literature will be presented, with an emphasis on hexagonally symmetric surfaces. A summary of the HREELS results and the proposed adsorption site for each surface are collected in Table 3.1. Castner *et al.* [27] did some of the preliminary investigations of NO on the Rh(111) surface, and observed two ordered LEED patterns, a $c(4 \times 2)$ pattern at low coverage and a (2×2) pattern at saturation coverage.

Root *et al.* [35] studied the adsorption of NO and O on the Rh(111) surface using a combination of Thermal Desorption Spectroscopy (TDS) and X-ray Photoelectron Spectroscopy (XPS). They found that NO adsorbs molecularly at 120K at all coverages. At coverages less than 0.3 monolayer, NO dissociates completely upon heating. The N and O thus formed desorb at 710K (N_2) and 1310K (O_2), respectively. A first order molecular NO desorption peak appears at 455K as the coverage is increased. Root *et al.* determined the saturation coverage of NO on

Substrate	HREELS	Proposed Site	Reference
Rh(111)	1840cm^{-1}	top	this work
	1480–1630	bridge	[28]
	1435	hollow	[29]
Pt(111)	1710	top	[30,31]
	1470	bridge	"
Pt(100) (1x1)	1615	bent	[32]
Pt(100) (5x20)	1805	top	"
	1690	bent	"
Pd(111)	1720–1850	top	[33]
	1510–1660	bridge	"
Ru(001)	1810	top	[31,34]
	1411–1508	bridge	[34]

Table 3.1: HREELS frequency and proposed adsorption sites for NO on various metal surfaces.

Rh(111) to be about 0.68monolayer at 120K. At saturation, 55% of the NO decomposes and desorbs as N_2 and O_2. By preadsorbing oxygen they were able to inhibit the NO decomposition.

De Louise *et al.* [36] used XPS, Secondary Ion Mass Spectrometry (SIMS), and TDS to study NO adsorption on the Rh(111) and Rh(331) surfaces. At room temperature both surfaces exhibited dissociative chemisorption at low coverages. As the coverage was increased a N(1s) peak evolved at 400.1eV indicative of molecular chemisorption. At saturation coverage only 3% of the NO was decomposed at room temperature on the Rh(111) surface, while 10 times that amount was decomposed on the Rh(331) surface. Presumably the huge increase in decomposition can be attributed to a much higher step density on the (331) surface. At high coverage De Louise *et al.* observed an asymmetry in the N(1s) XPS peak at 400.1eV from a smaller peak at 401.4eV. The 401.4eV peak, which accounts for 37% of the total molecular NO at saturation coverage, was assigned to a linear $(M\text{–}NO)^+$ species since the higher binding energy suggests transfer of the antibonding electron to the metal. The other peak at 400.1eV was assigned to the bent $(M\text{–}NO)^-$ state and was presumed to couple more strongly to the metal electrons, thus weakening the N–O bond, making it easier to dissociate.

More recently Root *et al.* used HREELS as a probe of the structure and thermal decomposition of NO on Rh(111).[28] Huge shifts in the N–O vibrational frequency with increasing exposure were found. At low coverages the N–O stretching frequency starts at 1480cm^{-1} and increases to 1630cm^{-1} by saturation. Despite the large frequency shift the mode at 1480–1630cm^{-1} was assigned to the N–O stretch of a bridge bonded species at all coverages. The shift of 150cm^{-1} was attributed to dipole–dipole coupling between the NO molecules, and to a coverage dependence of the backbonding from the metal orbitals to the $2\pi^*$ NO orbitals. The decomposition temperature of NO on Rh(111) was a strong function of the coverage. At low coverages the HREELS signature for intact NO would completely disappear at or near room temperature, while at high coverages the NO stayed intact up to just before desorption at 455K. In the presence of O adatoms the NO stretching frequency is observed at 1840cm^{-1} and is assigned to NO in a top site near one of the oxygen adatoms. Oxygen inhibits the decomposition of NO, while CO did not appear to affect the NO decomposition. No LEED pattern for NO was observed under the conditions of these experiments.

On the Pt(111) surface, NO adsorbs in two distinct sites, based on vibrational analyses and it forms a (2×2) structure at saturation coverage. Gland *et al.* [37], using HREELS, studied the adsorption of NO on Pt(111) at 100K. At low coverage a mode grows in at 1470cm^{-1} , which was assigned to ν_{NO} of bridge site NO. As the coverage was increased another peak was observed at 1710cm^{-1} , assigned to top site NO. Both states appeared to coexist at saturation. However, Hayden used IRAS on the same system and observed the coexistance of the two states in the very narrow coverage range of $0.12 < \theta < 0.16$ monolayer. At higher coverages the bridge site peak, at 1476–1498cm^{-1} , completely converted to the top site at 1700–1725cm^{-1} .[31]

The adsorption of NO on Pd(111) is very similar to Rh(111) and Pt(111). Some early work by Conrad *et al.* [38] with LEED, TDS, and UPS established that NO adsorbs molecularly at all coverages. At room temperature the overlayer was disordered, but if the adsorption was carried out at 200K, first a $c(4 \times 2)$ and then a poorly ordered (2×2) pattern were observed. The (2×2) pattern became sharp and well ordered if the NO back pressure was maintained at or above 1x10^{-6} torr. Conrad suggested that the relatively high pressure of NO was necessary to stabilize the high coverage structure against the large lateral interactions. More recently Harrison *et al.* have used HREELS to study the NO/Pd(111) system.[33] The HREEL spectra has two distinct N–O stretching modes, one at 1590cm^{-1} , populated at all coverages and another at 1780cm^{-1} which only appears near saturation coverage. The high coverage mode only grows in if the temperature is kept below 250K. They assign the 1590cm^{-1} mode to bridge site NO and the 1780cm^{-1} mode to top site.

On the Ru(0001) and Re(0001) surfaces, NO also populates two distinct sites. On Ru(0001)[34,39], at low coverages (<0.3 monolayer), there is a single HREELS vibrational mode at 1411cm^{-1} which is assigned to NO in a 2- or 3–fold bridge site. As the coverage is increased a new vibrational mode appears at 1830cm^{-1} . The latter mode is assigned to a linear NO species. The two forms have very different dissociation temperatures, 316K for bridged and 500K for linear. Different activation energies for the decomposition and blocking of sites by N and O adatoms have been postulated to account for this behavior. Re(0001) shows evidence of two different adsorption sites by XPS.[40]

In summary, in each and every hexagonal surface studied (Rh(111), Pt(111), Pd(111), Pt(100) (5x20), Ru(001), and Re(001)) NO can bond in more than one configuration as based on HREELS, XPS, and TDS. At low temperatures, *i.e.* ~100K, molecular adsorption predominates followed by some degree of dissociation upon heating. As the coverage is increased the amount of dissociation is reduced. In every case, except Rh(111), the vibrational analysis suggests two adsorption sites ranging from bridge and top on Pt(111), to bent and top on Pt(100) (5x20) to hollow and top on Ru(001). In the case of Rh(111) the HREELS suggests the bridge site for all coverages with the top site becoming populated only in the presence of coadsorbed O(ad). However, XPS shows a definite asymmetry in the N(1s) region which could be interpreted as the presence of two sites (top and bent).

There have been no LEED surface structural analyses of molecular NO on any metal surface. Consequently there is still controversy about which sites are populated on each of the different surfaces. The remainder of this chapter is devoted to the first surface structure of molecular NO by LEED: NO on Rh(111) adsorbed at 40K.

3.3 Experimental

The two Rh(111) single crystals used in this study were prepared by conventional techniques.[41] Two different chambers were used for each aspect of the study. The LEED I–V curves for dynamical LEED calculations were obtained on an ion–pumped stainless steel vacuum chamber with a Varian flip manipulator modified to give precision control of the angles of incidence. The LEED chamber was equipped with a closed cycle He refrigerator[42] connected to the crystal via a copper braid. The copper braid permitted X, Y, Z, motion, approximately 270° of polar rotation, and limited azimuthal rotation. A temperature of 40K was achieved after one hour.

Thermal losses were reduced by using electron bombardment from a hot tungsten ribbon to heat the crystal. The crystal was held at ground and the hot tungsten filament biased to about 1keV. The resultant electron flux on the back of the crystal was sufficient to heat the crystal from 40K to 1000K in about 30 seconds. The cooling rate was inversely proportional to the length of the copper braid and a length of about 6 inches proved to be a good compromise between ease of motion and high cooling rates.

A sharp (2×2) pattern was obtained by dosing 2.2L NO (purity 99.999% used as obtained from Matheson) at 40K and briefly annealing to 220K then cooling back to 40K for data collection. The I–V curves were generated using the video LEED technique described in chapter 2. The I–V curves were obtained at normal incidence from 20–200eV and covered a cumulative energy range of 1150eV.

3.4 HREELS

Surface crystallography by LEED relies upon the calculation of the Intensity *vs.* Voltage or I–V curves for a large number of model geometries and subsequent comparison to the experimental curves. A flowchart of a typical LEED analysis is shown in figure 3.1. By systematically changing the model and judging the match between theory and experiment with a reliability factor a best fit can be obtained and the correct surface structure deduced. Each theoretical model tested is calculationally intensive; therefore, any additional information about the surface structure by other techniques, which reduces the number of models tested, can be a great saving in time and effort.

HREELS has proven an invaluable tool for reducing the number of structural models input to the calculations. The vibrational spectra obtained by HREELS can be compared with known cluster compounds from inorganic chemistry to give assignments to the various loss features. The inorganic cluster compounds for NO exhibit great structural diversity. X–ray crystal structures show NO bonding ranging from linear to bent to 2- or 3–fold bridge sites, while the IR vibrational frequencies for ν_{N-O} range from 1300-1900cm^{-1}.[43,44,45,46,47,48] Figure 3.2 summarizes the frequency ranges for a large number of NO cluster compounds along with their sites. The N–O vibrational frequencies correlate quite well with the type of bonding site. On the same figure is shown the HREELS and IRAS vibrational modes for NO adsorbed on various surfaces. From these kinds of comparisons we can obtain a preliminary model for the adsorption of NO, but not its complete structure.

The HREEL spectra we obtained for saturation coverage of NO shows clear evidence of two different adsorption sites.[49] At low coverages there is no ordered pattern and the HREEL spectrum (figure 3.3, bottom panel) has only one peak in the N–O stretching region. The peak at 1635cm^{-1} is consistent with the highest coverage studied by Root *et al.* [28] Comparison with the cluster compound vibrational frequencies in figure 3.2 would suggest either bridge or terminal bent NO. We concur with the bridge site assignment of Root *et al.* due to the lack of any bending modes which should be observed if a bent M–NO species were present.

After a saturation exposure of NO a sharp (2 × 2) LEED pattern appears, and there are marked changes in the HREEL spectra (see figure 3.3 top). There are two distinct peaks in the N–O stretching region, one at 1515cm^{-1} and one at 1840cm^{-1} . There seems little doubt that the smaller of the two peaks at

Obtain desired LEED pattern

↓

Collect data in the form of Intensity vs Voltag curves

↓

Calculate theoretical curves from model geometries

↓

Compare with experimental curves via R-factors

↓

Correct Structure

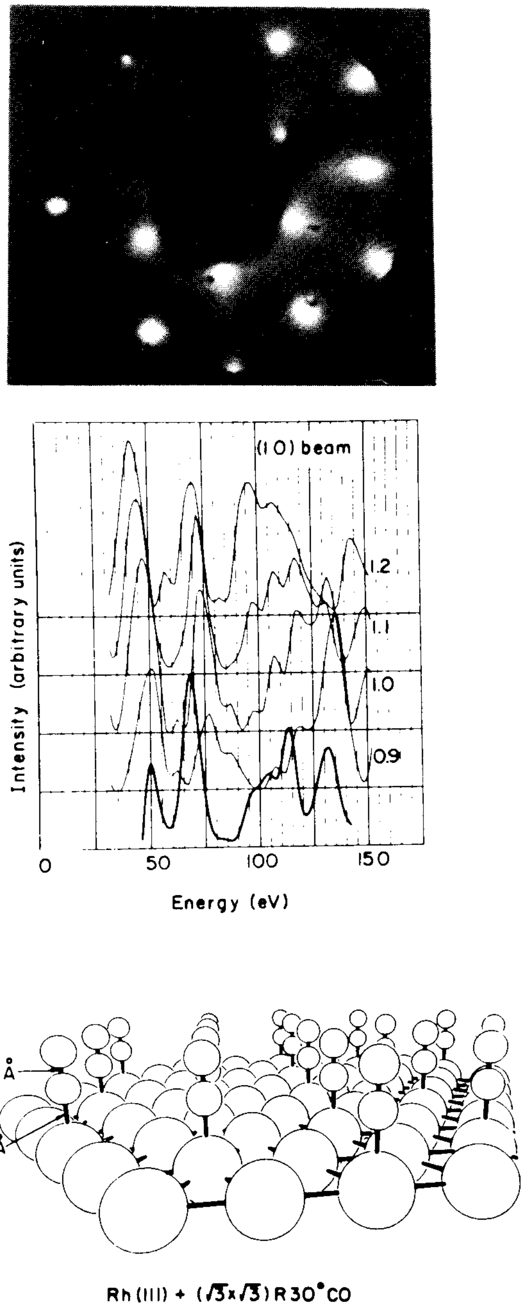

Figure 3.1: Flowchart for a typical surface structure by dynamical LEED calculations.

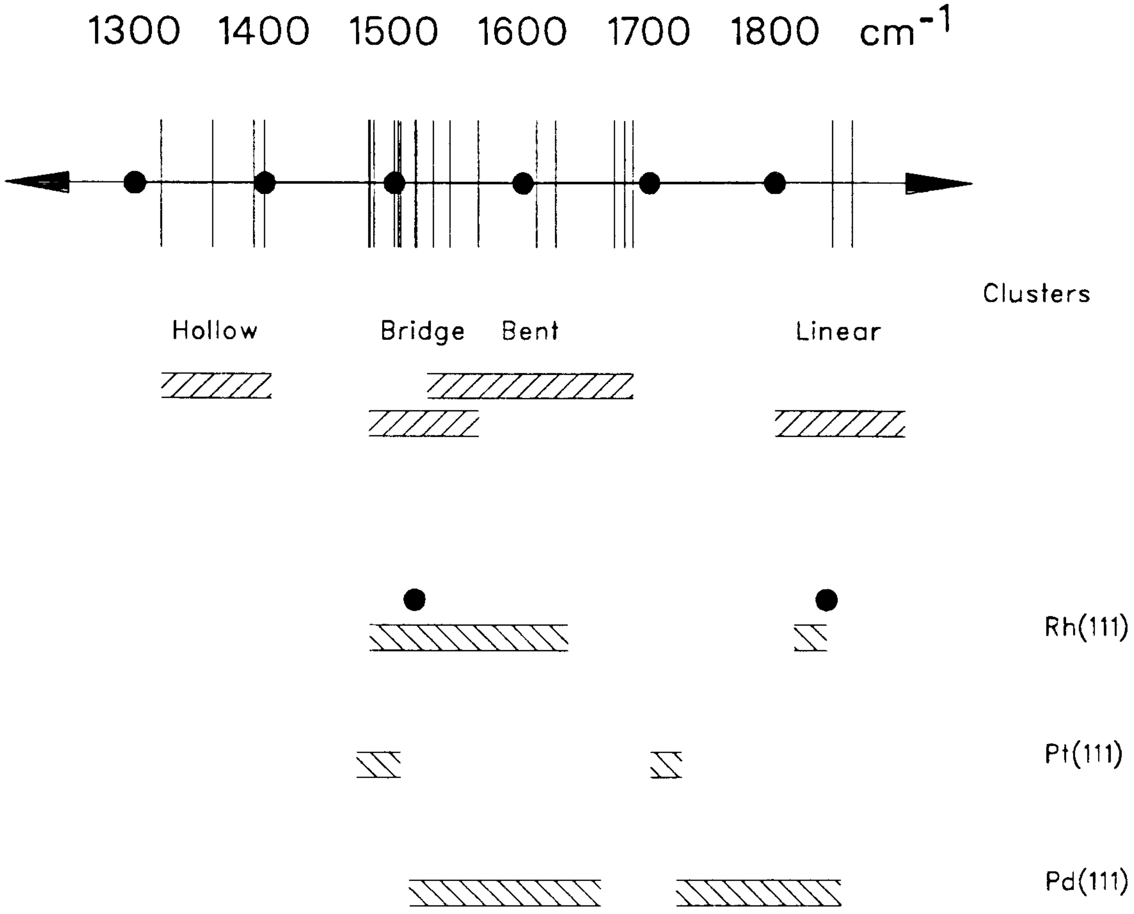

Figure 3.2: Summary of NO stretching frequencies for cluster compounds and surface science studies.

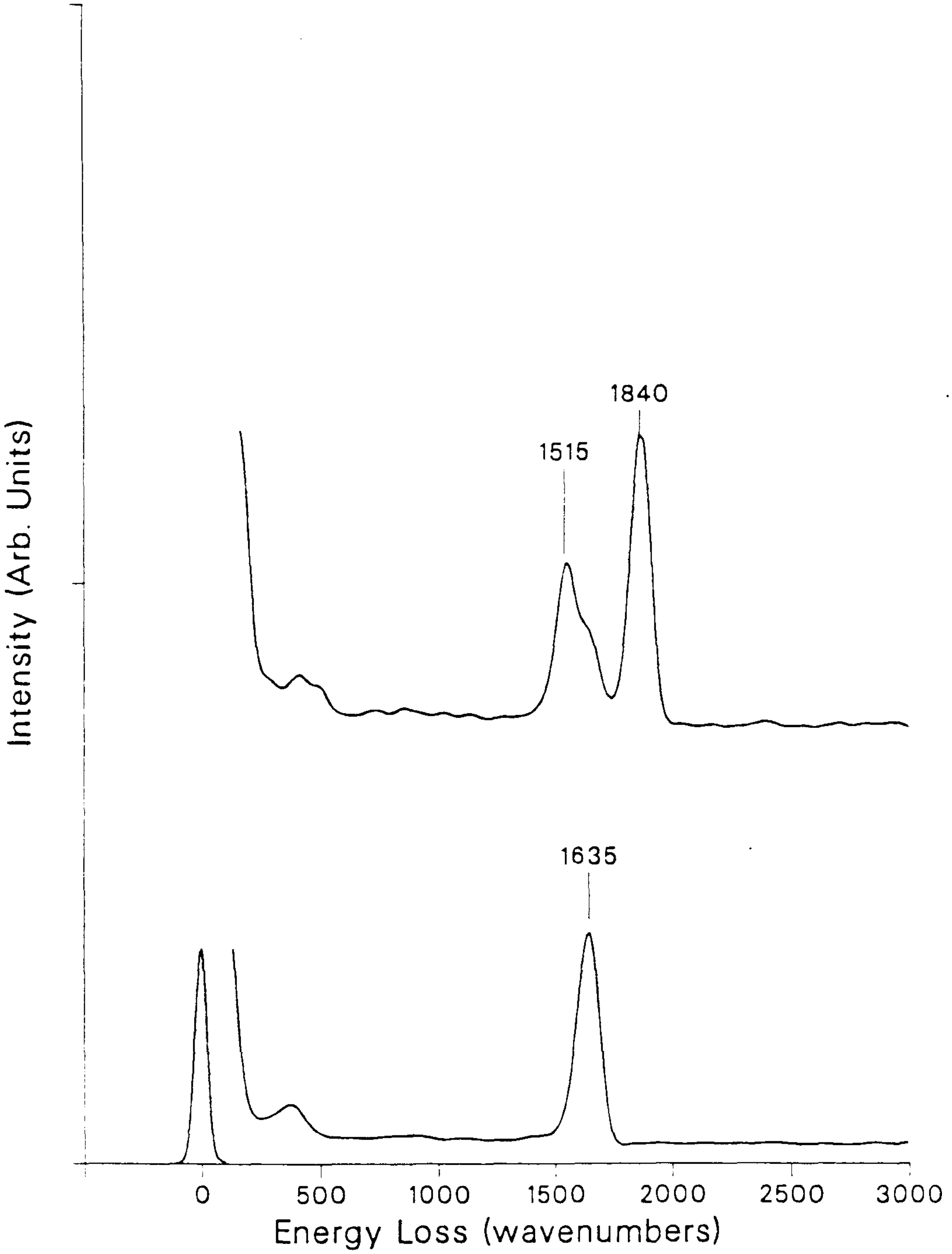

Figure 3.3: HREEL spectra for low (bottom) and saturation (top) coverage for NO on Rh(111) at 170K.[49]

1515cm^{-1} corresponds to bridge site adsorption. The assignment of the 1840cm^{-1} peak is also straightforward. NO in the gas phase has a mode at 1876cm^{-1} so the species responsible for the 1840cm^{-1} mode cannot be perturbed too much upon adsorption. The only nitrosyl complexes with frequencies in this range are linear NO species bound to a single metal atom[45]; therefore, the 1840cm^{-1} mode is assigned to NO bonded in a top site. The HREELS evidence indicates a double adsorption site model and the relative peak heights for NO suggest more top site species than bridge site.

3.5 Structural Search

The search for the correct NO structure on Rh(111) closely paralleled the search for the Rh(111) + (2 × 2) 3CO of Van Hove *et al.* [23] A brief description of the steps in the calculation will be included here. For a more complete discussion of the approximations used see Van Hove *et al.* [50,51] Even at relatively high coverages there is very little multiple scattering between adsorbates so while the scattering within each molecule was included exactly, that between molecules was ignored. This is the basis for the approximation called kinematic sublayer addition (KSLA), which is used to determine the scattered wave amplitudes for the overlayer. The substrate and adsorbate layers were stacked using renormalized forward scattering (RFS) to efficiently model the scattering between each layer. The whole calculation was done within the beam set neglect (BSN) formalism developed by Van Hove *et al.* [52] Table 3.2 summarizes the structural search. The Rh(111) surface was not allowed to relax from the bulk termination because the clean surface was found to be bulk-like to within the LEED accuracy.

Each of the three single adsorption sites, top, bridge, and hollow were initially

Model	$d_{\perp Rh-N}$	$d_{\perp N-N}$	$d_{\parallel N-N}$	$d_{\perp N-O}$
1–bridge/2–top	1.25(0.1)1.65	0.1(0.1)0.8	2.2(0.1)3.0	1.05(0.1)1.35
1–top/2–bridge	1.5(0.1)1.9	0.2(0.1)0.6	2.6(0.1)3.4	1.05(0.1)1.35
1–top	1.5(0.1)1.9	-	-	0.95(0.1)1.35
1–bridge	1.25(0.1)1.65	-	-	0.95(0.1)1.35
1–hollow(both)	1.25(0.1)1.65	-	-	0.95(0.1)1.35

Table 3.2: Summary of parameter variations for structure search for NO (2 × 2) on Rh(111). (Initial value (step) Final value)

Model	$d_{\perp Rh-N}$	$d_{\perp N-N}$	$d_{\parallel N-N}$	$d_{\perp N-O}$	R–factor
1–bridge/2–top	1.55	0.5	2.6	1.15	0.279
1–top/2–bridge	1.70	0.2	2.8	1.15	0.298
1–top	1.70	-	-	1.15	0.358
1–bridge	1.55	-	-	1.05	0.359
1–hollow(both)	1.25	-	-	1.15	0.362

Table 3.3: Best values for the structural parameters for NO on Rh(111).

examined. For the pure single adsorption sites there were only two structural parameters to vary, the Rh–N and the N–O layer spacings. The range for these parameters was chosen to bracket typical values for Rh–N and N–O bonds. Table 3.3 gives the “best” values for each trial structure along with their minimum R–factor. The structures corresponding to the local minima are shown in figure 3.4. All three of the single pure adsorption sites yield poor agreement and relatively large R–factors (0.358, 0.359 and 0.362 for top, bridge, and hollow, respectively). Both the fcc and hcp hollow sites were attempted with equally poor results.

The HREEL spectra for the (2 × 2) NO overlayer suggests two possible configurations for the NO, top and bridge or bent. Van Hove *et al.* [23] have carried out a LEED analysis of the Rh(111) + (2 × 2) 3CO. The (2 × 2) pattern was only observed at relatively high pressures (10^{-5} torr), but a full set of I–V curves were taken and compared to theory. The two sets of I–V curves are shown in

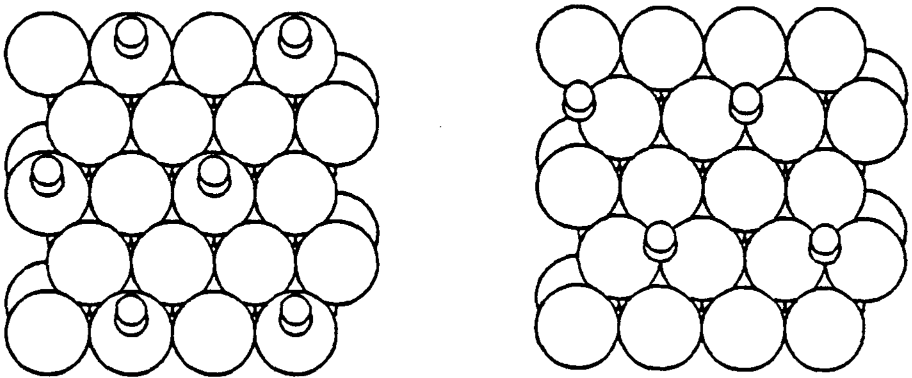

Top Site Bridge Site

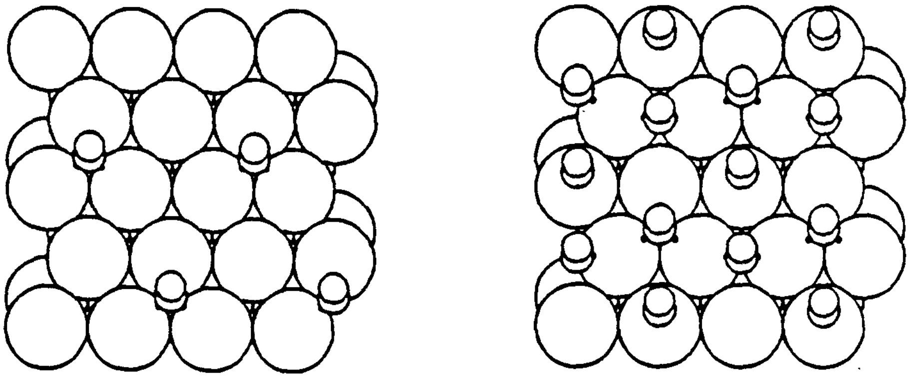

Hollow Site 2 Bridge / 1 Top

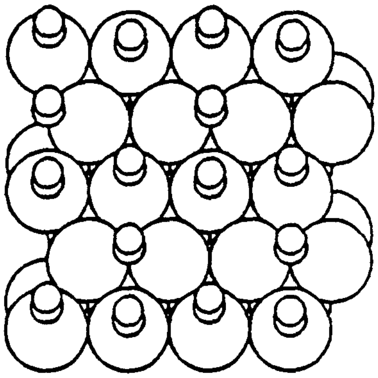

2 Top / 1 Bridge

Figure 3.4: Trial structures for the structural search of NO on Rh(111).

figure 3.5 and they are qualitatively similar. The solved Rh(111) + (2 × 2) 3CO consists of two near–top sites and a bridge site within each unit cell. Because of the similarities in the I–V curves for the two systems, and based upon the HREEL assignments, the initial structural model contains two top sites and one bridge site just as in the CO structure (see figure 3.6).

The symmetry of the unit cell is consistent with one bridge and two top or two bridge and one top site, each was examined. In the two double adsorption site models there are two perpendicular mirror planes which reduce the number of additional structural parameters necessary to completely determine the structure. One of the mirror planes runs parallel to the $(1,\bar{1},0)$ direction connecting the bridge site NO's and making the two top site NO's equivalent. This first mirror plane only exists for the top layer, but we will assume it is a true mirror plane for the purpose of the calculations. The second mirror plane is parallel to the $(1,\bar{2},1)$ direction and makes all of the bridge site NO's equivalent (this one is a true mirror plane). If we constrain the two different N–O bond lengths to have the same value we reduce the number of parameters to four. The N–O bond length is not a severe constraint since the difference between a single and a double bond length is within typical LEED accuracy. The four parameters are $d_{\perp\ Rh-N}$, $d_{\perp\ N-O}$, $d_{\perp\ N-N}$, and $d_{\parallel\ N-N}$. (see figure 3.7).

The one bridge/two top site model yields the lowest R-factor minimum of 0.279 (as opposed to 0.298 for the two bridge/one top model). Assuming the functional form of the R–factor *vs.* any structural parameter to be parabolic it is possible to extrapolate between parameter grid points to give the best structure shown in figure 3.7 with a 5–R factor average of 0.2664. There are a total of three NO's per unit cell in the solved structure. One NO is located on a pure bridge site. The other two molecules bind in top sites, but the coverage is high enough that lateral

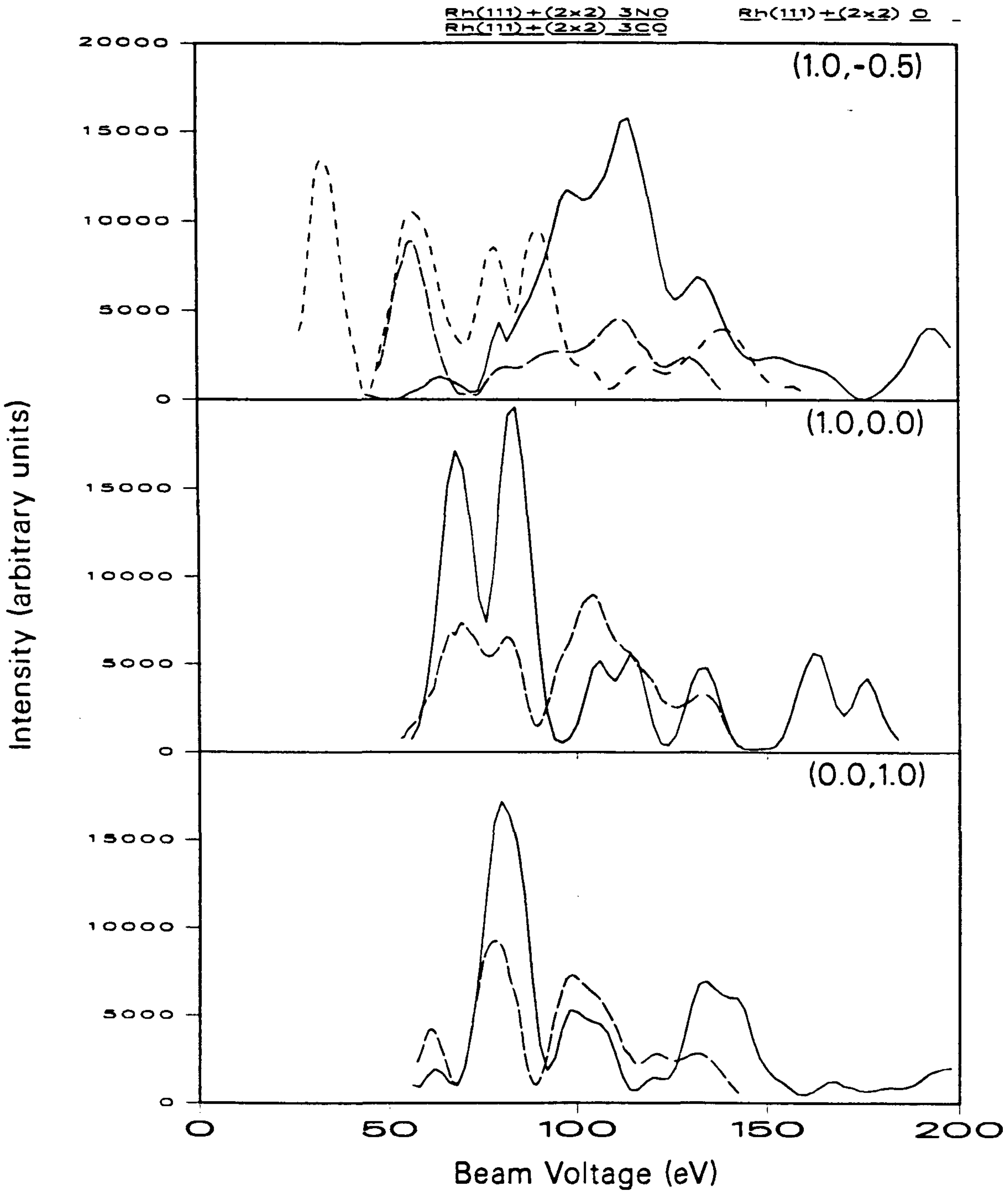

Figure 3.5: Comparison of I-V curves for Rh(111) + (2 × 2) 3NO and Rh(111) + (2 × 2) 3CO and Rh(111) + (2 × 2) O.[51]

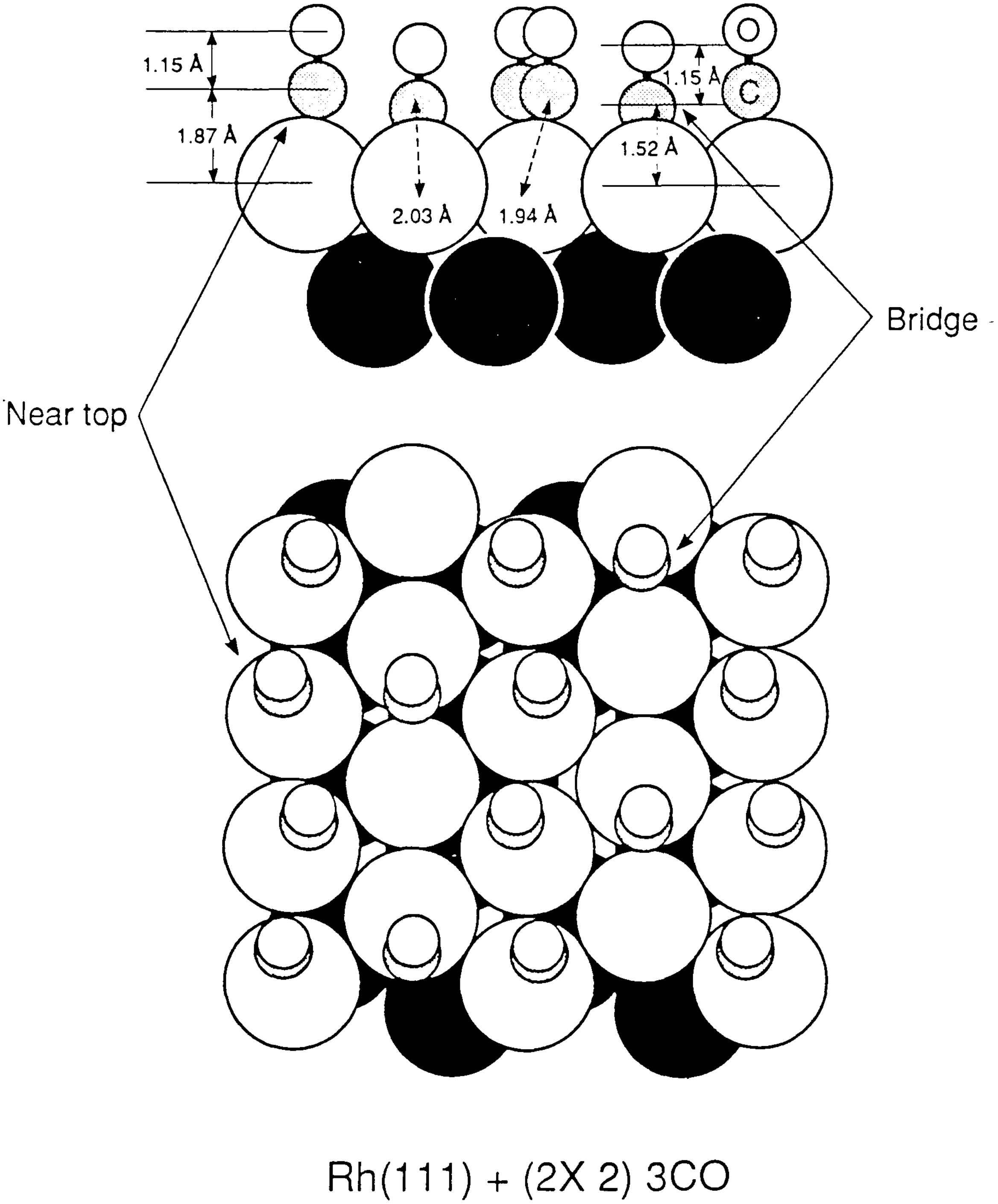

Figure 3.6: Final structure for the Rh(111) + (2 × 2) 3CO pattern.

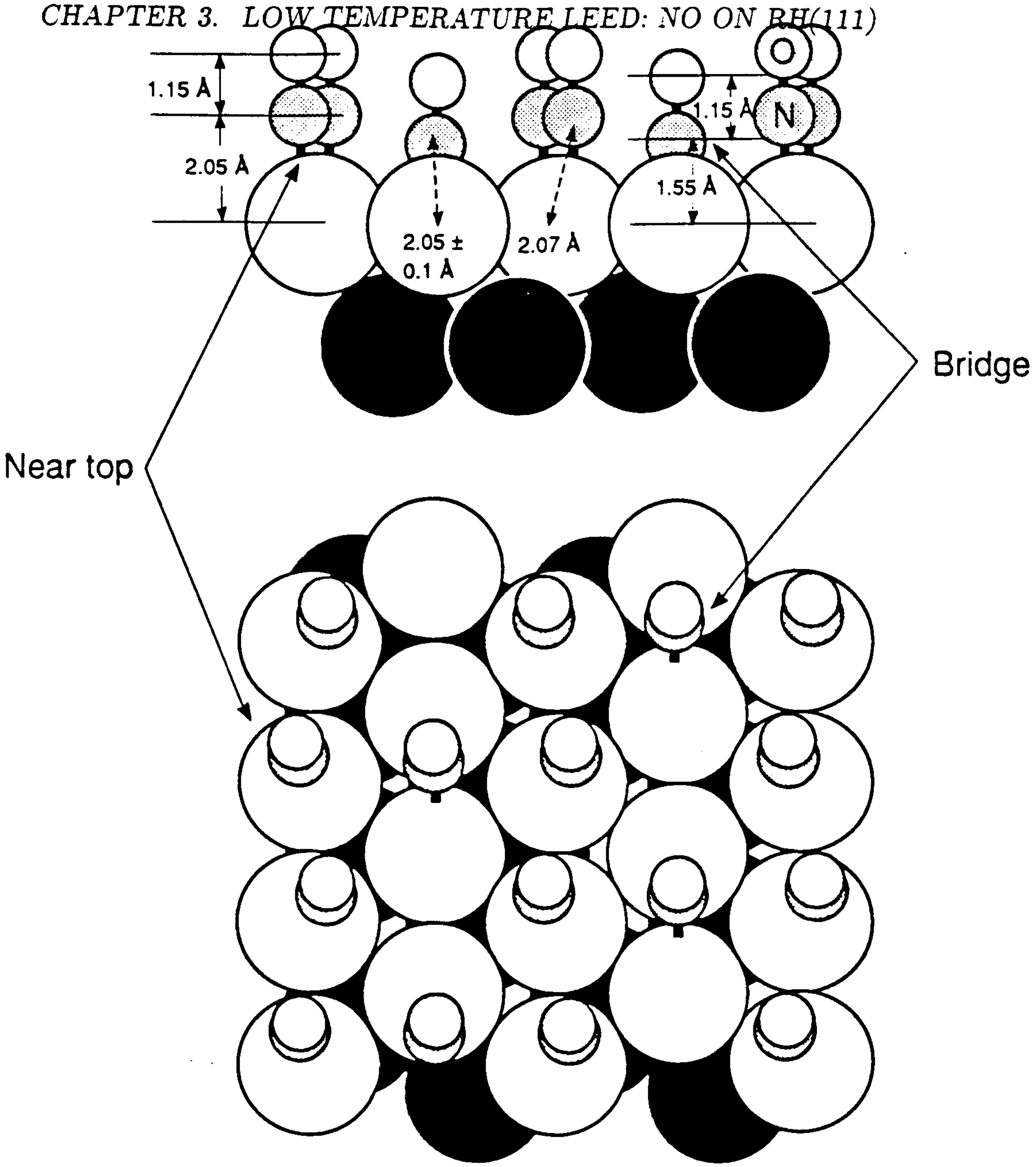

Rh(111) + (2 X 2) 3NO

XBL 888-8950

Figure 3.7: Final structure for the Rh(111) + (2 × 2) 3NO pattern.

repulsions have a noticeable effect. The top site NO's are pushed away from the pure site by 0.22Å. The NO bond lengths are all 1.15Å which is equal to the gas phase value.

3.6 Discussion

It appears that our new surface structural study conflicts with some of the earlier HREELS results. Root *et al.* [28] suggest that NO molecules occupy only bridge sites at all coverages up to full saturation. At their highest coverage (0.68 monolayer) only one N–O vibrational mode at 1630cm^{-1} which is consistent with bridge or bent NO is observed. We see similar results until we go to very large exposures or to very low temperatures. In our HREEL studies we see peaks corresponding to only bridge site NO up to about 75L exposures at 220K. Then a new mode grows in at 1840cm^{-1} . The frequency for this mode places it in the range for top site adsorption.

Root *et al.* see a higher frequency mode only when NO is coadsorbed with oxygen.[53] The only possible source of oxygen in our studies is from partial decomposition of NO, but at saturation coverage only a small percentage of NO decomposes on the Rh(111) surface (3% by XPS[36]). The molecules stay intact until desorption starts at 455K.[28] In order to produce the (2 × 2) pattern for LEED analysis the crystal was cooled to 40K for adsorption, then annealed to 220K to allow the NO to order. It is unlikely that any appreciable decomposition of the NO can occur under these mild conditions.

One would also expect to see a Rh–O stretch at 530cm^{-1} if there was significant decomposition of NO. The HREEL spectrum we observe for the saturated (2 × 2) overlayer is shown in the top panel of figure 3.3. There is no evidence for the presence of oxygen adatoms on the surface. There are two peaks in the N–O stretching region, one at 1840cm^{-1} from NO in a top site, and one at 1515cm^{-1} from a species adsorbed in a bridge site. There is a small shoulder on the 1515cm^{-1} peak at about 1630cm^{-1} which is probably due to smaller amounts of bridge site NO outside of the ordered areas.

Root *et al.* did not observe any ordered pattern for any coverage of NO on Rh(111). A full overlayer of the Rh(111) + (2 × 2) 3NO requires a coverage of 0.75 monolayer, and it was necessary for us to use large doses or low temperatures to produce the structure. Root *et al.* estimate the saturation coverage of NO with XPS to be only 0.68ML, which may explain why they never observed (2 × 2) ordering. They suggested that the previously observed (2 × 2) pattern[27] was due to oxygen adsorption which does exhibit the same pattern at high coverages. The I–V curves for this oxygen structure[51] did not match with the ones we obtained for the NO (2 × 2) . The O-((2 × 2) I–V curve for the (1/2,0) beam is included in figure 3.5 for comparison.

The (2 × 2) structure used for the LEED analysis was produced by adsorption of 2.2L at 40K followed by a short annealing to 220K. Because of the low adsorption temperature high coverages were relatively easy to attain, despite lateral repulsions between the adsorbates. Conrad[38] observed similar behavior for NO on Pd(111). In this study temperatures below 250K and pressures as high as 1x10^{-6} torr of NO were used to produce a well–ordered (2 × 2) pattern. NO and CO are similar in this respect because, in order to maintain a high enough coverage for the Rh(111) + (2 × 2) 3 CO structural study, Van Hove *et al.* had to have a background pressure of 1x10^{-5} torr of CO.[23] In our study, the high coverages are stabilized by the extremely low temperatures, but in the earlier NO and CO studies relatively high pressures were used. It is evident that the the low temperature apparatus can be used to mimic the effects of high pressure on the surface chemical bond.

What sort of phenomena do we observe after this low temperature or high pressure adsorption? The LEED results show the population of a new type of adsorption site. Not only is there a new site populated but, because of the large amount of lateral repulsion between the NO molecules, the NO molecules are pushed away from the pure top site by 0.22Å. Figure 3.8 shows both the NO and CO (2 × 2) overlayers drawn with their corresponding van der Waals radii. In both cases the molecule bonds in pure bridge sites and in near–top sites. The increase in energy from pushing the NO or CO to a less favorable site is compensated for by a reduction in the overlap of the van der Waals radii thereby reducing the lateral repulsions. As one would expect, the CO is pushed further off the top site because the carbon van der Waals radius is larger than nitrogen. In fact the CO overlayer exhibits an almost hexagonal symmetry as a result of this compression. True hexagonal symmetry would minimize the lateral repulsions within the overlayer, but then the overlayer would be incommensurate with the substrate.

One further structural ramification of the lateral repulsion is the small tilt of the top–site CO's in the (2 × 2) structure. Each top–site CO is tilted by about 5° from the surface normal. In chapter 4 another structure with tilted CO will be presented: Rh(111) + $c(4 \times 2)$ CO + CCH_3. The tilt of the CO for both structures may be a further attempt at reducing the lateral repulsions between molecules in these closely packed monolayers. In both NO structures, the NO is perpendicular to the surface to within the accuracy of LEED, despite the fact that there are many NO cluster compounds exhibiting bent M–NO bonds.

3.7 Conclusions

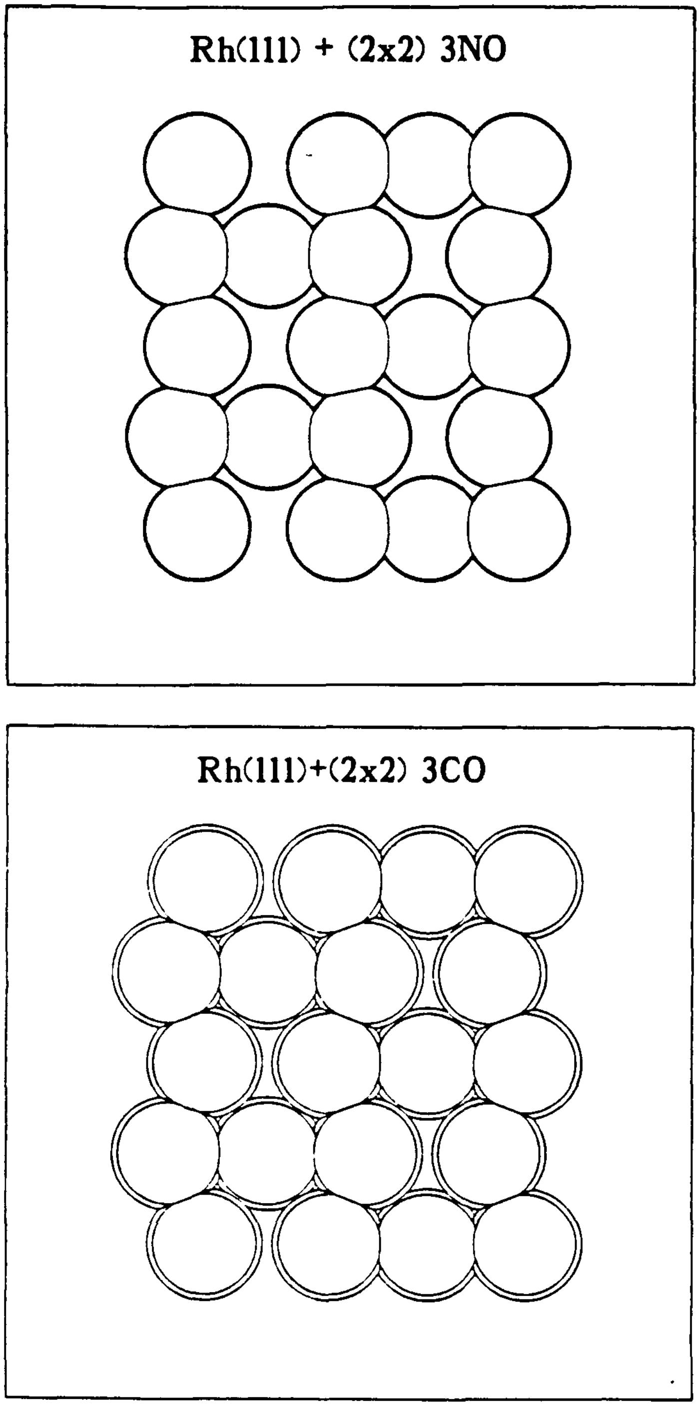

XBL 889-3249

Figure 3.8: Surface structure for the (2 × 2) patterns drawn with van der Waals radii.

The (2 × 2) NO on Rh(111) structure is the first dynamical LEED study for NO on any metal surface. High pressure adsorption was mimicked in this study by using a low temperature LEED apparatus. There are three intact NO molecules in each unit cell, two in near–top sites and one in a bridge site. Lateral repulsions between NO molecules in this high coverage structure are large enough to push the top site NO's to the near–top site positions. In the similar Rh(111) + (2 × 2) 3CO structure, CO molecules behave in the same way, but there are even larger lateral repulsions which push the CO further from the pure top site.

Chapter 4

Coadsorbate Induced Ordering

4.1 Introduction

Adsorbate–adsorbate interactions have an important effect on surface chemistry, but they are poorly understood. The interaction can be mediated either through the substrate, usually called an electronic effect, or directly by steric repulsions. Such lateral interactions can be very important at higher applied pressures (*e.g.* in a catalytic reactor) when the surface species are closely packed together. One way to probe the interactions between adsorbates in an UHV environment is to work at very high coverages as in chapter 3. Another way is to use mixtures of different adsorbates. An understanding of the structural effects that one adsorbate induces on a neighboring adsorbate will help us to understand the lateral interactions between molecules adsorbed on a surface. Coadsorbed systems are typified by relatively high coverages and in some cases unusual bonding configurations. Studying the structure of coadsorbate systems and the details of the order–order transitions provides information relevant to the nature of adsorbate–adsorbate interactions at higher applied pressures.

Low–Energy Electron Diffraction (LEED) has been used for many years to study thousands of ordered surfaces.[54] Their three–dimensional atomic structure can be determined by comparing experimental LEED intensities with theory.[50] Over the years some 200 surface structures have been determined in this way.[55] In most of these cases the ordered surface consisted of a clean or reconstructed metal with a single atomic or simple molecular adsorbate. A new level of complexity has recently been introduced with coadsorbate induced ordering of molecules.[56]

Coadsorbate induced ordering is a cooperative interaction between two different adsorbates which yields a different ordered structure than either adsorbate forms by itself. The phenomenon of coadsorbate induced ordering has been investigated in our laboratory with various combinations of adsorbates.[56,57,58,59,60] If an adsorbate that either orders poorly or not at all by itself can be forced to order by the addition of an appropriate coadsorbate, then we can more easily extract the surface structure by using dynamical LEED calculations.

In our group we utilize a particularly powerful combination of techniques for surface structural analysis: High Resolution Electron Energy Loss Spectroscopy (HREELS) and LEED. HREELS provides information regarding the local geometry of the adsorbates and LEED gives us the structure of the ordered portions of the surface. By comparing the HREEL spectra to the vibrational spectra of cluster compounds, many of the possible proposed structures can be eliminated, thereby making the LEED structural analyses faster and easier. Throughout this chapter you will see the interplay of the two techniques and how they have been used successfully to unravel the complexities of the surface structures presented.

This chapter describes investigations of a number of coadsorbate induced ordered structures. Historically, the first system found to exhibit such ordering was the CO plus benzene system on Rh(111). In 1985 Mate discovered, through a careful HREELS analysis, that certain ordered benzene patterns could not be obtained without the addition of small amounts of CO.[56] Section 4.4 recounts briefly some of the HREELS results and discusses in detail the structural studies for the benzene/CO system.

Once the Pandora's box was opened, a whole series of different coadsorbed structures were found.[57,58,59,60,29] A logical step in the search for more coadsorbed structures was to use NO in the place of CO as an inducement to order. NO is structurally and electronically similar to CO. It has one extra electron from the nitrogen which populates the $2\pi^*$ antibonding orbital – consequently, NO has a bond order of 2.5 instead of 3.0 as in CO. Nitrogen has a smaller van der Waals radius than carbon (1.65, and 1.75Å respectively) which could effect the lateral interactions. As expected, NO also participates in coadsorbate induced ordering. Section 4.5 describes the ordering modification of ethylidyne when coadsorbed with NO and CO.

Many unusual bonding configurations have been observed in coadsorbate induced ordered structures. CO, by itself, on Rh(111) bonds in a top or a bridge site, but when coadsorbed with benzene it occupies the three–fold hollow sites. Benzene exhibits a Kekulé distortion (alternation of short and long bonds) in the coadsorbate induced ordered structures on Rh(111). In addition, the benzene ring is expanded from its gas phase value which may have interesting catalytic implications.

As mentioned above, CO and NO will both induce an ordered structure when coadsorbed with ethylidyne on Rh(111). The CO and NO molecules bond in different three–fold hollow sites upon coadsorption with ethylidyne (hcp and fcc hollows, respectively). Ethylidyne switches sites between hcp and fcc hollows depending on which coadsorbate it is paired with. The lateral interactions are large enough to cause the CO molecules to tilt slightly in the CO plus ethylidyne ordered structure, but the NO is oriented perpendicular to the surface. In each case, the presence of neighboring ethylidynes modifies the surface chemical bonds of CO and NO, because of the lateral interactions.

This chapter is divided into two major sections: the first (Section 4.4) is concerned with the CO/benzene coadsorption system; the second (Section 4.5) contains a discussion of the CO/ethylidyne and NO/ethylidyne systems. Each section is organized in a chronological sequence. The formation of each of the structures and their corresponding LEED patterns are discussed first. Then the HREELS analyses of the ordered structures is presented. An initial structural model is proposed based on the LEED patterns and the HREELS analyses. Starting with the proposed structure multiple scattering calculations were performed to determine the variation of scattered intensity of the ordered diffraction spots with incident electron energy (or voltage). The theoretical Intensity *vs.* Voltage (I–V) curves are then compared to the experimental ones through a so-called reliability factor (R-factor). By graphing a structural parameter *vs.* the reliability factor, the minimum R-factor is determined, and this corresponds to the best structural model. If the R-factor is low enough, that is, if the fit between theory and experiment is good enough, we are confident that the correct structure has been found.

4.2 Background

The bonding modifications caused by the presence of coadsorbates is best illustrated by comparison with the structures of the adsorbates by themselves. This section will discuss what is known about the surface structures of the various molecules, by themselves, on the Rh(111) surface.

Carbon monoxide is the most widely studied molecular adsorbate, and the

Adsorbate(s)	$d_{\perp Rh-CO(NO)}$	$d_{\perp C-O(N-O)}$	site
$(\sqrt{3}\text{x}\sqrt{3})$ R30° -CO	1.95	1.07	top
(2x2)-3CO	1.87	1.15	near top
"	1.52	1.15	bridge
(2x2)-3NO	2.05	1.15	near top
"	1.55	1.15	bridge

Table 4.1: Summary of the surface structures of CO and NO on the Rh(111) surface.

surface crystallography of pure CO on Rh(111) is well characterized. As many as four separate ordered phases are formed.[27,61] Around 125K, a (2×2) pattern is observed at low coverages, which changes to a $(\sqrt{3} \times \sqrt{3})R\,30°$ pattern at a coverage of approximately 1/3 of a monolayer. Further exposure causes the formation of a so-called "split (2×2)" structure, followed finally by a second (2×2) structure at saturation coverage. Both the $(\sqrt{3} \times \sqrt{3})R\,30°$ and the high coverage (2×2) structures have been solved using LEED surface crystallography.[62,63] The solved structures are shown in figure 4.1. All of the structural parameters are collected in Table 4.1.

Even by itself CO exhibits significant lateral interactions. Initially CO bonds only at the top sites, as shown in figure 4.1a. As the coverage increases above 1/3 monolayer the lateral repulsions between CO molecules force the additional CO molecules to occupy new sites. The HREEL spectra exhibit an additional peak which corresponds to bridge site CO. The high coverage (2×2) structure (figure 4.1b) was only stable in a relatively high background pressure of CO ($1\text{x}10^{-5}$ torr). The LEED analysis confirms the presence of both top and bridge sites. The lateral repulsions between CO molecules; however result in a significant dis-

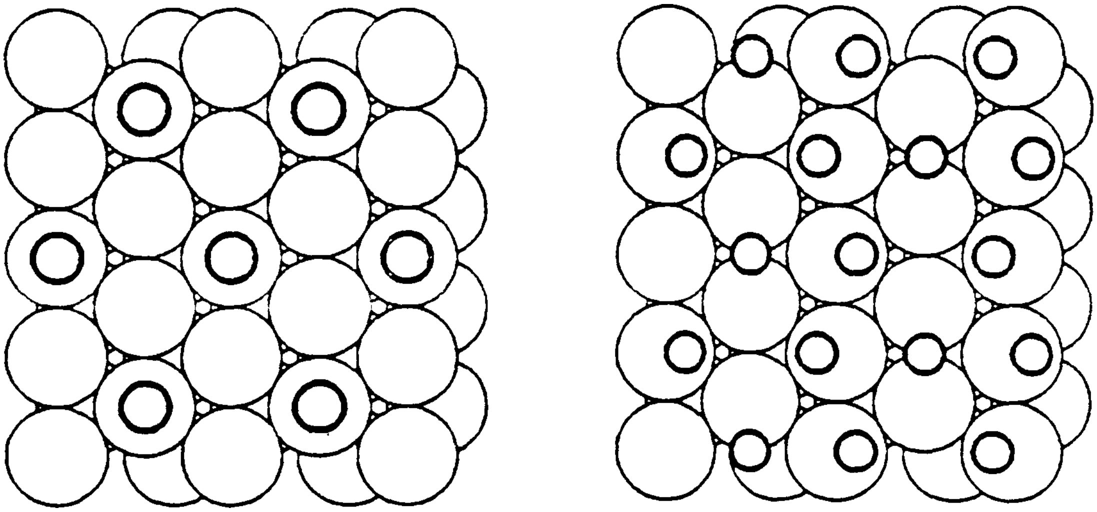

Rh(111) + $(\sqrt{3} \times \sqrt{3})R30°$ CO   Rh(111) + (2 × 2) 3CO

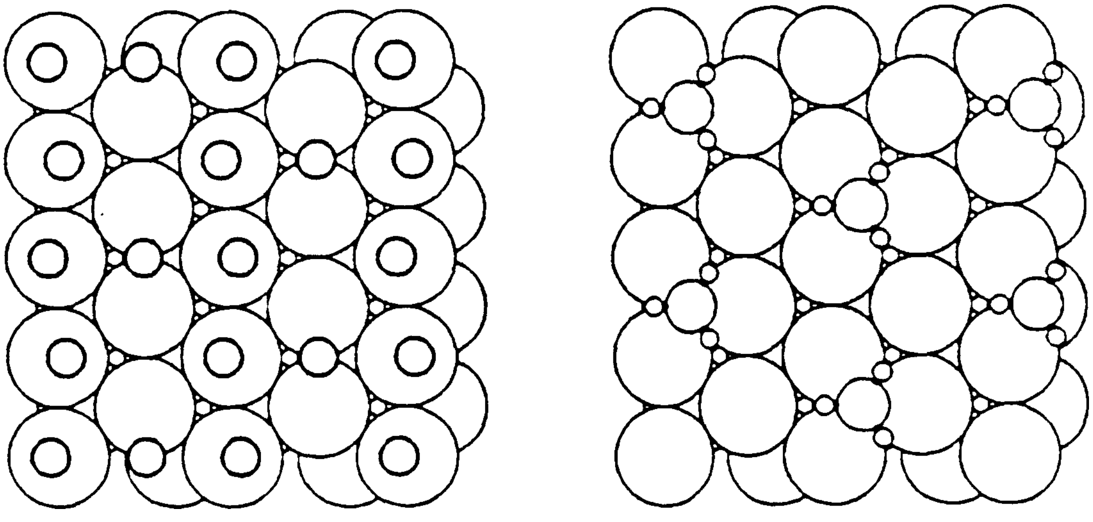

Rh(111) + (2 × 2) 3NO   Rh(111) + (2 × 2) CCH_3

Figure 4.1: Surface structures of CO, NO, and ethylidyne on the Rh(111) surface. a. Rh(111) + $\sqrt{3}$CO. b. Rh(111) + (2 × 2) 3CO. c. Rh(111) + (2 × 2) 3 NO. d. Rh(111) + (2 × 2) CCH_3

placement of the "top site" CO molecules and a distortion the overlayer towards hexagonal symmetry. (For a more detailed discussion of the high coverage structure see chapter 3.)

It has never been possible to determine by LEED the surface structure of benzene by itself on any surface. On Pt(111) and Pd(111) benzene is disordered and on Rh(111) it is so beam sensitive that LEED structural analysis has proven impossible. Work is in progress to use the new low current digital LEED apparatus (chapter 5) to determine the structure of disordered benzene on Pt(111), but until that study is completed the only solved LEED structures for benzene are the coadsorbate induced ordered structures discussed here.[58,59,60]

Despite its catalytic importance, the only LEED structural analysis of molecular NO on *any* surface is the one presented in the previous chapter. The NO orders into a (2 × 2) pattern at either very high exposures or at very low temperatures. The surface structure is shown in figure 4.1c and the bond lengths are collected in table 4.1. At low coverages, NO bonds exclusively in bridge sites[28] and the top sites are only occupied at very high coverages (opposite to the behavior of CO). The (2 × 2) structure of NO does not exhibit as much of a hexagonal distortion as the CO (2 × 2) structure does, presumably because of smaller lateral repulsions in the overlayer.

Ethylene by itself adsorbs as a disordered molecular overlayer at 40K at all coverages. Annealing the ethylene layer to around 70K gives the adspecies sufficient mobility that they can relax into ordered phases, indicating a relatively small barrier for surface diffusion. After an exposure of 1.5L and heating to 70K a sharp (2 × 2) pattern is observed. With increasing exposures (and the same annealing conditions) coexisting $(\sqrt{3} \times \sqrt{3})R30^\circ$ and (2 × 2) patterns are first observed at 2.0L and finally a pure $(\sqrt{3} \times \sqrt{3})R30^\circ$ pattern is observed. TDS and HREELS results suggest an intact C_2H_4 molecule with its C–C axis parallel to the surface and elongated slightly to between a single and double bond length.[64]

As the temperature is increased approximately 25% of the ethylene in the saturated monolayer desorbs molecularly and the rest partially decomposes and reorients to give 0.25 monolayer of a surface ethylidyne.[65,66,67,64] This transformation occurs at around 220K and produces a (2 × 2) pattern (the IV curves change as the surface structure changes, but the surface symmetry does not). Upon further heating to 270K, hydrogen desorbs and the ethylidyne (2 × 2) structure disorders to give diffuse intensity near the (1/3,1/3) positions as shown in the bottom right of figure 4.7. The ethylidyne remains intact until as high as 400K where it presumably decomposes to CCH and CH fragments.[68] The ethylidyne (2 × 2) structure has been solved using dynamical LEED calculations[65] and is shown in figure 4.1d.

4.3 LEED theory

The theoretical methods applied in this work have been described previously.[23,50,51,52,69] Only a summary is given here.

Within the Combined Space Method we have used Renormalized Forward Scattering to stack layers. The substrate layer diffraction was calculated accurately with conventional methods.[50,51] The overlayer diffraction matrices were obtained with full multiple scattering within individual molecules by Matrix Inversion, and with Kinematic Sublayer Addition to combine the different molecules. In addition, Beam Set Neglect was applied. All of these approximations have been shown to yield structural results to rather better than 0.1Å for molecular overlayers.[23,52] As in earlier work, hydrogen was left out of the calculations, since it is too weak a scatterer to interfere with the structure determination or to be detected against other adsorbates.

The non-structural parameters in our LEED calculations were identical to those selected in previous LEED studies of ethylidyne [65] and carbon monoxide [23,62] on Rh(111). For nitric oxide, we generated phase shifts starting from a cluster of eight rhodium atoms in fcc(111) configuration and a top site NO molecule. The Hermann–Skillman wavefunctions were used as input into the CAVLEED phase shift program [70],and phase shifts up to $l_{max}=5$ were used.

As in previous work[62], five R-factors and their average were applied to compare theory and experiment.

4.4 Carbon Monoxide plus Benzene on Rh(111)

4.4.1 LEED patterns

Benzene forms three distinct ordered patterns on the Rh(111) surface, depending only on the amount of CO incorporated in the lattice.[56] A schematic diagram for each of the ordered patterns is shown in figure 4.2. The first ordered pattern observed is for saturation coverage of benzene with no CO. Using matrix notation this pattern is described as a

$$\begin{pmatrix} 3 & 3 \\ \bar{2} & 2 \end{pmatrix}$$

or in the Wood's notation a $(2\sqrt{3} \times 3)rect$. After careful examination of this pattern at normal incidence a systematic absence of certain spots was observed. Such absences are indicative of an additional symmetry element called a glide line symmetry.[51,71] A glide line symmetry puts certain restrictions on the contents of the surface unit cell, in this case there must be an even number of molecules in the cell related by the glide line. An excellent candidate is shown in figure 4.3, but the exact structure is unknown because this structure is very beam sensitive.

Preadsorption of CO followed by saturation exposure of benzene yields a completely different ordered pattern called a $c(2\sqrt{3} \times 4)rect.$ or a

$$\begin{pmatrix} 3 & 1 \\ 1 & 3 \end{pmatrix}$$

structure. This structure will form spontaneously from the $(2\sqrt{3} \times 3)rect.$ structure as a result of CO adsorption from the background gases. As still more CO is added, a mixed LEED pattern is observed followed by a stable (3×3) or

$$\begin{pmatrix} 3 & 0 \\ 0 & 3 \end{pmatrix}$$

pattern. If still more CO is preadsorbed, a disordered LEED pattern is observed upon exposure to benzene. The (3×3) pattern is the most stable of the three patterns and each of the others will ultimately convert to the (3×3) if left in UHV. Once the (3×3) is formed, it is stable for literally weeks in UHV. Ohtani *et al.* have even managed to use Scanning Tunneling Microscopy to image benzene molecules in this structure.[60]

The $c(2\sqrt{3} \times 4)rect.$ structure was studied by Van Hove *et al.* [23,69] and the (3×3) structure is discussed in this chapter. For the $c(2\sqrt{3} \times 4)rect.$ pattern, a complete set of I–V curves with thirteen beams and a cumulative energy range of 1224eV was collected. The structural search for the both the $c(2\sqrt{3} \times 4)rect.$ and the (3×3) structure is similar and is discussed in section 4.4.3. The (3×3) pattern was obtained, at room temperature, by dosing 0.4L CO ($\sim 2/9$ monolayer based on the solved $(\sqrt{3} \times \sqrt{3})R\,30°$ CO pattern at 1/3 monolayer coverage) and then saturating the surface with a 0.7L dose of benzene. The I–V curves were collected with the video LEED technique, described in chapter 2, for energies

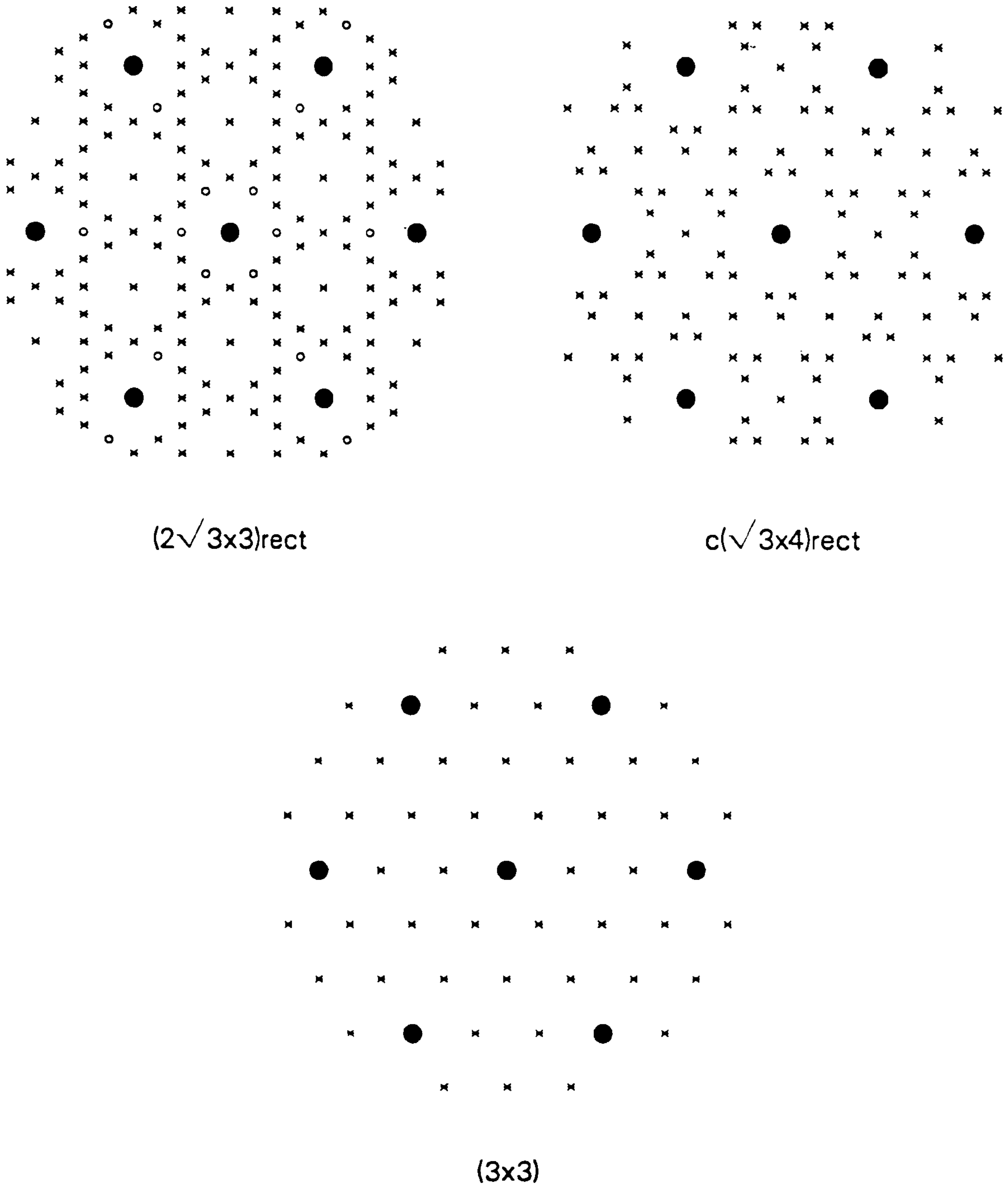

(2$\sqrt{3}$x3)rect

c($\sqrt{3}$x4)rect

(3x3)

Figure 4.2: Schematic diagram of the three ordered LEED patterns for benzene coadsorption on the Rh(111) surface.

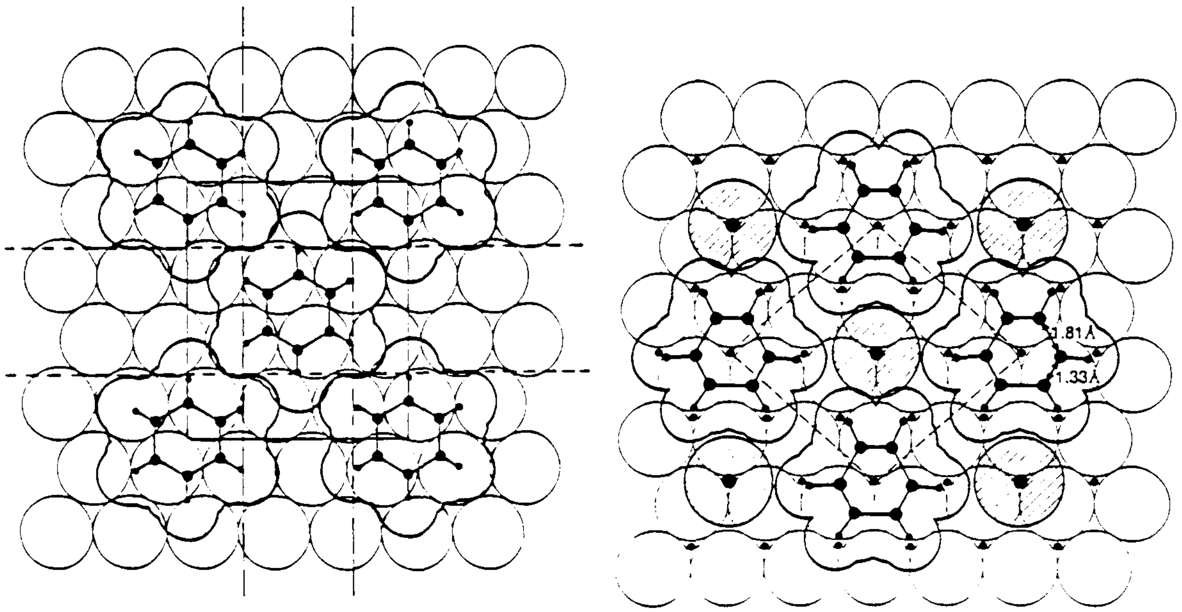

$(2\sqrt{3}\times3)$rect

c$(\sqrt{3}\times4)$rect

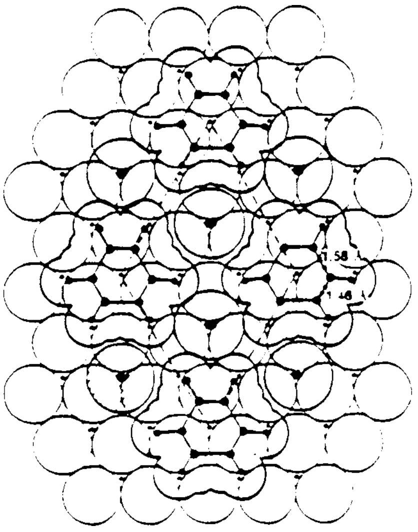

(3×3)

Figure 4.3: Initial guesses for the surface structures for the three ordered structures of benzene on Rh(111).

from 20–200eV for all the beams in figure 4.2. The cumulative energy range for the 14 symmetry inequivalent beams was 1144eV.

4.4.2 HREELS of CO plus Benzene on Rh(111)

A great deal of information can be inferred from the vibrational modes of an adsorbed molecule. HREELS provides a starting place, an initial "guess", for the surface structural analysis. The general methodology involves comparing the IR modes of the clusters and the HREEL spectra of the surface species, to yield a plausible model for the identity of the surface species.

As CO is coadsorbed with benzene, the structural modifications and interactions between the adsorbates can be monitored with HREELS. Figure 4.4[56] shows the HREEL spectra for the three different ordered structures of CO plus benzene on Rh(111). The bottom spectra in figure 4.4 is for the $(2\sqrt{3} \times 3)rect.$ structure of pure benzene on Rh(111). The strongest mode in the spectra (at 805cm^{-1}) shifts by a large amount (to 565cm^{-1}) upon deuteration. Thus, the 805cm^{-1} mode must be a C–H mode as opposed to a C–C or Rh–C mode which would not shift as much after deuteration.[72] Metal–benzene complexes with the benzene π–bonded to the metal atom have a γ_{CH} mode in this region (*e.g.* $(C_6H_6)_2Cr$ has a mode at 795cm^{-1} [73]). The large vibrational loss peak is therefore assigned to the γ_{CH} mode. There are some weak modes at 1115, 1330, and 1430cm^{-1} , which can be assigned by comparison to gas phase benzene to the δ_{CH} (CH bend), the C–C stretch, and the ring deformation modes, respectively. Each of the three weaker modes are in the plane of the molecule, while the strong mode at 805cm^{-1} has its dynamic dipole oriented perpendicular to the plane of the ring. Modes which are strongly peaked in the specular direction arise from dipole scattering. The dipole selection rule[74] states that a mode with its dynamic dipole perpendicular to the surface will be strong; therefore, the benzene must be intact and lying flat on the surface. Any tilt of the molecule would weaken the γ_{CH} out of plane mode and strengthen the other benzene modes.

The benzene vibrational modes are virtually unaffected by the addition of CO. The middle and top spectra in figure 4.4 are from the $c(2\sqrt{3} \times 4)rect.$ structure at $\theta_{CO} = 0.12$ monolayer and the (3×3) structure at $\theta_{CO} = 0.22$ monolayer respectively. The γ_{CH} and the in-plane modes occur at the same frequencies to within the 40cm^{-1} resolution of HREELS; therefore, the benzene configuration must be essentially unchanged by the coadsorption of CO. It should be noted however that HREELS is relatively insensitive to the benzene adsorption site.

The C–O vibrational frequency however, is extremely sensitive to the adsorption site. From the HREEL spectra of the (2×2) 3CO structure on Rh(111), discussed in the previous chapter, we know that CO in a top site has a C–O stretching mode at 2065cm^{-1} and a bridge site mode at 1855cm^{-1} . One would expect CO bonded in a three-fold hollow site to have a stretching frequency below either the top or bridge sites. The $c(2\sqrt{3} \times 4)rect.$ has a C–O mode at 1655cm^{-1} while the (3×3) has one at 1700cm^{-1} . CO cluster compounds with frequencies in this range have the CO bonded to three metal atoms.[75] Therefore, the modes at 1655 and 1700cm^{-1} are assigned to CO in a three-fold hollow site.

Based on the HREELS analyses an approximate surface structure can be deduced. The initial guesses are shown in figure 4.3 in which benzene is drawn with its approximate van der Waals radii. The $(2\sqrt{3} \times 3)rect.$ structure has the benzene located on the bridge sites. Although HREELS is not sensitive to the benzene adsorption site, the presence of glide line symmetry severely limits the choice of structures. In figure 4.3 the vertical dashed lines represent glide planes perpen-

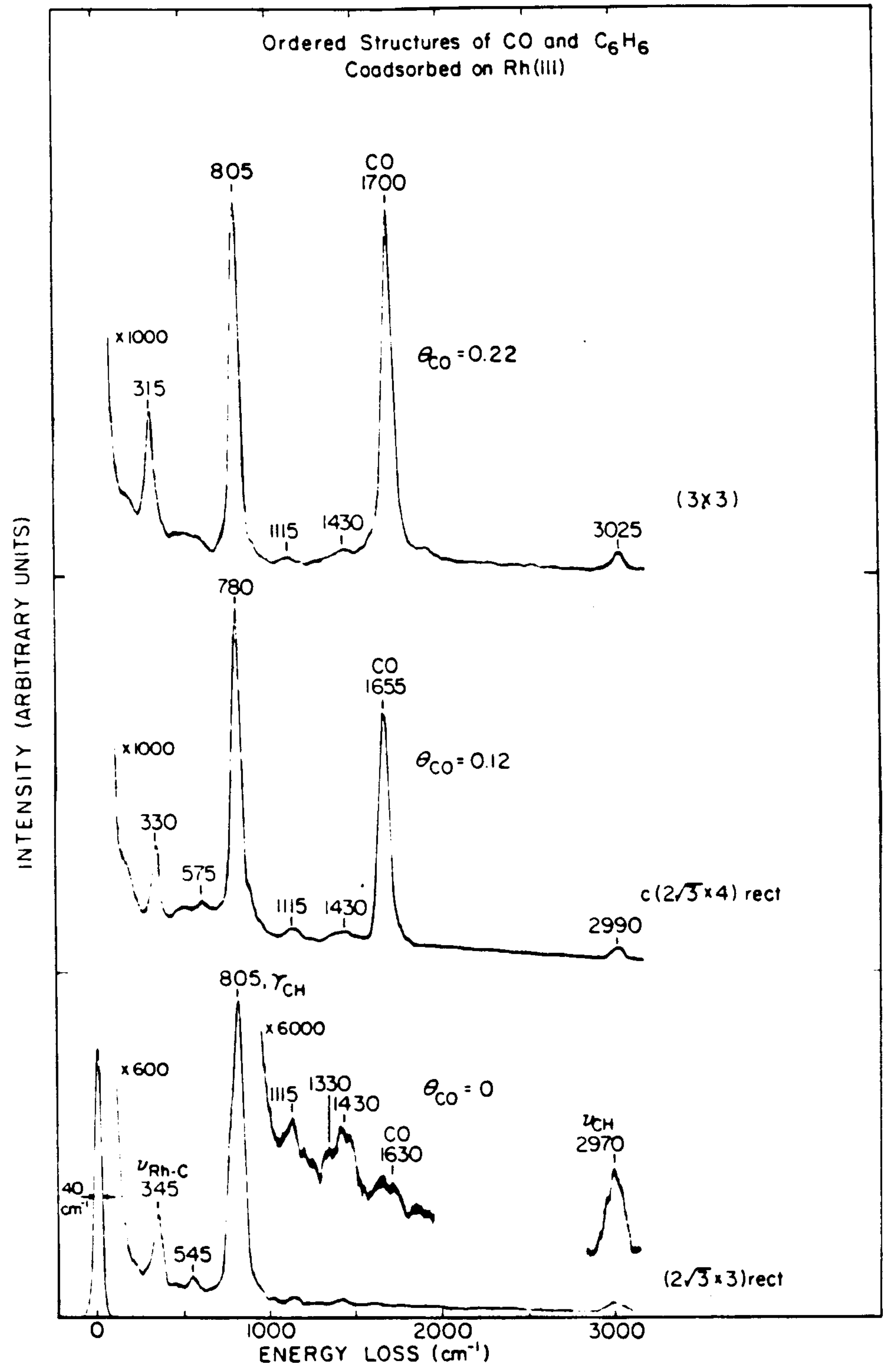

Figure 4.4: HREEL spectra of benzene on Rh(111) with varying amounts of CO.

dicular to the surface. The starting structures for the two coadsorption patterns are also shown in figure 4.3. The holes in the benzene structures are just large enough to contain CO molecules: one CO in each unit cell in the $c(2\sqrt{3} \times 4)rect.$ structure and two CO's per unit cell in the (3×3) structure. In the theoretical calculations both the benzene and CO molecules were initially assigned gas phase bond lengths and angles.

4.4.3 Structural Search and Results for the Rh(111) + (3×3) 2CO + Benzene Structure

The (3×3) unit cell is a large one and the presence of two different molecular adsorbates in each unit cell rapidly escalates the theoretical difficulties. Each plausible structure must be tested; and even with the information available from other techniques, there are still a large number of different models. A full multiple scattering calculation for so many large and complex structures would be difficult if not impossible, so various levels of approximation are used to calculate the theoretical I–V curves. (See section 4.3.) The initial calculations were done using gas phase benzene and CO parameters and purely kinematic scattering within the overlayer to quickly map out parameter space. As the models became more complete, the multiple scattering was included more exactly. In the final structure the I–V curves were calculated using full multiple scattering within each adsorbate (using Matrix Inversion), Kinematic Sublayer Addition to add the benzene and CO sublayers, and Beam Set Neglect to add the overlayer and substrate diffraction.

Over 1600 distinct structures were tested with varying levels of calculational accuracy. At first, the role of CO was not understood, so the initial models only contained benzene. The benzene ring was allowed to distort in two ways. An in–plane Kekulé type distortion and an out–of–plane buckling to the chair or boat forms of cyclohexane. Without a coadsorbate in place, the 2–D benzene lattice is not tightly packed and there is not expected to be much of a barrier to the rotation of the benzene around the surface normal. Rotational disorder for the benzene molecule was modelled by averaging over many different angular configurations from 0–60° .

With a coadsorbate in place the benzene can no longer freely rotate due to steric hindrance between coadsorbates. A series of structures were tried with only a carbon atom in the lattice. The carbon atom never gave satisfactory agreement so it was given up in favor of a CO molecule. The HREELS results suggest CO is bonded to three metal atoms in a hollow site. Thermal desorption experiments and packing density considerations suggest two CO molecules in each unit cell. Top, bridge, and both kinds of hollow sites (fcc and hcp) were tried for both coadsorbates. The Rh–CO distance was varied as was the benzene to CO perpendicular distance (the final distances are labeled in figure 4.5). The in–plane Kekulé distortion of the adsorbed benzene was modeled with two structural parameters, the ring radius r and an angular deviation β to describe the long–short bond length alternation. The C–O bond length was initially fixed at 1.15Å but in the last stage of the calculation it was also varied.

The final structure was determined from the best fit between the theoretical and experimental I–V curves as judged by a minimum reliability factor (R–factor.) In the (3×3) structure shown in figure 4.5 both CO and benzene occupy hcp hollow sites (hollow sites with metal atoms below in the next metal layer.) The C–O bond length is slightly elongated to 1.17Å and the molecule is at a height of 1.30Å. This gives a Rh–C bond length of 2.02Å, just under the sum of the covalent radii.

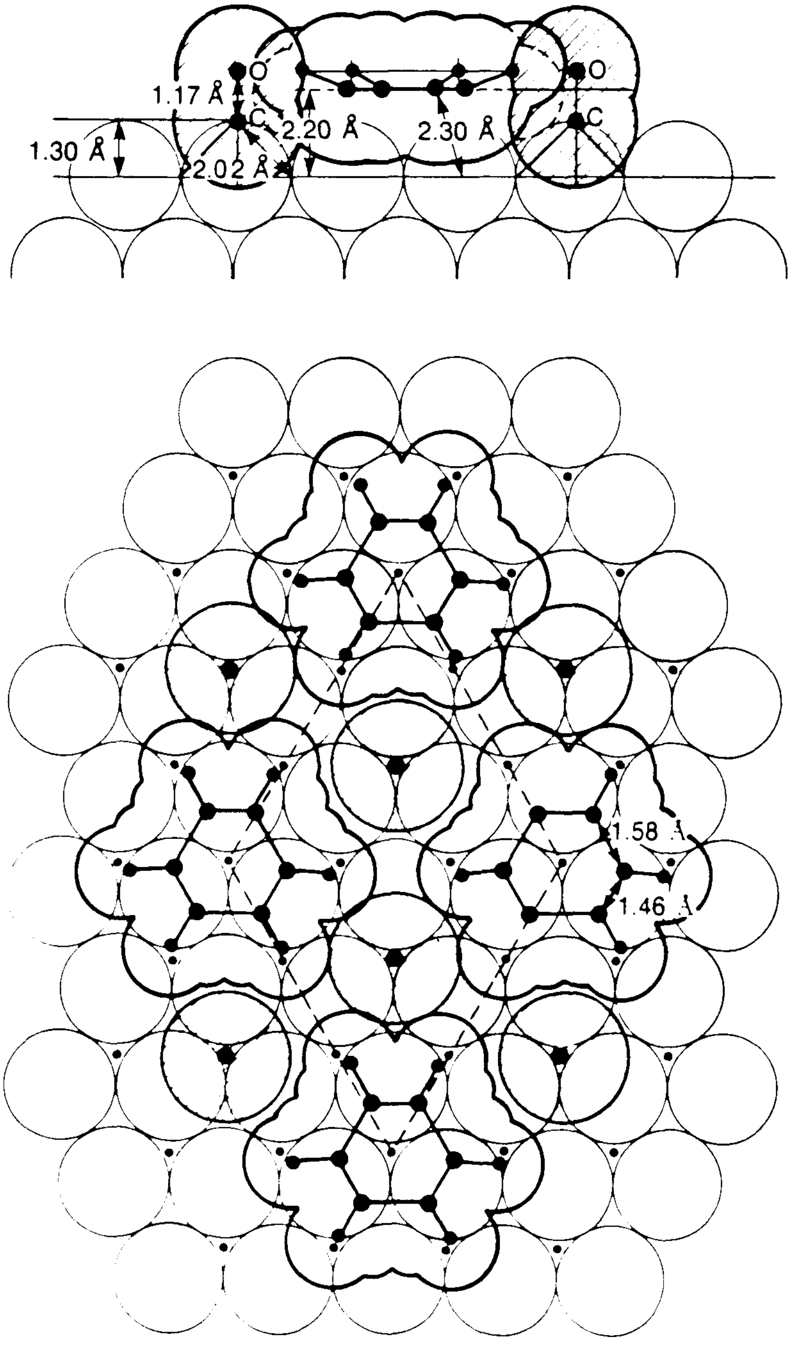

Rh(111) - (3×3) - C_6H_6 + 2CO

XBL 863 10701

Figure 4.5: Final structure for Rh(111) + (3 × 3) 2CO + benzene.

The benzene molecule is distorted slightly from its gas phase configuration. The molecular ring is expanded from a gas phase value of 1.397Å to 1.51Å after coadsorption. In addition the C–C bonds in the ring exhibit a slight Kekulé distortion. The long C–C bond is 1.58Å and the short bond is 1.46Å. The uncertainties on these values are ±0.15Å so the distortion is only barely significant. The best 5–R–factor average for the (3×3) structure is 0.21, which is quite low for such a complex structure.

4.4.4 Discussion of the Benzene Coadsorption Structures

Benzene and CO exhibit a rich variety of different ordered structures on various metal surfaces, many of which have been solved by our group. There are three ordered structures for benzene on Rh(111). The two coadsorbate induced structures $c(2\sqrt{3} \times 4)rect.$ [59] and the (3×3) [present study] have been solved by dynamical LEED calculations. On Pt(111) benzene by itself is disordered at all coverages, but upon coadsorption with CO two new ordered structures formed. One of these has been solved by LEED.[58] On Pd(111) pure benzene is also disordered, but there is a (3×3) ordered CO coadsorption phase, which was solved by Ohtani *et al.* .[60] Table 4.2 summarizes the solved CO plus benzene structures.

There are significant modifications in the CO and benzene bonding configurations as a result of the coadsorbate induced ordering. On Rh(111) the preferred adsorption sites change for both benzene and CO upon coadsorption. CO by itself bonds in only top sites at low coverages, with bridge and top sites populated in a 1:2 ratio at saturation.[23] Nevertheless, when coadsorbed with benzene, CO bonds in a hcp hollow site. None of the pure benzene structures have been solved yet, but on Rh(111) the pure benzene overlayer is ordered. As mentioned in section

Surface	CO/Bz	R	β	d_{C-C}	$d_{\perp M-Bz}$	d_{C-O}	$d_{\perp M-CO}$	site	γ_{CH}cm^{-1}	ν_{CO}cm^{-1}
Pt(111)	4/2	1.79,1.72	1.5°	1.65,1.76	2.10	1.15	1.45	bridge	840	1700,1800
Rh(111)	1/1	1.72	4.5	1.33,1.81	2.25	1.21	1.50	hcp hollow	780	1700
	2/1	1.51	1.3	1.46,1.58	2.20	1.17	1.30	hcp hollow	805	1655
Pd(111)	2/1	1.43	0.75	1.40,1.46	2.25	1.17	1.30	fcc hollow	730-770	1735

Table 4.2: Summary of structural parameters for the solved CO plus benzene structures on Pt(111)[58], Rh(111)[59], and Pd(111).[60]

4.4.1 the $(2\sqrt{3} \times 3)rect.$ has a glideline symmetry which restricts the structure to two benzene molecules in bridge sites related by the glide line. After coadsorption benzene shifts to the hcp hollow site for both the CO induced structures. On Pt(111)[58] both benzene and CO bond in bridge sites upon coadsorption; while on Pd(111)[60] the fcc hollow site is occupied.

The most surprizing result is the benzene distortions evident in all the coadsorbate induced ordered structures. Benzene is least distorted on the Pd(111) surface and most distorted on Pt(111), with Rh(111) somewhere in between. On Pd(111) the benzene has a very slight Kekulé distortion with a ring radius within error of the gas phase value (see table 4.2).

On the Rh(111) surface both of the ordered structures have benzene distorted into a Kekulé configuration. The (3×3) structure with two CO's per benzene is least distorted with bonds of 1.46 and 1.58Å for the alternating C–C bonds and a ring radius of 1.51Å. The benzene in the $c(2\sqrt{3} \times 4)rect.$ structure, with one CO per benzene, has large distortions. The long C–C bond is 1.81Å, which is 0.3Å longer than a typical C–C single bond. The benzene seems on the verge of decomposition, but it must still be intact because of the presence of ring modes in the HREELS. As the temperature is raised the ring modes start to disappear at 400K.[68] The short C–C bond is 1.33Å long, about the length of the ethylene C–C double bond. The short bond is centered above a top site, with the long bond bridging two rhodium atoms, as if the rhodium atoms were pulling pairs of carbons apart. The highly distorted benzene may be the precursor to dissociation into acetylenic type fragments, consistent with the hydrocarbon decomposition studies of Bent.[64]

Benzene on Pt(111) also exhibits distortions, but they are not the same as the Kekulé distortions on Rh(111) or Pd(111). As mentioned previously benzene and CO both bond in bridge sites on Pt(111). Kekulé distortions would not be consistent with the substrate symmetry of a bridge site. The benzene distorts in such a way as to maintain the bridge site mirror plane. The result is two shorter bonds (1.65Å) and four longer bonds (1.76Å). The ring radius is 1.79Å along the mirror plane and 1.72Å for the carbons either side of the mirror plane.

The benzene distortions for the coadsorbate induced ordered structures may have catalytic implications. The metal benzene interaction seems to increase from Pd to Rh to Pt ($d_{\perp M-Bz}$ = 2.25 - (2.25 and 2.20) - 2.10 for Pd, the two Rh structures, and Pt respectively). At the same time the C–C bond becomes weaker. The Pd(111) surface is one of the only surfaces which can catalyze acetylene trimerization to benzene in UHV. Neither Pt(111) nor Rh(111) will form benzene from acetylene, rather they both decompose benzene to form hydrogen and residual carbon.[68]

4.5 Nitric Oxide and Carbon Monoxide plus Ethylidyne

4.5.1 LEED Patterns

There is a complex evolution of LEED patterns and structures for the ethylidyne coadsorption systems. A flow chart of the different ordered structures as a function of temperature and coverage is shown in figure 4.6. In the LEED chamber 0.25 monolayer of ethylene and 0.25 monolayer of CO or NO were sequentially adsorbed at ~40K and then the crystal was heated to 200K to produce a sharp $c(4 \times 2)$ pattern. In general, pre– or post–adsorption of CO or NO to 0.25 monolayer of ethylene even at temperatures as high as 400K (where ethylidyne starts to decompose) will produce the $c(4 \times 2)$ pattern. Post–adsorbing NO with

0.25 monolayer of ethylidyne gives a much sharper $c(4 \times 2)$ pattern than for CO post-adsorption. On the right side of figure 4.7 are photos of the LEED patterns observed when various amounts of CO were dosed followed by saturation coverage of ethylidyne.

We were unable to produce the $c(4 \times 2)$ structure without addition of a coadsorbate, even though previous reports [63,66] indicated that slow annealing would do so. It is possible that an undetected impurity was responsible for the $c(4 \times 2)$ structure observed in the previous study. By annealing a saturated ethylidyne covered surface or by adsorbing above 270K we could reproducibly form a diffuse pattern of triangular clusters of spots at the (1/3,1/3) positions indicative of some short range ordering of the ethylidyne molecules in this temperature range, as shown in the lower right hand corner of figure 4.7.

4.5.2 HREEL Spectra of NO and CO plus Ethylidyne

The HREELS analyses, for the ethylidyne coadsorption systems, are used both to fingerprint the ethylidyne and to determine the sites for NO and CO adsorption. Figure 4.8 and table 4.3 summarize the HREEL analyses for the two coadsorption structures as well as each of the adsorbates by themselves.

Nitric oxide populates a new site after coadsorption with ethylidyne. Figure 4.8a shows the HREEL spectra for NO by itself on Rh(111) at about 1/4 monolayer coverage. The single strong peak at 1635cm^{-1} is similar to that observed by Root *et al.* [28], which they assign to NO bonded in a bridge site. Figure 4.8c is a spectra obtained from the NO induced $c(4 \times 2)$. The large peak at 1345cm^{-1} is indicative of the well-known ethylidyne species (figure 4.8e). The CH3 umbrella mode of ethylidyne can be used as a fingerprint for this species. For a

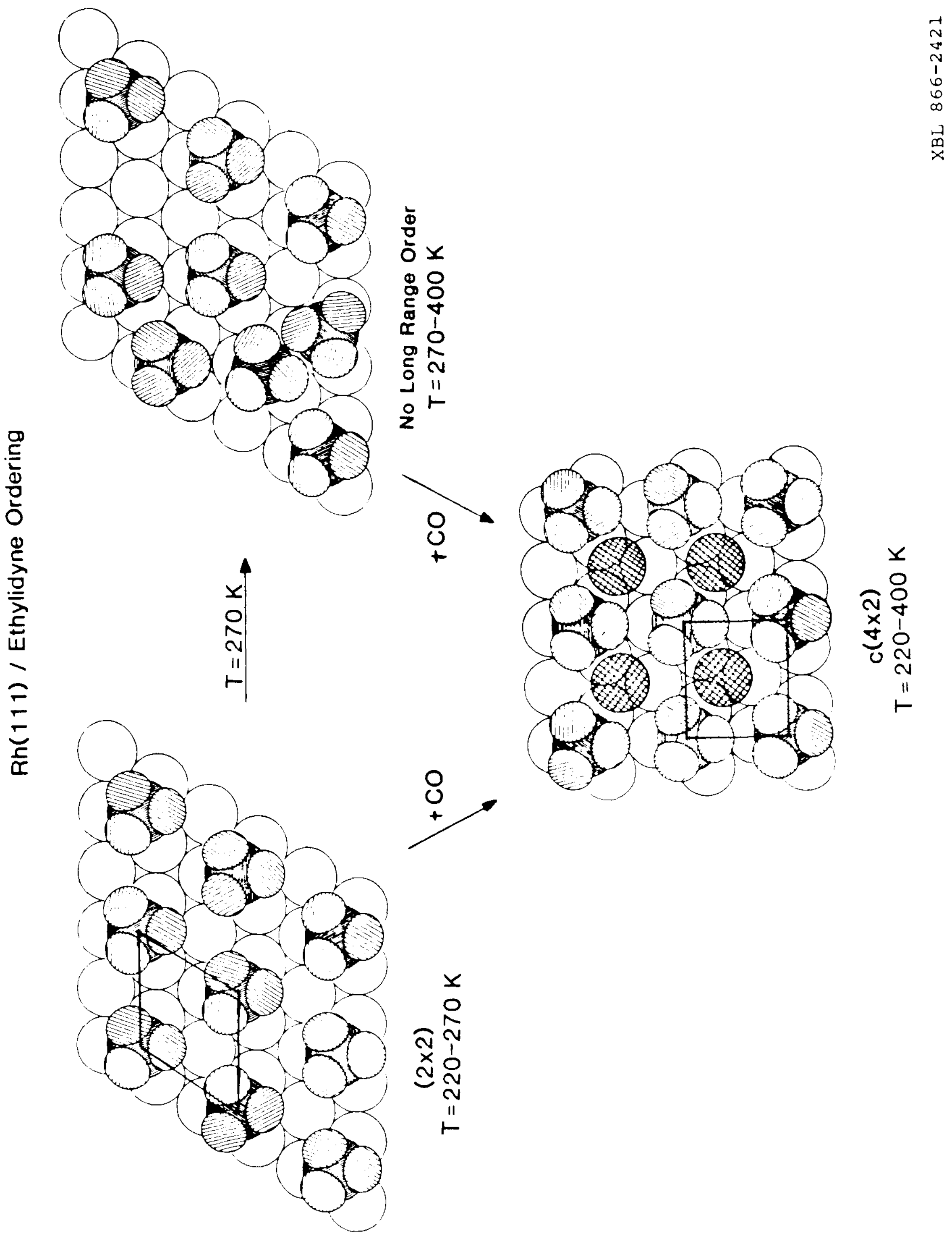

Figure 4.6: Schematic diagram of various pathways for production of the $c(4 \times 2)$ pattern of ethylidyne and CO on Rh(111).

Coadsorption of CO and Saturation Coverage of Ethylidyne

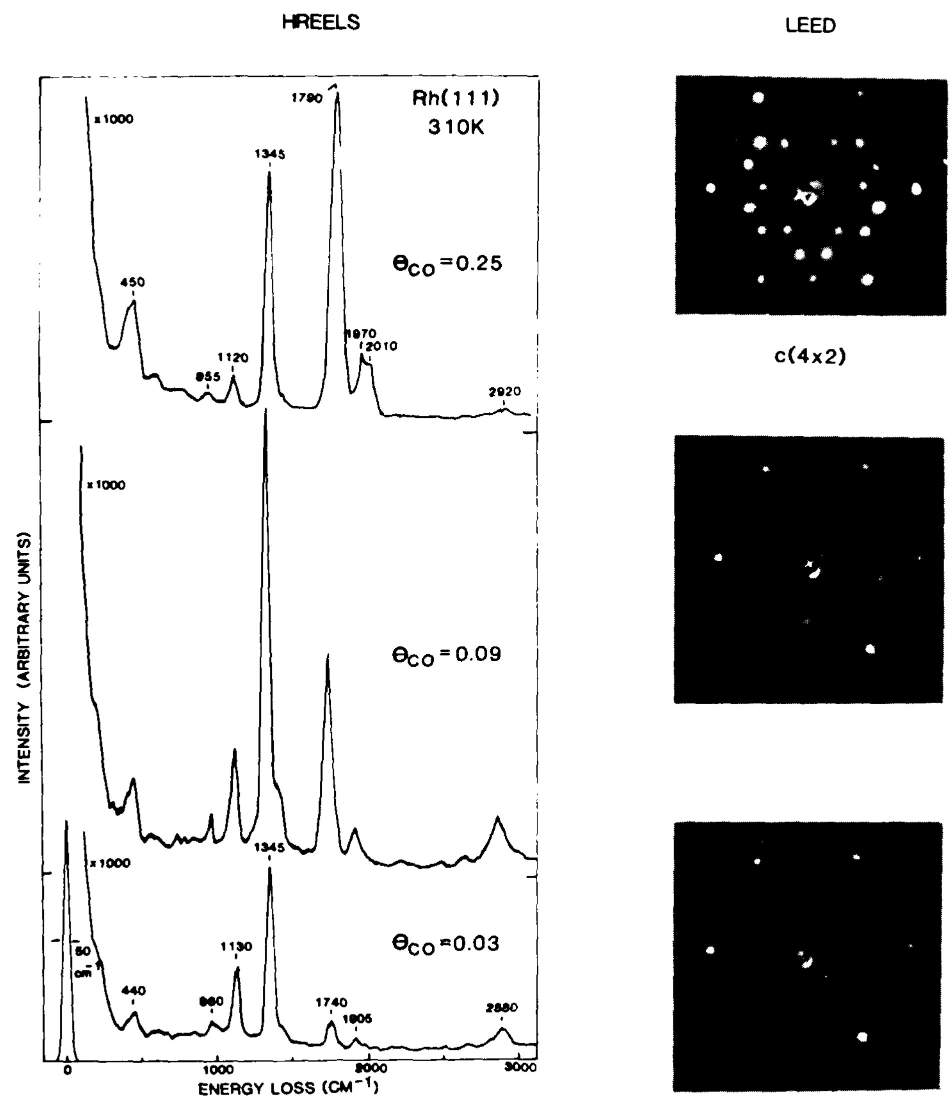

Figure 4.7: HREEL spectra of saturation coverage of ethylidyne with increasing quantities of CO and the corresponding LEED patterns at 310K.[56]

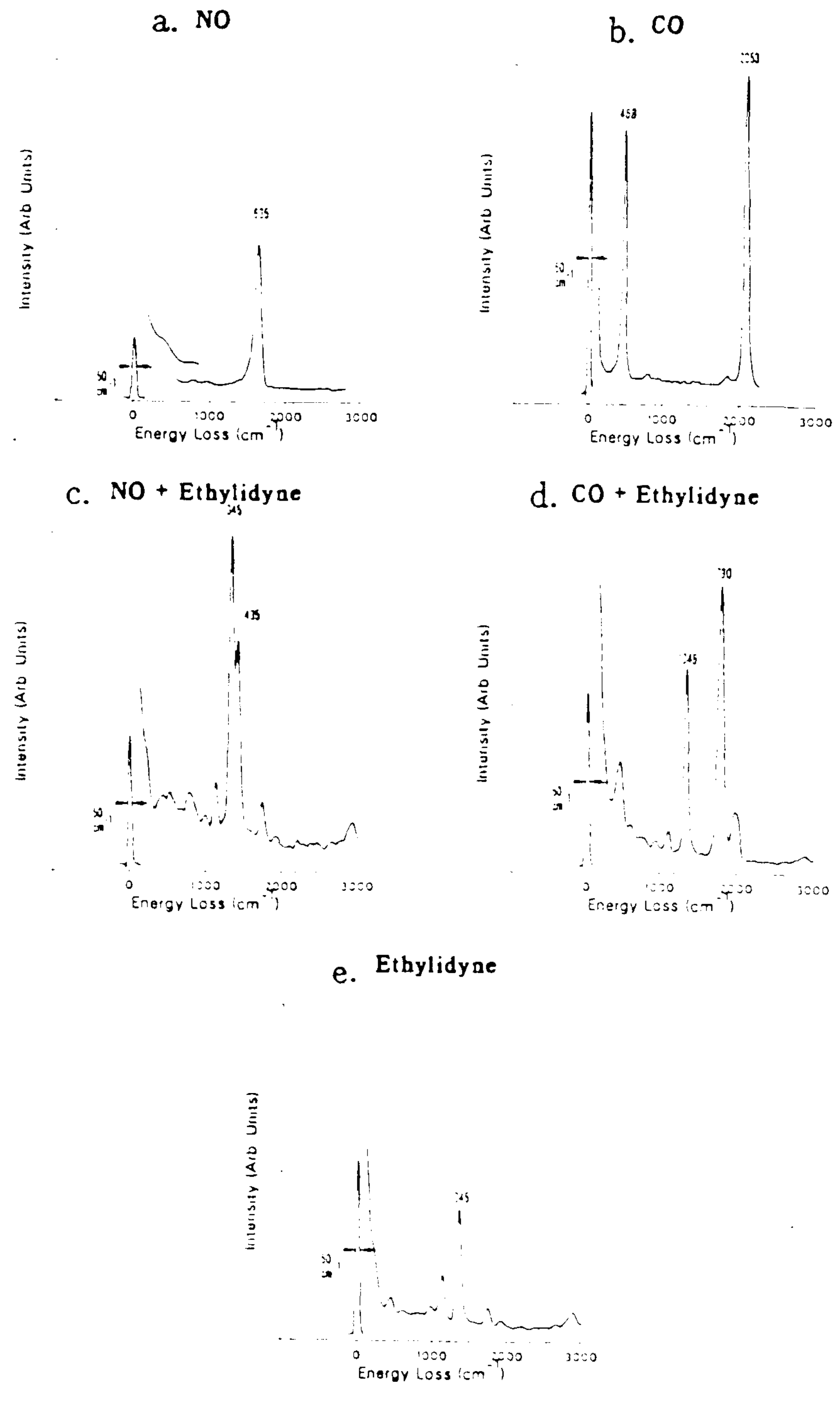

XBL 879-3975

Figure 4.8: HREEL spectra at room temperature for: a) NO alone; b) CO alone; c) NO + ethylidyne; d) CO + ethylidyne; e) ethylidyne alone.

Mode	$\nu_{s(C-O)}$	$\nu_{s(N-O)}$	$\nu_{s(C-C)}$	$\delta_{s(CH_3)}$	$\nu_{s(CH_3)}$
0.25 ML NO		1635			
0.25 ML CCH_3			1130	1345	2880
c(4x2)-NO+CCH_3		1435	1130	1345	2855
c(4x2)-CO+CCH_3	1790		1120	1345	2920
0.25 ML CO	2053				

Table 4.3: Comparison of vibrational frequencies (cm^{-1}) for NO, CO, and ethylidyne on the Rh(111) surface. (ν_s: symmetric stretch, δ_s: symmetric bend).

more complete discussion of the assignment of the vibrational modes of ethylidyne see reference [64]. Most of the modes in figure 4.8c are attributed to the ethylidyne species.(compare with figure 4.8e) The peak at 1435cm^{-1} is the only new one not directly attributed to hydrocarbon modes. While the peak at 1435cm^{-1} is at the right frequency for the antisymmetric CH_3 bend from ethylidyne, isotope shift experiments with deuterated ethylidyne prove it can not be a CH mode. After deuteration one would expect such a mode to shift downwards because of the heavier deuterium, but the mode remains at 1435cm^{-1} after deuteration[29]; therefore, it must be the N-O stretching mode. In view of the evidence, we assign the 1435 cm^{-1} mode to a N-O stretch. This frequency is much lower than any N-O stretch previously observed on the Rh(111) surface [28], however there are inorganic cluster complexes which exhibit N-O modes in this range (figure 3.2). [46,47,48] These compounds have the NO bonded to three metal atoms.

Carbon monoxide also shifts site upon coadsorption. The HREEL spectrum of CO by itself on Rh(111) is shown in figure 4.8b. At 0.25 monolayer coverage only two vibrational peaks appear in the spectra, one at 468cm^{-1} and one at 2053cm^{-1} . The two frequencies correspond to the Rh-CO and C-O stretching frequencies, respectively. When CO is coadsorbed with ethylidyne; however, a strong peak grows in at 1790cm^{-1} .(figure 4.7) This C-O stretching frequency is substantially lower than that observed for CO bonded at bridge (~1850cm^{-1}) or top (~2016cm^{-1}) sites on the clean Rh(111) surface [67], but is characteristic of CO bonded at three-fold hollow sites.[56,57] The small peaks around 1970 and 2010cm^{-1} are from contaminant CO in bridge and top sites outside of the ordered $c(4 \times 2)$ regions.

Based on the HREELS results we were able to propose a structural model for input into the LEED calculations.(cf figure 4.6) Both the N–O and C–O vibrations have shifted to substantially lower frequencies upon coadsorption (200cm^{-1} shift for NO and 260cm^{-1} shift for CO.) These large shifts are indicative of hollow site adsorption based on comparison with cluster compounds[46,47,48] and previous LEED studies.[59,69] In both coadsorbate induced structures the ethylidyne vibrational frequencies are almost identical to the ethylidyne by itself in a hollow site, indicating little change in its bonding geometry. The schematic diagram in the middle of figure 4.6 shows the preliminary structure. Although the HREELS analysis can help us determine the site of adsorption, it is not sensitive to the different types of hollow sites or to the detailed bond lengths and angles. LEED calculations are necessary to determine the precise structure.

4.5.3 Structural Search and Results for NO and CO plus Ethylidyne

In the case of CO + C_2H_3 we have made the following assumptions based on the HREELS results. The adsorbates are intact carbon monoxide and ethylidyne, bonded through carbon atoms to three Rh atoms in a three–fold hollow site. The molecular adsorbates stand perpendicular to the Rh(111) plane, see Figure 4.9.

Some minor off-normal tilting has been explored. No relaxation of the metal substrate from the bulk structure has been allowed, since none was found in previous LEED studies of molecules on Rh(111).

Six structural parameters were varied independently in our structural search. Table 4.4 shows their ranges of variation. The interlayer spacings between C and O of CO and between C and C of C_2H_3 were varied, as well as the two corresponding Rh–C spacings. In addition, the CO and C_2H_3 molecular axes were allowed to tilt away from each other. The tilt was investigated because, in the favored arrangement over two different hollow sites, a given molecule is not exactly at the center of the rectangle formed by its four nearest neighbors molecules. The tilting allows the top of the molecule to relax towards the center of this rectangle. The direction of tilt is chosen to respect the symmetry plane of the unrelaxed structure.

In all, 396 distinct geometries were tested for Rh(111)-*c*(4 × 2) -CO+C_2H_3 using the normal-incidence LEED I–V data. In addition, 96 structures were tested with the θ=21° data, in order to verify the structural result obtained at normal incidence.

In the case of NO + C_2H_3 on Rh(111), the same basic geometrical models were tested. Table 4.4 details these parameter variations, which yield 576 distinct geometries. The favored structures were very similar to those for the CO + C_2H_3 overlayer, so the theoretical I–V curves were calculated only at normal incidence.

The R-factor comparisons yielded similar structures for the two coadsorbed structures. The Rh(111)-*c*(4 × 2) -CO+C_2H_3 is shown in figure 4.9 and the Rh(111)-*c*(4 × 2) -NO+C_2H_3 structure in figure 4.10. The final structural parameters are collected in table 4.5. In both cases, adsorption over hollow sites was found to yield reasonable R-factor values and bond lengths. There are two

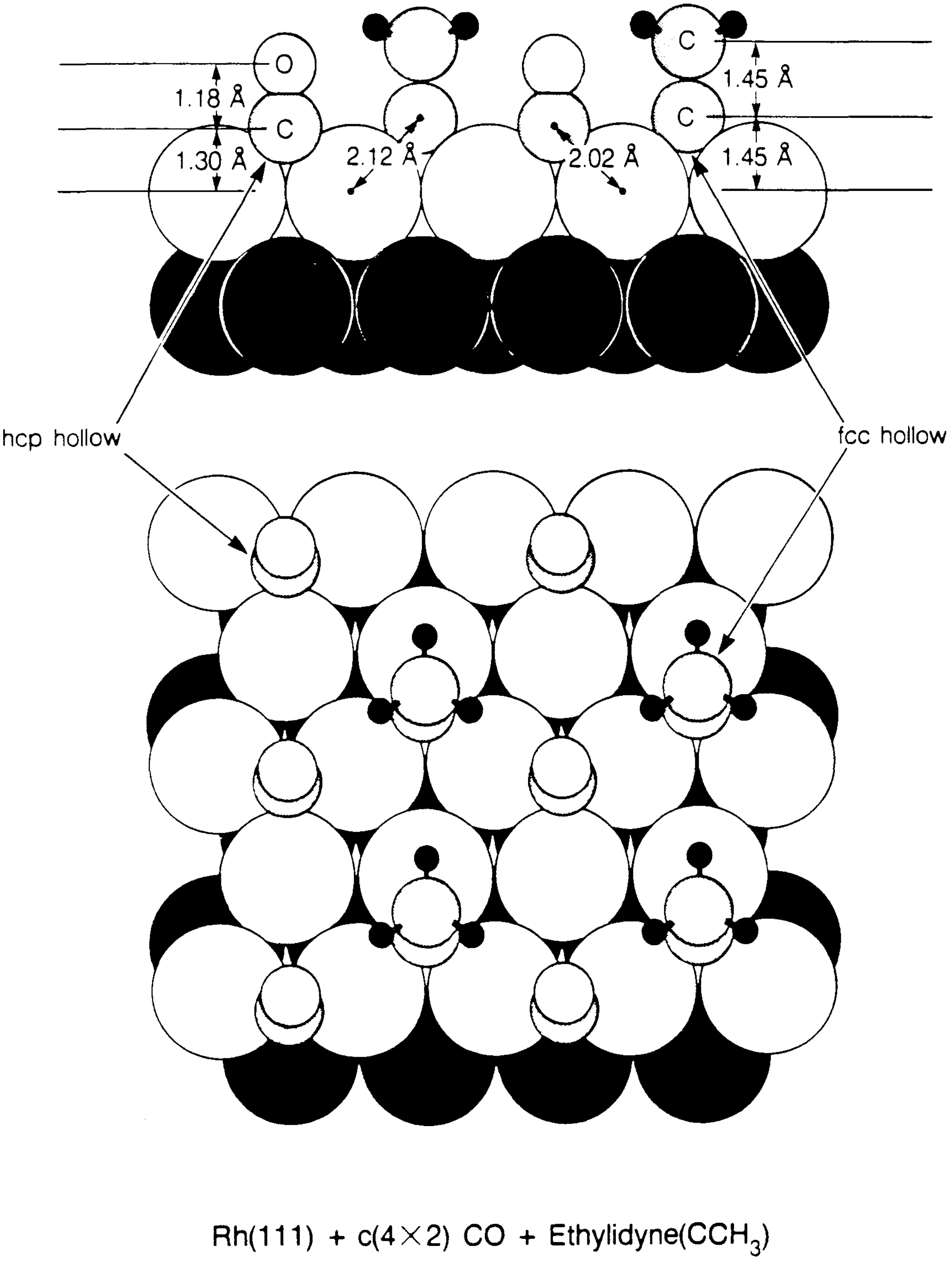

Figure 4.9: Final structure of Rh(111) + c(4 × 2) CO + C_2H_3 in side view(top panel) and near-perpendicular view(bottom panel), showing bond lengths.

CO				C_2H_3				
site	$d_{\perp Rh-C}$	$d_{\perp C-O}$	$\lvert d_{\parallel C-O}\rvert$	$d_{\perp C(CO)-C(C_2H_3)}$	site	$d_{\perp C-C}$	$\lvert d_{\parallel C-C}\rvert$	R
fcc	1.35(0.1)1.55	1.15	0	0.15(-0.1)-0.15	hcp	1.25(0.1)1.55	0	0.3354
hcp	"	"	"	"	fcc	"	"	0.2688
"	1.2(0.1)1.4	1.1(0.05)1.2	"	0.25(-0.1)-0.05	"	"	"	0.2596
"	1.2(0.1)1.5	1.175	"	0.25(-0.1)0.05	"	1.35,1.45	"	0.2561
"	"	"	0.2^a	"	"	"	"	0.2692
"	"	"	0.1^a	"	"	"	0.1^a	0.2691
"	1.2(0.1)1.4	1.15	$0.15,0.30^a$	0.1(-0.1)-0.1	"	1.35	0	0.2420
"	1.1(0.1)1.4	1.175	0.15^a	0.25(-0.1)-0.5	"	1.25(-0.1)-0.05	"	0.2450
"	"	"	$0.15,0.30^a$	"	"	"	"	0.2420
"	"	1.125,1.225	0.15^a	"	"	1.45	"	0.2497

NO				C_2H_3				
site	$d_{\perp Rh-N}$	$d_{\perp N-O}$	$\lvert d_{\parallel N-O}\rvert$	$d_{\perp N(NO)-C(C_2H_3}$	site	$d_{\perp C-C}$	$\lvert d_{\parallel C-C}\rvert$	R
hcp	1.1(0.1)1.4	1.15	0	0.25(-0.1)0.05	fcc	1.25(0.1)1.55	0	0.3265
fcc	"	"	"	"	hcp	"	"	0.3011
"	"	1.15(0.025)1.2	"	0.1(-0.1)0.1 -0.05(-0.1)-0.25	"	"	"	0.2961
"	"	1.10,1.175 1.20,1.25	"	0.2(-0.1)0.0	"	"	"	0.2943
"	"	1.175	$0.15,0.30^a$	"	"	"	"	0.3003

Table 4.4: Summary of the structures tested for Rh(111) + $c(4 \times 2)$ CO plus ethylidyne and Rh(111) + $c(4 \times 2)$ NO plus ethylidyne. (Ranges indicated have the following format: initial value (step) final value.)

Adsorbate(s)	$d_{\perp Rh-C}$	$d_{\perp C-C}$	$d_{\perp Rh-CO(NO)}$	$d_{\perp C-O(N-O)}$	site
$CO+C_2H_3$	1.45	1.45	1.30	1.18	hcp/fcc hollow
$NO+C_2H_3$	1.35	1.45	1.30	1.18	fcc/hcp hollow

Table 4.5: Summary of the final structural parameters for the ordered structures of CO + ethylidyne, and NO + ethylidyne. (The nitric oxide structural results for the (2 × 2) are from reference [49].)

different kinds of hollow sites on a fcc (111) surface. The hcp hollow has a metal atom directly beneath it in the next metal layer, while the fcc hollow does not. The dynamical LEED analysis may be the only technique which can distinguish between them. CO adsorbs in an hcp-type hollow site, while NO favors the fcc hollow site. The ethylidyne is bonded in different three–fold sites for the two structures, namely, when coadsorbed with CO it prefers the fcc hollow and with NO it takes the hcp hollow.

The local geometry of the ethylidyne is very similar in the two structures. The ethylidyne in both structures has its C–C axis perpendicular to the surface with a C–C bond length of 1.45±0.05Å. The CO molecule was found to be slightly tilted, by about 5±5° : shifting the O atoms parallel to the surface by 0.08Å improved the five-average R-factor from 0.259 to 0.242. The direction of tilt is away from the two nearest ethylidynes, towards the center of the rectangle formed by the four nearest ethylidynes in the mirror plane of the untilted geometry, see Figure 4.9. With NO, no evidence of a tilt was found. The optimum C-O and N-O bond lengths seem to be slightly elongated to 1.175±0.05Å, compared to the gas-phase value of 1.15Å.

For ethylidyne coadsorbed with CO or NO, we find Rh–C bond lengths of

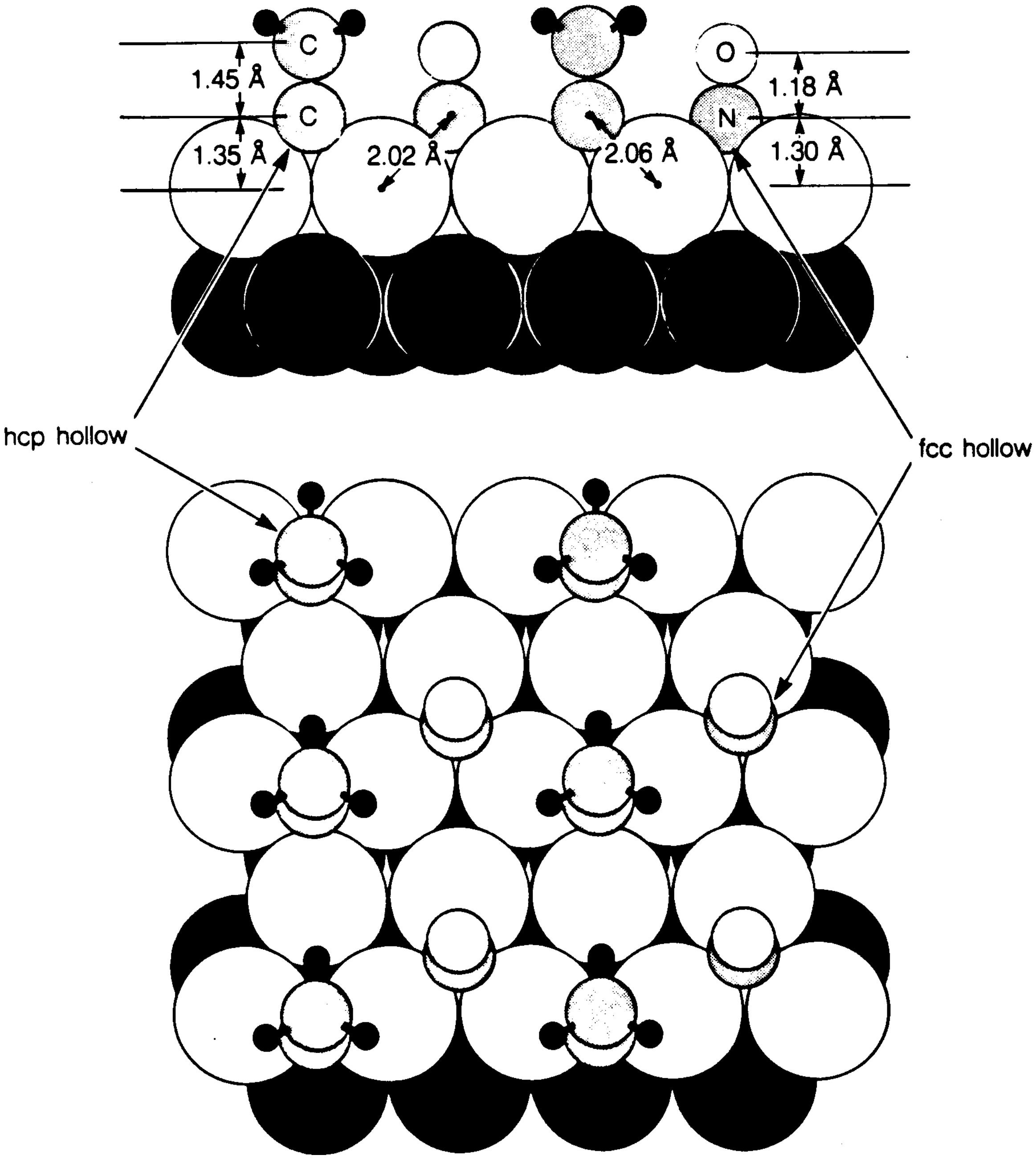

Rh(111) + c(4×2) NO + Ethylidyne(CCH_3)

XBL 877-7005

Figure 4.10: Final structure of Rh(111) + c(4 × 2) NO + C_2H_3 in same representation as figure 4.9.

Data Set	5-R average	R_{ZJ}	R_{PE}
CO+C_2H_3 0°	0.242	0.304	0.512
CO+C_2H_3 21°	0.242	0.348	0.517
NO+C_2H_3 0°	0.294	0.348	0.688

Table 4.6: Best values of the five R–factor average, the Zanazzi–Jona R–factor and the Pendry R–factor.

2.12±0.03Å and 2.06±0.03Å, respectively. These values correspond to interlayer spacings of 1.45±0.05Åand 1.35±0.05Å, respectively. For CO and NO the rhodium–C and rhodium–N distances are both 2.02±0.03Å, corresponding to spacings of 1.30±0.05Å, and consistent with the sum of the covalent radii.

The R-factor values for the optimum structures are shown in Table 4.6.

4.5.4 Discussion of the Ethylidyne Coadsorption Structures

The dynamical LEED calculations for the ethylidyne coadsorbate structures reveal some interesting points. First of all both NO and CO occupy three–fold hollow sites. CO by itself on Rh(111) prefers to occupy only top sites at low coverage with bridge sites becoming populated only at coverages above 1/3 monolayer (pressures around 1x10^{-5} torr or temperatures around 40K are required–see chapter 3 or reference [23]). As discussed in the previous section structural results for CO coadsorption with benzene show that CO bonds in an hcp hollow.[56,58,59,69] It is also known that, upon coadsorption of CO with a strongly electron donating species like potassium or sodium, the HREELS vibrational frequency decreases dramatically, which is again indicative of hollow site adsorption.[67] The hollow site adsorption appears therefore to be a common feature of CO coadsorption structures.

In addition to the hcp hollow adsorption for the CO, we also find a slight tilt of approximately 5° away from the surface normal in the ethylidyne coadsorption structure. In the high coverage (2 × 2) structure of CO on Rh(111), a similar tilt was suggested for top-site molecules.[23] The direction of the tilt in the coadsorption structure is such that the CO is leaning away from its nearest neighbor ethylidynes and towards a relatively open place in the unit cell. A possible reason for this behavior is steric repulsion between the electron orbitals of the CO and those of the ethylidyne; the same effect could also be responsible for the tilting observed in the (2 × 2) CO overlayer.

The NO molecules coadsorbed with ethylidyne bind in fcc hollow sites and exhibit an N–O stretching frequency of 1435cm^{-1} . Previous HREELS results by Root *et al.* [28] for NO adsorbed alone on Rh(111) showed that the N–O stretching frequency shifted continuously from 1480 to 1630cm^{-1} with increasing NO coverage. Root *et al.* suggest that the shift in frequency originates from large chemical and/or dipole–dipole interactions, between NO molecules bound in 2–fold bridge sites rather than a change in adsorption site. In contrast, Thiel and Weinberg [39] propose a possible three–fold adsorption site for NO on Ru(001) based on a HREELS stretching frequency in the range of 1379 to 1525cm^{-1} . The inorganic cluster compound $(C_5H_5)_3Co_3(NO)_2$ has a strong vibrational mode at 1405cm^{-1} .[46,48] Dimas *et al.* have synthesized and characterized the Rh analog of the above Co cluster[47] and they report the N–O stretch at 1392cm^{-1} . In both cluster studies the N–O stretching frequencies were assigned to NO bonded to 3 metal atoms in a hollow site.

We find a strong vibrational loss feature for pure NO on Rh(111) at around 1635cm^{-1} (5.0L exposure), This vibrational mode shifts substantially upon coadsorption: the new N-O stretch at 1435cm^{-1} , a full 200cm^{-1} shift, is consistent with hollow site adsorption. Our LEED analysis also indicates that the NO molecule when coadsorbed with ethylidyne, bonds in a hollow site (fcc hollow).

The adsorption sites of ethylidyne are different in the two structures: fcc hollow for CO coadsorption and hcp hollow for NO coadsorption. It can not be ruled out that the difference in adsorption sites for the two coadsorbed structures depends on the preparation procedure.

A previous LEED study of pure ethylidyne on Rh(111) [65] found the hcp hollow to be the favored site; however, upon coadsorption with CO the ethylidyne occupies the fcc hollow site. If CO is added after ethylidyne formation a microscopic shift for each and every ethylidyne within the ordered $c(4 \times 2)$ domains would be required. The observed LEED pattern produced under these conditions is poorly ordered, while if NO is used under the same conditions a sharp pattern is produced. This ordering phenomenon is consistent with the observed site shift.

4.6 Conclusions

Ordered coadsorption structures of benzene with CO, and ethylidyne with NO and CO have been analyzed with LEED surface crystallography. In both cases HREELS was used to discriminate between the manifold of possible structures and to provide a first model for the LEED calculations. A summary of the important results follows:

I. Benzene + CO coadsorption systems.

1. The complex coadsorbate induced CO plus benzene structures are the first test of the Beam Set Neglect approximation for large unit cells.

The various CO plus benzene structures are the first successes for LEED analyses of unit cells containing more than one kind of molecule.

2. The CO plus benzene structures on Rh(111) are the first LEED structural confirmation of CO bonded in a three–fold hollow site on any metal surface.
3. The Kekulé distortions and ring expansions may be implicated in the molecular transformation pathways by which benzene is catalytically produced from acetylene over metals.

II. Ethylidyne coadsorption systems:

1. The NO plus ethylidyne structure is the first example of nitric oxide induced ordering of a coadsorbate.
2. This is the first LEED study confirming NO bonding in a three-fold hollow site. CO also bonds in a three-fold hollow site when coadsorbed with ethylidyne.
3. It is possible to distinguish between the two kinds of hollow sites on the (111) surface by LEED analyses. NO bonds in a hcp hollow, CO in a fcc hollow, whilst ethylidyne switches between the two sites in the two coadsorption structures.

Finally a word about the mechanism of coadsorbate induced ordering. Looking through the various combinations of adsorbates which produce ordered patterns, and even more importantly those that do not, one trend is observed. In each instance of coadsorbate induced ordering one of the pair could be classified as having a positive surface dipole moment and the other a negative surface dipole moment. When two coadsorbates with similarly oriented surface dipoles are coadsorbed, the resulting overlayer is disordered or consists of segregated domains. This hypothesis is supported by work function measurements, which are presented in a separate publication[76] along with a more detailed discussion of the effect.

Chapter 5

Diffuse LEED

5.1 Introduction

Low–Energy Electron Diffraction(LEED) has been the major tool for surface structure determination. Over 200 surface structures have been determined through the use of conventional LEED techniques.[55] Conventional LEED techniques require the high intensities produced by diffraction from ordered surfaces. It has been possible in only one case (atomic oxygen on W(100)) to determine the surface structure of a ***disordered*** adsorbate with conventional LEED.[77] The diffuse intensity from a disordered overlayer is difficult to measure, because it is generally weak (i.e. two or more orders of magnitude less than the ordered intensities). We have developed a digital LEED apparatus which solves the measurement problem. Our apparatus is so sensitive it can easily measure the weak diffuse intensity from a disordered overlayer. We have used the new apparatus – and a recent theoretical development – to determine the first surface structure of a disordered molecule by LEED: disordered CO on Pt(111).

This chapter describes the use of digital LEED to determine the first surface structure of a disordered molecular adsorbate. The chapter will be organized as follows. An introduction to the new diffuse LEED technique and a survey of the literature to date will be presented first. Section 5.2 is a description of the digital LEED apparatus and the steps necessary to collect and manipulate the data. Section 5.3 contains a brief survey of the Pt(111) plus CO system which we have chosen for this first study. The next two sections, 5.4 and 5.5, detail the theoretical methods used and the structural search process, respectively. Section 5.6 discusses the structural result and how it fits in with previous work on the Pt(111) /CO system. Finally the conclusion section where the bright future for both diffuse LEED and digital LEED is discussed.

Normal LEED can be used to study certain forms of disorder on surfaces. At low coverages, some adsorbates tend to coalesce into small ordered islands driven by attractive interactions between the adsorbates. Broad diffuse spots are observed because the width of the ordered diffracted beams is inversely proportional to the size of the ordered patches. The spot profiles can be modeled theoretically and information about the size, shape and distribution of the islands can be inferred.[78,79]

Phase transitions from order to disorder or vice versa can be investigated by measuring the intensities of the LEED spots as a function of temperature [80] or coverage [81,82]. Moreover, the appearance of streaks or broad diffuse spots at certain coverages are a qualitative indication of disorder during a phase transition. However, neither the spot profile analysis nor the analysis of the intensity decay with temperature can be used to determine the structure of a disordered adsorbate.

In many cases, adsorbates on ordered single–crystal substrates occupy one or more sites with distinct local geometries, but without long–range order, a so–called lattice gas. In the absence of long–range order, it has never been possible to determine the structure with normal LEED. While fine structure techniques such as

Surface Extended X–Ray Absorption Fine Structure (SEXAFS), Near–Edge X–Ray Absorption Fine Structure (NEXAFS), and Angle–Resolved Photoelectron Emission Fine Structure (ARPEFS) can provide information on disordered adsorbates, these techniques are limited to adsorbates chemically distinct from the substrate and normally require a synchrotron light source. The "diffuse LEED" method extends the techniques of LEED structure determination developed for ordered overlayers to all types of lattice–gas disorder. Diffuse LEED can already be used to determine the structure of disordered atoms[77] and molecules (described more fully herein). It may eventually be used to determine the structure of disordered steps[83] or vacancies.[84]

The scattering process in diffuse LEED is no different for an electron interacting with an ordered or a disordered part of the surface. The difference lies in the constructive and destructive interference caused by the presence of long–range order. Any electrons which are scattered into the background, that is, in non–Bragg directions, must have interacted at least once with a disordered part of the surface. As Pendry [85,86] discusses, it is possible in the limit of low coverage to calculate the elastic diffuse scattering from a disordered overlayer by breaking the calculation up into three steps. The first step includes the incident electrons and each scattering event up to the first interaction with the disordered adsorbate and can be treated in the same way as diffraction from an ordered substrate.[50] The second step consists of all scattering paths which begin and end on the disordered adsorbate. This step can be treated by a cluster calculation similar to NEXAFS. The second step contributes only a small amount to the total since it consists of scattering paths which must be of at least third order.[87] The cluster radius is of the order of 4–5Å and is determined by the short mean free path of the electrons. The third and final step propagates the scattered wave field from the sample to the detector after its last interaction with the disordered adsorbate. This third step can also be handled as conventional diffraction from an ordered surface.

In such diffuse LEED studies one is interested solely in the disordered part of the surface. Pendry therefore suggests that long–range correlations can be removed using the Y–function:

$$Y(E) = \frac{L(E)}{(1 + L(E)^2 V_{0i}^2)} \tag{5.1}$$

where V_{0i} represents the imaginary part of the inner potential or the damping term, and L(E) is the logarithmic derivative with respect to energy:

$$\begin{aligned} L(E) &= \left(\frac{1}{I}\right) \frac{dI}{dE} &(5.2)\\ &= \frac{\mathcal{S}(\vec{q})}{I_{single}\mathcal{S}(\vec{q})} \times \frac{d\ I_{single}}{dE}. &(5.3) \end{aligned}$$

Here $\mathcal{S}(\vec{q})$ is the two–dimensional long range structure factor, while I_{single} is the intensity due to a single adsorbate. The long range structure factor is independent of energy and cancels out in the logarithmic derivative, leaving only the scattered intensity from a single disordered species on the surface. The formation of the logarithmic derivative in this way requires that the coverage be low so that there is no multiple scattering between adsorbates.

One may consider the diffuse intensity as a function of exit angle at a fixed energy or as a function of energy at a fixed parallel momentum transfer. Pendry and Saldin[85] and Saldin *et al.* [87] calculated the elastic diffuse intensity from a single oxygen atom above a Ni(100) surface and showed that the diffuse intensity was highly structured across the Brillioun zone. Pendry mentions that major changes in the experimental methods are necessary before meaningful theory/experiment comparisons can be made. The theory is based on calculation of the diffuse intensity across the Brillouin zone. This means that the experiment must be designed to collect and analyze the entire screen, rather than merely the ordered diffraction spots.

Heinz *et al.* were the first to be able to test the theoretical calculations with their study of oxygen on W(100).[77,88] The oxygen coverage was close to saturation in their study, so the requirement of a low coverage lattice gas was not obeyed, but they were able to determine the structure of the disordered overlayer nonetheless. A video camera with an image intensifier was used to collect the data as a function of exit angle at fixed energy. They took 24 horizontal cuts with 24 vertical pixels in each cut because it was not possible to collect the full image. Fine structure in the data from the energy selection grids was removed by a 5–fold 3 point smoothing routine, as well as local smoothing. The three–step theory was used and in the initial calculation the only structural parameter was the oxygen adsorption height. There was a well–defined minimum in the Pendry R–factor (< 0.2) at a height of 0.54Å. A later calculation, which included substrate relaxations using tensor LEED, reduced the R–factor to 0.05.[89]

We have recently developed a new, fast digital LEED apparatus which is sensitive enough to count single electrons.[18,90] Even the relatively weak diffuse scattering from a disordered adsorbate at low coverages is easily measured with this new technique. It is well suited for diffuse LEED studies, because the entire image can be obtained at a given energy in a matter of seconds with signal to noise ratios far higher than conventional video techniques.

Significant theoretical advances are needed to deal with the lack of periodicity, and superior experimental techniques are required to measure the diffuse intensities, which can be two or more orders of magnitude smaller than the intensities from the ordered substrate. This chapter describes the first application of a low–noise digital LEED system and an efficient new method for diffuse LEED calculations to determine bonding geometries for disordered CO on the Pt(111) surface at low coverages. We find that CO adsorbs in two distinct sites at 1/3 monolayer coverage, 88% top and 12% bridge. The bond lengths are 1.85±0.1Å and 1.55±0.1Å for top and bridge sites, respectively.

5.2 Experimental

We have recently developed a fast, sensitive "digital" or electron-counting LEED apparatus, schematically shown in figure 5.1. A brief description of the new digital LEED apparatus follows. (A more complete discussion can be found in section 2.6.

The digital LEED apparatus uses extremely small incident currents (~1pA) which eliminates any possibility of beam stimulated damage. The electron gun used to generate the low current electron beam is of a conventional design, but it has a very small (30micron) beam limiting aperture precisely located at the first crossover point of the electron beam. This aperture cuts down the current incident on the crystal to less than 1pA. Since CO on Pt(111) is sensitive to beam stimulated decomposition, this allowed us to complete the experiment without fear of changing the nature of the surface. During the entire set of experiments less than one unit cell in a thousand was hit by an electron.

The digital LEED detector was designed to optimize both speed and sensitivity. Because only about 5% of the incident current is elastically scattered, the detector must be extremely sensitive. The energy selection is accomplished with three hemispherical grids. The first is grounded; the second has the suppressor voltage applied; and the third is at the same potential as the front of the amplification stage. The amplification stage consists of two microchannel plates arranged in

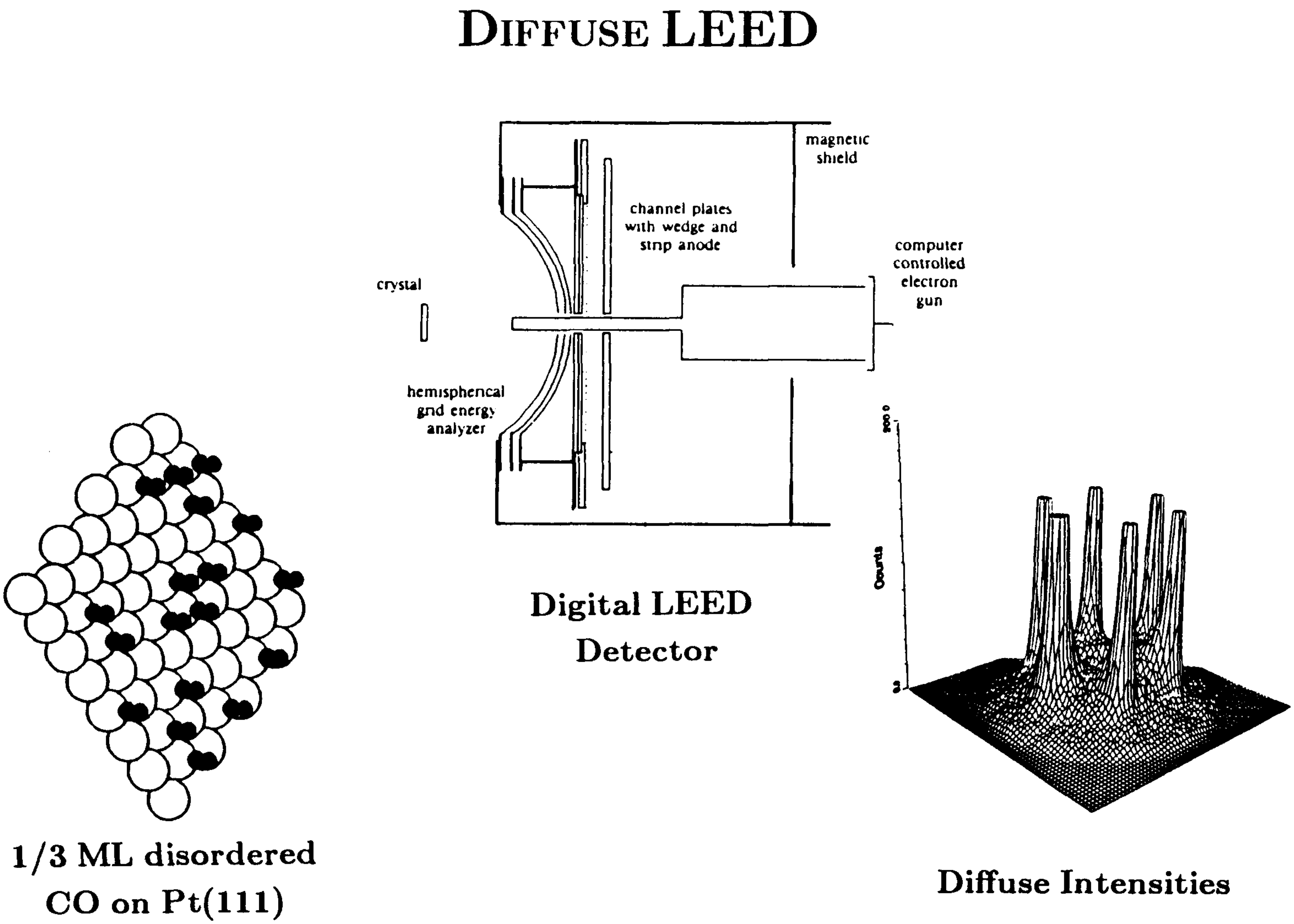

XBL 881-267

Figure 5.1: Schematic diagram of a diffuse LEED experiment.

a chevron array. There is a center hole in the plates for the electron gun.(See figure 5.1) By applying ~1keV bias to each plate, a total gain as high as 10^8 can be attained. The pulse of electrons exiting from the back of the channel plates travels through a field free region and is incident on a wedge–and–strip position sensitive anode. The anode consists of pure copper electrodes on a quartz substrate and was made using conventional photolithographic techniques. The rise time for each pulse on the detector is very fast (~50ns). The digitization electronics operate at about 200kHz. The factor which limits the count rate is the recharge speed of the microchannel plates, which become saturated in the local region around a LEED spot at ~25kHz. All the data for this study were collected at speeds of about 15kHz, well below the saturation level.

Digital LEED has no significant background and is only limited by statistical noise, with a signal–to–noise ratio determined by counting time. By comparison, conventional LEED uses currents of $\sim 1\mu$A, and a fluorescent screen with a video camera for detection.[17] Such currents can cause beam damage to the sensitive CO overlayer on Pt(111).[22] Because of the limited dynamic range, the signal to noise ratio is about 80 for a typical video camera. Video detection therefore, can only be used when the diffuse intensity is strong.

One potential problem with the current design of the digital LEED detector is that the quantum efficiency of the channel plates depends on the angle of incidence with respect to the front surface. Our channel plates consist of thousands of tiny channels tilted at 8° with respect to the surface normal. Each channel acts like a miniature channeltron; and, like a channeltron, the efficiency of amplification depends on the angle of incidence with the walls. The angle of the electrons incident on the front surface of the channel plates varies from 0–40° . This causes the efficiency of secondary emission to vary from 40 to 80%.[91] Initially, we applied a correction based on the reported angular efficiencies from Galanti *et al.* [91], but the channel plate configuration was different in their study. The optimal structural parameters were the same regardless of whether the quantum efficiency correction was included, so in subsequent studies we omitted this data manipulation step.

In addition to the quantum efficiency variation of the detector, there is a radial distortion of the pattern. The digital LEED detector produces a radially distorted pattern because the image is mapped onto a flat plate rather than a spherical screen. The distortion depends only on the geometry of the detector and is easy to correct for. Work is in progress to modify the detector to eliminate both the radial distortion and the quantum efficiency problems.

The surface used in this study was prepared by conventional techniques.[22] The sample temperature during data collection was ~160K and the CO coverage was maintained at about 0.3 monolayer. Normal incidence was used. The diffraction pattern, within about 50° of the surface normal, is projected onto the planar detector and is digitized on a 256x256 pixel grid. Each image contained a total of 10^6 counts and took between 50 and 90 seconds to collect at count rates well below the saturation level for our detector. Data were collected in energy ranges around 80 and 130eV. Corresponding diffuse intensities were also measured for the clean surface, for a background subtraction process suggested by Ibach and Lehwald[92] and discussed below.

There are a few steps of data massage necessary before the raw digital LEED data could be compared to the theory. The first step, mentioned above, is to correct for the radial distortion of the detector. The next step in the data manipulation is to average it to the coarser grid spacing used in the theoretical calculations. The experimental data consists of a 256x256 array of pixels and the theoretical pixel grid is much coarser (41x41). About 40 experimental pixels are averaged into each theoretical pixel which smooths the data to some extent. See figure 5.2 for the results of the data manipulation.

Elastic diffuse scattering from the disordered overlayer is not the only diffuse contribution to the digital LEED images. Any disorder, such as steps, kinks or defects, left on the surface after cleaning will contribute to the diffuse intensities. The energy resolution for a retarding field analyzer, like the one in the digital LEED apparatus, is seldom better than 1eV. Therefore, the experimental diffuse intensities also have contributions from phonons. Ibach *et al.* have suggested that the phonon contributions can be removed by subtracting the clean surface diffuse intensities from the intensities obtained after the addition of the disordered overlayer. Therefore, we collect the data for the clean surface just prior to the data for the disordered CO. The background subtraction is discussed in section 5.6.

The final step of data manipulation is to construct the Y–function. The logarithmic derivative is obtained by using two images separated by a small energy difference ($\triangle$E is typically about 2eV). The derivative is taken at constant parallel momentum transfer so the images must be corrected for the change in the scale of the pattern with energy. After this step the comparison with theory can be performed.

5.3 Pt(111) + Disordered CO

For our studies, we chose carbon monoxide adsorbed in a disordered monolayer on the Pt(111) single crystal surface. The adsorption behavior of CO on Pt(111) has been studied by both High–Resolution Electron Energy Loss Spectroscopy (HREELS)[93] and Infrared Reflection Absorption Spectroscopy (IRAS)[31], as well as conventional LEED[22], but there still is not general agreement on the site

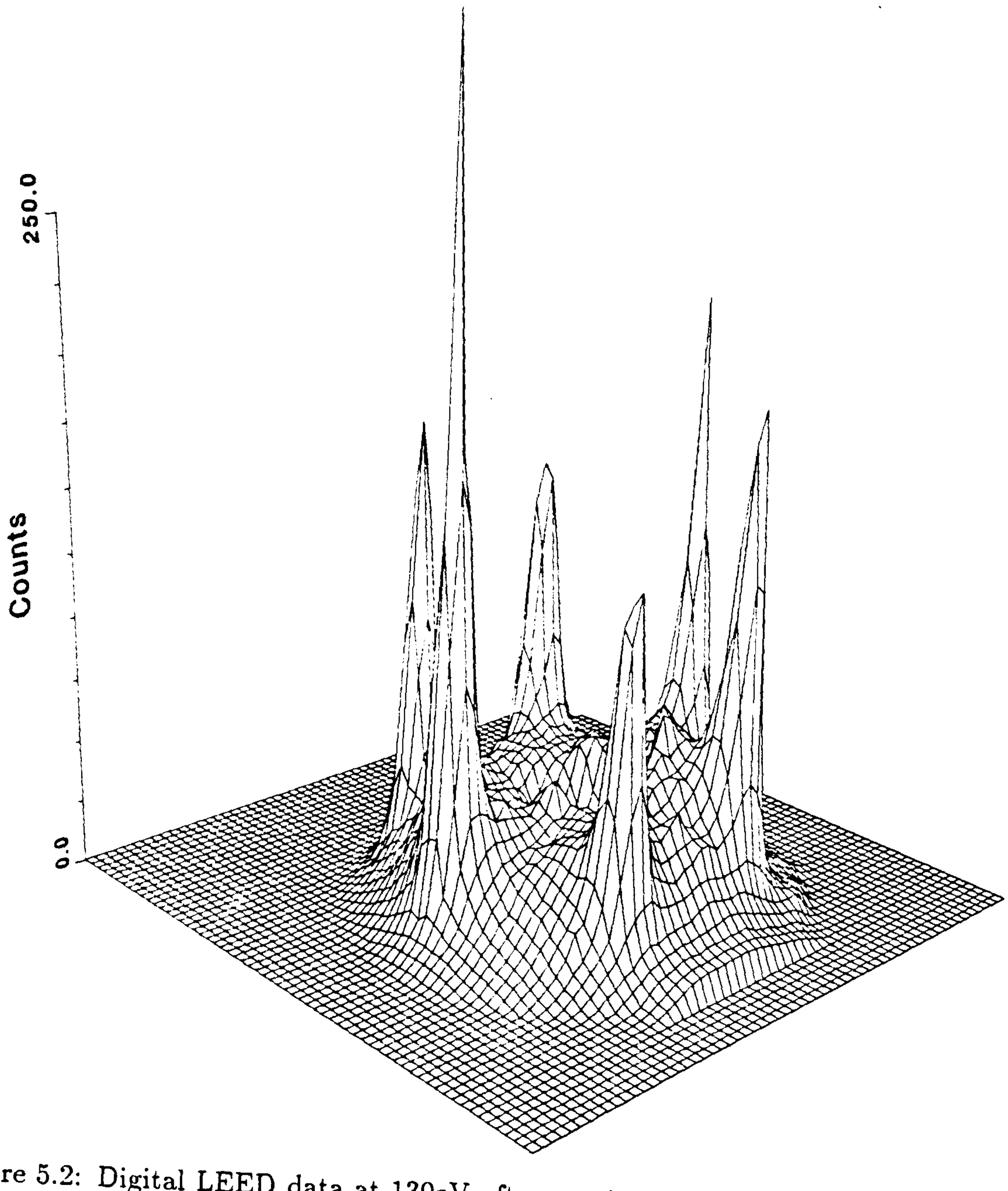

Figure 5.2: Digital LEED data at 130eV after manipulation. The two horizontal axes are in k-space coordinates, the vertical axis is the averaged intensity.

occupancy with coverage or temperature. At low coverages ($\theta < 0.17$ monolayer, where one monolayer corresponds to one CO per Pt surface atom) at a temperature of 92K, a single C–O vibrational frequency is observed at 2100cm^{-1} in the HREEL spectra. This frequency is attributed to CO adsorption at top site. As the coverage is increased a new loss peak grows in at $\sim$ 1850cm^{-1} . This mode is assigned to CO bonded to two metal atoms in a two–fold coordinated bridge site.[93] The IRAS results are not in agreement about the coverage necessary for the bridge sites to first be populated and they include an additional lower frequency mode at $\sim$1810cm^{-1} , which is attributed to CO in a three–fold hollow site.[31]

In the coverage range $0.35 < \theta < 0.5$ and just below room temperature, CO orders into a c(4x2) arrangement on the surface. Ogletree *et al.* [22] have carried out a LEED structural analysis of this ordered overlayer at 0.5 monolayer coverage. The LEED structural results confirm the vibrational assignments of the two modes to top and bridge sites. Both CO molecules bond with their molecular axis perpendicular to the surface and the carbon end down with a C–O bond length of 1.15Å. The Pt–C distances perpendicular to the surface are 1.85 and 1.55Å for the top and bridge sites, respectively.

We observed no long range order when the coverage was below 0.35 monolayer at a temperature of 160K. Yet, there remains weak diffuse scattering from the disordered overlayer. This is the focus of our investigation.

5.4 Theory

A multiple–scattering theory of diffuse LEED should calculate the probability that an electron scatters at least once from a disordered adsorbate. We shall ignore scattering from one adsorbate to another; therefore, the structural model consists of a single adsorbate on a perfectly ordered substrate. Ignoring scattering between adsorbates will be a good approximation as long as the coverage is not too high (in practice, a half monolayer or less is adequate).

In the three–step theory of Pendry *et al.* [85,86], the electrons from the middle step must have scattered at least three times, one of which must have been a backscattering event. Therefore, the contribution to the total intensity is generally weak. In the present extension[87] of beam set neglect[52,94], this step is simplified by using only the available plane waves, rather than the spherical wave representation for scattering between adsorbate and substrate. The three steps can then be efficiently combined and computed in the plane–wave representation. Multiple scattering within the adsorbate is included exactly by matrix inversion, as in ordered polyatomic layers.[50].

Diffuse LEED intensities due to adsorbates at different bonding sites can simply be added incoherently. This is an approximation which becomes exact in the low-coverage limit, but is already very good at the coverages common in adsorbed layers, such as for 1/3 to 1/2 monolayers. As a result, it is relatively easy to study simultaneous adsorption at different sites.

To summarize, we treat the surface as composed of a separate overlayer with one bonding site at a time and individual substrate layers. For each layer, diffraction matrices are obtained as in conventional LEED[50], but only for two sets of beams: the set of integral-order beams due to the incident beam and a replica of this set which is shifted in parallel momentum space in such a way that the detected direction is included. The calculation is repeated for each detected direction. Renormalized forward scattering is used to stack the layers.[50]

The physical parameters in the calculations are the same as those chosen previously for the ordered system Pt(111)-c(4x2)-2CO.[22] We follow Heinz *et al.* for the comparison between theory and experiment and apply the Pendry R–factor to the Y–function of the intensity rather than to the intensity itself.[77]

$$R_{Pendry} = \frac{\int (Y_e - Y_t)^2 dE}{\int (Y_e^2 + Y_t^2) dE}$$

where Y is the Y–function defined by equation 5.1. This procedure removes long–range pair correlation effects from the data, but not local bonding information.

5.5 Structure Determination

A number of structural possibilities were tested for our disordered CO layer on Pt(111). We made a few simplifying assumptions based on the solved Pt(111)-c(4x2)-2CO structure.[22] The substrate was kept bulk-like, while the CO molecules were taken to be intact and perpendicular to the surface, with a C–O bond length of 1.15Å . The two metal-carbon interplanar spacings, one for the top site and another for the bridge site, were varied independently. Many mixtures of top- and bridge-site occupations, from 100% on top to 100% on bridge, were also tested.

Using the Pendry R–factor to assess the fit between theory and experiment, we determined the optimal structure. In figures 5.3 and 5.4, we show R–factors for representative sets of adsorption structures, using the 130eV data set. Choosing 90% of top sites and 10% of bridge sites (near the best mix we have found), we explored the independent variations of the two metal-carbon spacings; this is shown in figure 5.3 with a two-dimensional contour plot. A clear minimum is found near the spacings $d_{\perp top} = 1.85$Å and $d_{\perp bridge} = 1.55$Å, the values found earlier in the ordered c(4x2) structure. Assuming the above interlayer spacings, the dependence on the site mix is illustrated in figure 5.4. A surprisingly sharp minimum is visible near 90% top–site and 10% bridge–site occupation. Interpolation yields a minimum at 88 ± 5% and 12 ± 5%. Subtraction of the clean–surface diffuse intensity has no significant effect on this result for the 130eV data set. However, the background subtraction step was important for the data at 80eV (discussed below).

5.6 Discussion

The structure of disordered CO on Pt(111) is in agreement with the ordered c(4x2) arrangement studied by Ogletree.[17] The HREELS[93] and the IRAS[31] results do not agree on which sites are populated and at what coverage, but both studies suggest multiple sites. The HREEL spectra show only top and bridge sites occupied at 1/3 monolayer coverage, while the IRAS suggests a 3–fold hollow site in addition to the top and bridge sites. It is not easy to estimate the relative site occupancy quantitatively from the surface vibrational spectroscopy, because the phonon excitation cross–sections are not known.

The R–factor drops considerably when different combinations of top and bridge sites are used. By interpolation the minimum R–factor is 0.55 at 88% top and 12% bridge. Our results are consistent with the sequential adsorption model proposed by Steininger[93] where top sites are populated first.

The two sets of experimental data at different energies obtained for disordered CO on Pt(111) gave the same optimal Pt–C bond lengths. However, the minimum in the R–factor versus relative site occupancy depended on the background subtraction step. The diffuse intensities for the clean surface at 80 and 130eV are shown in figure 5.5. Since the energy selection for digital LEED is done with traditional hemispherical grids, the energy acceptance window is as large as 1eV. Both the elastic and quasi–elastic electrons are therefore included in any LEED

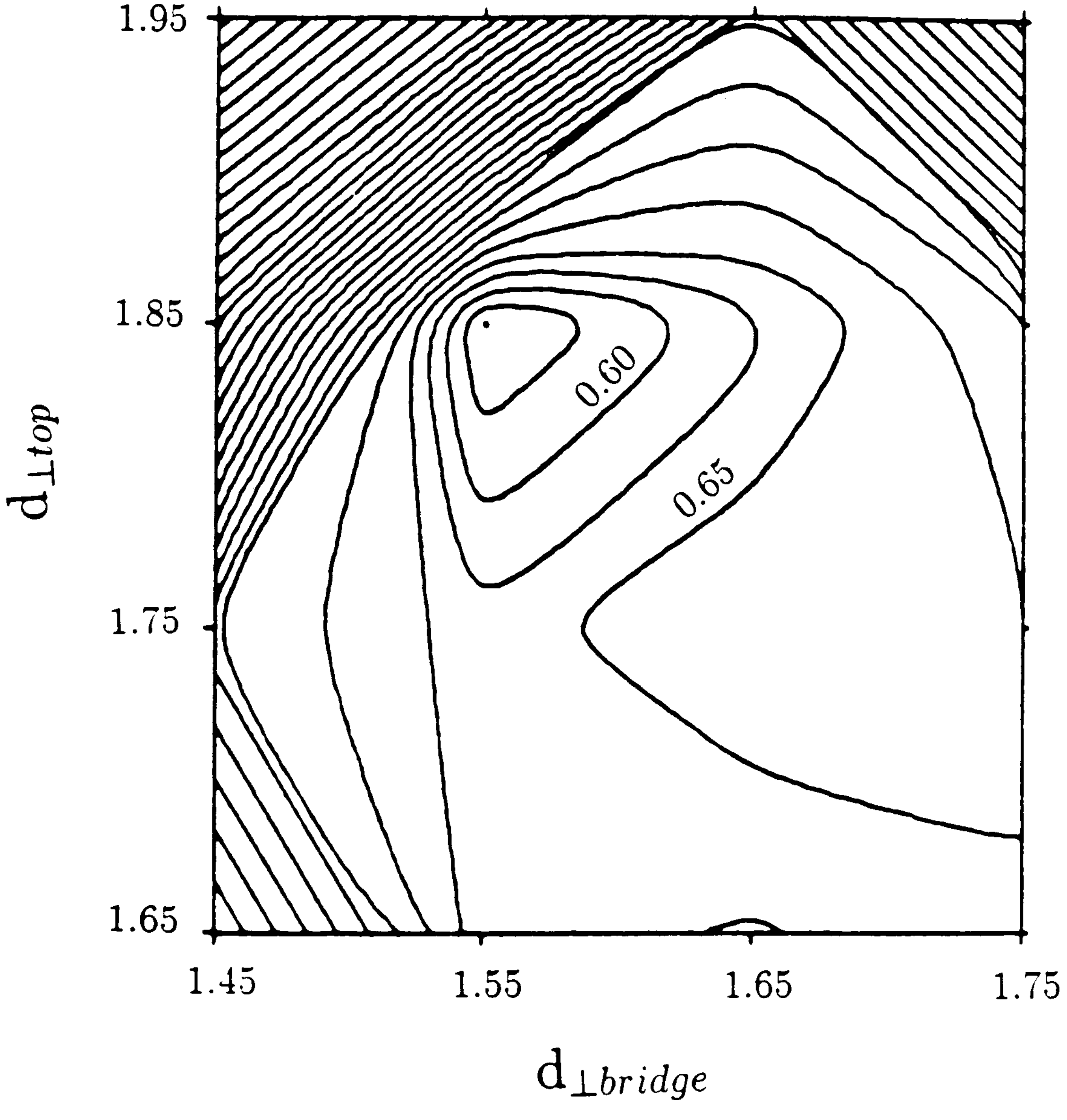

XBL 884-1277

Figure 5.3: Two dimensional contour plot of R-factor variation with the Pt–C distances for top and bridge sites.

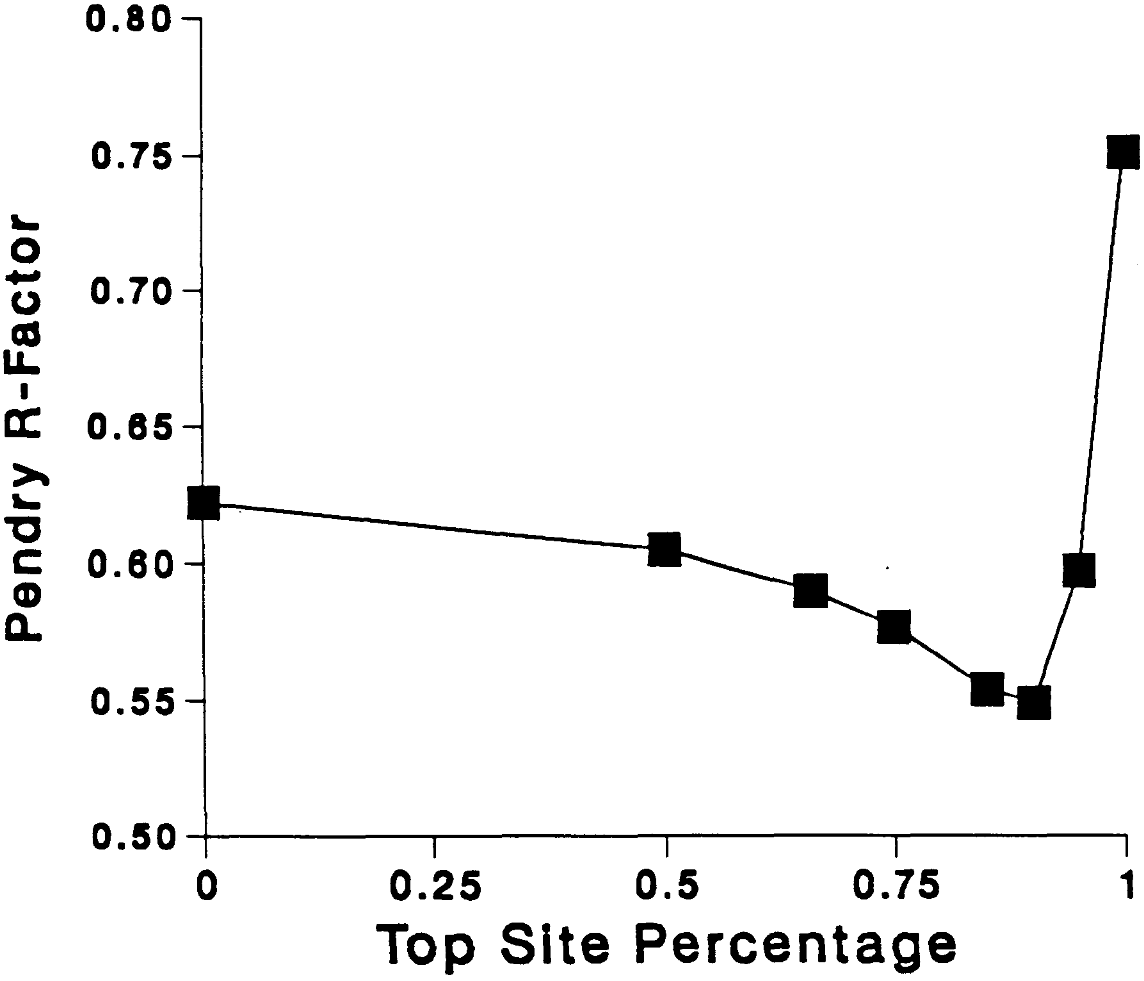

XBL 884-1275

Figure 5.4: R–factor variation with relative top site occupancy.

pattern. These quasi–elastic electrons include most of the phonon losses which are in the 0.1eV range just below and above the elastic peak. Also included in the clean surface background intensities are any electrons which have scattered from defects or steps left on the surface after cleaning. There is structure in the diffuse intensities from the clean surface and the magnitude of the diffuse intensity for the 80eV data set is larger than that for the 130eV set. The large amount of diffuse intensity from the substrate at 80eV could be the reason for the importance of the background subtraction at this energy.

Ibach and Lehwald have already suggested that diffuse LEED data can contain sizable inelastic contributions,[92] which can be attributed to the quasi–elastic electrons having undergone phonon losses. They have shown that the HREELS contribution can, at some energies and angles, be larger than the proper elastic diffuse intensity of interest in diffuse LEED. As a partial remedy, they suggest subtracting the intensities due to the clean surface from those due to the overlayer–covered surface. This approach is supported by theoretical estimates of the phonon contribution to diffuse intensities which show that almost all phonon losses occur in the substrate.[95]

The best R–factor value of about 0.55 obtained here is not as good as that found in the O/W(100) structure analysis.[88] On the other hand, it is our experience that R–factor values for ordered molecular adsorbates are rather higher than for ordered atomic adsorbates. The same could be expected in the disordered case.

5.7 Conclusion

The two bonding geometries which we obtained for disordered CO on Pt(111) agree, to well within our error bars of ±0.1Å, with those obtained earlier for

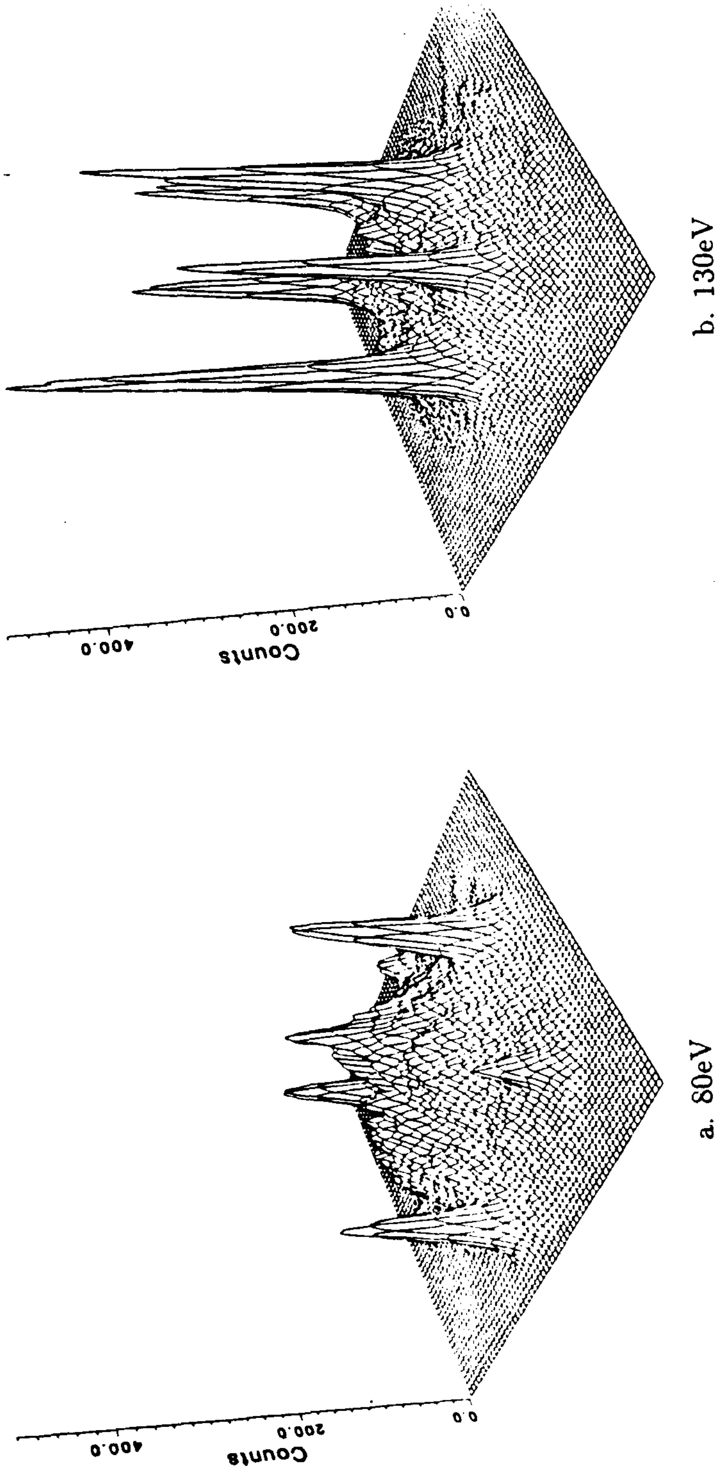

Figure 5.5: Thermal diffuse intensities from the clean surface at a) 80eV and b) 130eV. The horizontal axes are k–space coordinates and the vertical axis is intensity.

ordered CO on Pt(111). In addition, our 88% – 12% mix of top and bridge sites (based on data that are less affected by the clean–surface background) is consistent with the HREELS results.

We have shown that our new digital LEED technique has sufficient sensitivity to easily measure the low intensities from disordered molecular adsorbates on an ordered surface. Conventional techniques would not have worked in this case because they are not sensitive enough. Using these diffuse intensities we were able to obtain the complete local surface structure of a disordered molecular overlayer for the first time. It was not only possible to obtain local molecular bonding geometries, but also to determine the relative occupation of different adsorption sites.

The limited dynamic range of the video LEED method, combined with the difficulty of collecting an entire screen of data, has slowed experimental contributions to diffuse LEED. However, the theory of diffuse LEED is continuing to move forward. Rous *et al.* used the three–step theory of diffuse LEED formalism to calculate the elastic diffuse scattering from a random distribution of vacant sites on a Cu(100) surface.[84] Significant structure in the diffuse intensities across the Brillouin zone was noted, even without including the inevitable relaxations around the vacant site. In a later study, the diffuse scattering from a random distribution of steps on the same surface was calculated.[83] The three–step formalism had to be modified for this study because the implicit assumption of no multiple scattering between disordered adsorbates was no longer true. Scattering between chains of atoms parallel to the step edge is strong and had to be included in the theory.

In each of these theoretical studies, the Y–function was extremely sensitive to the structural details of the models. Now that a sufficiently fast and sensitive experimental apparatus has been developed, more complex disordered molecular adsorbates, defects, and even disordered steps should be amenable to LEED structural analysis.

Bibliography

[1] A.W. Adamson, *Physical Chemistry of Surfaces*, (J. Wiley and Sons, New York, 1982).

[2] J.F. O'Hanlon, *A User's Guide to Ultra High Vacuum Technology*, (J. Wiley and Sons, New York, 1980).

[3] R.G. Musket, W. McLean, C.A. Colmenares, D.M. Makowiecki, and W.J. Siekhaus, *Appl. Surf. Sci.* **10** (1982) 143.

[4] Gabor A. Somorjai, *Chemistry in Two Dimensions*, (Cornell University Press, Ithaca, 1981).

[5] Clifftronics Inc. Model CE406 electron gun, Clifton, NJ 07013.

[6] R.N. Lee, *Rev. Sci. Inst.* **39(9)** (1968) 1306.

[7] D. Briggs and M.P. Seah, *Practical Surface Analysis by Auger and X-Ray Photoelectron Spectroscopy*, (J. Wiley and Sons, Chichester, England, 1983).

[8] G. Ertl and J. Küpper, *Low Energy Electrons and Surface Chemistry*, (Verlag Chemie, Weinheim, 1974).

[9] C. Benazeth, N. Benazeth, and M. Hou, *Surf. Sci.* **151** (1985) L137.

[10] A.J. Slavin, *J. Elect. Spect. and Rel. Phen.* **40** (1986) 181.

[11] E.G. McRae, *Surf. Sci.* **11** (1968) 479.

[12] E.G. McRae, *Surf. Sci.* **11** (1968) 492.

[13] W. Ehrenberg, *Phil. Mag.* **18** (1934) 878.

[14] E.J. Scheibner, L.H. Germer, and C.D. Hartman, *Rev. Sci. Inst.* **31(2)** (1960) 112.

[15] J.J. Lander, J. Morrison, and F. Unterwald, *Rev. Sci. Inst.* **33** (1962) 782.

[16] Yoshikatsu Namba and Toshio Mōri, *J. Vac. Sci. Tech.* **A4(4)** (1986) 1884.

[17] D.F. Ogletree, G.A. Somorjai, and J.E. Katz, *Rev. Sci. Inst.* **57** (1986) 3012.

[18] D.F. Ogletree, PhD thesis, University of California, Berkeley, CA 94720, 1986.

[19] IP–512 System, Imaging Technologies, Inc., Woburn, MA.

[20] For schematics of the electronics contact Joe Katz at Lawrence Berkeley Labs, Berkeley CA 94720.

[21] MCP-75mm-6mm-CH, Galileo Electro-Optics Corp., Galileo Park, Sturbridge, MA.

[22] D.F. Ogletree, M.A. Van Hove, and G.A. Somorjai, *Surf. Sci.* **173** (1986) 351.

[23] M.A. Van Hove, R.J. Koestner, J.C. Frost, and G.A. Somorjai, *Surf. Sci.* **129** (1983) 482.

[24] F.A. Cotton and G. Wilkinson, *Advanced Inorganic Chemistry*, (J. Wiley and Sons, New York, 1980).

[25] L.L. Hegedus, J.C. Summers, J.C. Schlatter, and K. Baron, *J. Cat.* **56** (1979) 321.

[26] W.F. Egelhoff, *The Chemical Physics of Solid Surfaces and Heterogenous Catalysis, Vol. 4, eds D.A. King and D.P. Woodruff*, (Elsevier, Amsterdam, 1982) page 397.

[27] D.G. Castner, B.A. Sexton, and G.A. Somorjai, *Surf. Sci.* **71** (1978) 519.

[28] T.W. Root, G.B. Fisher, and L.D.Schmidt, *J. Chem. Phys.* **85(8)** (1986) 4679.

[29] G.S. Blackman, C.T. Kao, B.E. Bent, C.M. Mate, M.A. Van Hove, and G.A. Somorjai, Surf. Sci. in press.

[30] J.L. Gland, *Surf. Sci.* **93** (1980) 487.

[31] B.E. Hayden and A.M. Bradshaw, *Surf. Sci.* **125** (1983) 787.

[32] G. Pirug, H.P. Bonzel, H. Hopster, and H. Ibach, *J. Chem. Phys.* **71(2)** (1979) 593.

[33] I. Harrison, C.T. Kao, and G.A. Somorjai, In Preparation.

[34] G.E. Thomas and W.H. Weinberg, *Phys. Rev. Lett.* **41(17)** (1978) 1181.

[35] T.W. Root, L.D. Schmidt, and G.B. Fisher, *Surf. Sci.* **134** (1983) 30.

[36] L.A. DeLouise and N.Winograd, *Surf. Sci.* **159** (1985) 199.

[37] J.L. Gland and B.A. Sexton, *Surf. Sci.* **94** (1980) 355.

[38] H. Conrad, G. Ertl, J. Küppers, and E.E. Latta, *Surf. Sci.* **65** (1977) 235.

[39] P.A. Thiel and W.H. Weinberg, *J. Chem. Phys.* **73(8)** (1980) 4081.

[40] S. Tatarenko, M. Alnot, and R. Ducros, *Surf. Sci.* **163** (1985) 249.

[41] R.F. Lin, R.J. Koestner, M.A. Van Hove, and G.A. Somorjai, *Surf. Sci.* **134** (1983) 161.

[42] Air Products and Chemicals Inc., Model CSA-202, Allentown, PA 18103.

[43] R.B. King and M.B. Bisnette, *J. Amer. Chem Soc.* **85** (1963) 2527.

[44] R.C. Elder, F.A. Cotton, and R.A. Schunn, *J. Amer. Chem Soc.* **89** (1967) 3645.

[45] R. Eisenberg and C.D. Meyer, *Accnts. Chem. Res.* **8** (1975) 26.

[46] J. Müller and S. Schmitt, *J. Organomet. Chem.* **97** (1975) C54.

[47] P.A. Dimas, R.J. Lawson, and J.R. Shapley, *Inorg. Chem.* **20** (1981) 281.

[48] A. Kubat–Martin, A.D. Rae, and L.F. Dahl, *Organometallics* **4** (1985) 2221.

[49] C.T. Kao, G.S. Blackman, C. M. Chan, M.A. Van Hove, and G.A. Somorjai, In Preparation.

[50] M.A. Van Hove and S.Y. Tong, *Surface Crystallography by LEED*, (Springer, Heidelberg, 1979).

[51] M.A. Van Hove, W.H. Weinberg, and C.-M. Chan, *Low-Energy Electron Diffraction: Experiment, Theory and Surface Structure Determination*, (Springer Heidelberg, 1986).

[52] M.A. Van Hove, R.F. Lin, and G.A. Somorjai, *Phys. Rev. Lett.* **51** (1983) 778.

[53] T.W. Root, G.B. Fisher, and L.D.Schmidt, *J. Chem. Phys.* **85(8)** (1986) 4687.

[54] H. Ohtani, C.T. Kao, M.A. Van Hove, and G.A. Somorjai, *Progress in Surf. Sci.* **23** (1986) 155.

[55] J.M. MacLaren, J.B. Pendry, P.J. Rous, D.K. Saldin, G.A. Somorjai, M.A. Van Hove, and D.D. Vvedensky, *Surface Crystallographic Information Service: A Handbook of Surface Structures*, (D. Reidel Publishing Company (Dordrecht, Holland), 1987).

[56] C.M. Mate and G.A. Somorjai, *Surf. Sci.* **160** (1985) 542.

[57] C.M. Mate, B.E. Bent, and G.A. Somorjai, *J. of Elect. Spect. and Rel. Phen.* **39** (1986) 205.

[58] D.F. Ogletree, M.A. Van Hove, and G.A. Somorjai, *Surf. Sci.* **183** (1987) 1.

[59] R.F. Lin, G.S. Blackman, M.A. Van Hove, , and G.A. Somorjai, *Acta Cryst.* **B43** (1987) 368.

[60] H. Ohtani, M.A. Van Hove, and G.A. Somorjai, *J. Phys. Chem* **92** (1988) 3974.

[61] P.A. Thiel, E.D. Williams, J.T. Yates, and W.H. Weinberg, *Surf. Sci.* **84** (1979) 54.

[62] R.J. Koestner, M.A. Van Hove, and G.A. Somorjai, *Surf. Sci.* **107** (1981) 439.

[63] R.J. Koestner, M.A. Van Hove, and G.A. Somorjai, *J. Phys. Chem.* **87** (1983) 203.

[64] B.E. Bent, PhD thesis, University of California, Berkeley, CA 94720, 1986.

[65] R.J. Koestner, M.A. Van Hove, and G.A. Somorjai, *Surf. Sci.* **121** (1982) 321.

[66] L.H. Dubois, D.G. Castner, and G.A. Somorjai, *J. Chem. Phys.* **72(9)** (1980) 5234.

[67] J.E. Crowell and G.A. Somorjai, *Appl. Surf. Sci.* **19** (1984) 73.

[68] B.E. Koel, J.E. Crowell, B.E. Bent, C.M. Mate, and G.A. Somorjai, *J. Phys. Chem.* **90** (1987) 2949.

[69] M.A. Van Hove, R.F. Lin, and G.A. Somorjai, *J. Amer. Chem. Soc.* **108** (1986) 2532.

[70] D.A. Titterington and J.B. Pendry, Private Communication.

[71] B.W. Holland and D.P. Woodruff, *Surf. Sci.* **36** (1973) 488.

[72] B.E. Koel, B.E. Bent, and G.A. Somorjai, *Surf. Sci.* **147** (1984) 211.

[73] H.F. Efner, D.E. Tevault, W.B. Fox, and R.R. Smardzewski, *J. Organomet. Chem.* **146** (1978) 45.

[74] H. Ibach and D.L. Mills, *Electron Energy Loss Spectroscopy and Surface Vibrations*, (Academic Press (New York), 1982).

[75] R. Eischens and W.A. Pliskin, *Advan. Catalysis* **10** (1958) 1.

[76] C.M. Mate, C.T. Kao, and G.A. Somorjai, To be published.

[77] K. Heinz, D.K. Saldin, and J.B. Pendry, *Phys. Rev. Lett.* **55** (1985) 2312.

[78] M.G. Lagally, T.-M. Lu, and G.-C. Wang, *Ordering in Two Dimensions, ed S. Sinha*, (Elsevier, Amsterdam, 1980).

[79] M. Henzler, *Surf. Sci.* **168** (1986) 744.

[80] E.G. McRae and R.A. Malic, *Phys. Rev. Lett.* **58** (1987) 1437.

[81] R.J. Behm, K. Christmann, and G. Ertl, *Surf. Sci.* **99** (1980) 320.

[82] L.D. Roelofs, A.R. Kortan, T.L. Einstein, and Robert L. Park, *Phys. Rev. Lett.* **46** (1981) 1465.

[83] P.J. Rous and J.B. Pendry, *Surf. Sci.* **173** (1986) 1.

[84] P.J. Rous and J.B. Pendry, *Surf. Sci.* **155** (1985) 241.

[85] J.B. Pendry and D.K. Saldin, *Surf. Sci.* **145** (1984) 33.

[86] J.B. Pendry. *The Structure of Surfaces, Eds. M.A. Van Hove and S.Y.Tong*, (Springer Verlag, Heidelberg, Germany, 1985), page 124.

[87] D.K. Saldin, J.B. Pendry, M.A. Van Hove, and G.A. Somorjai, *Phys. Rev.* **B31** (1985) 1216.

[88] K. Heinz, K. Müller, W. Popp, and H. Lindner, *Surf. Sci.* **173** (1986) 366.

[89] P.J. Rous, J.B. Pendry, D.K. Saldin, K. Heinz, K. Müller, and N. Bickel, *Phys. Rev. Lett.* **57** (1986) 2951.

[90] G.S. Blackman, D.F. Ogletree, and G.A. Somorjai, In Preparation.

[91] M. Galanti, R. Gott, and J.F. Renaud, *Rev. Sci. Inst.* **42** (1971) 1818.

[92] H. Ibach and S. Lehwald, *Surf. Sci.* **176** (1986) 629.

[93] H. Steininger, S. Lehwald, and H. Ibach, *Surf. Sci.* **123** (1982) 264.

[94] M.A. Van Hove, *Proc. 8th Int'l Summer Inst. on Surf. Sci., Milwaukee, WI, Aug. 17–23*, (Springer Series in Surface Science, Springer Verlag, Heidelberg, Germany, 1987).

[95] P.L. De Andres, P.J. Rous, and J.B. Pendry, *Surf. Sci.* **193** (1988) 1.